Skin Cancer segmentation and Detection Using Total Variation and Multiresolution Analysis

Faouzi Adjed

NNT: 2017SACLE042

Skin Cancer segmentation and Detection Using Total Variation and Multiresolution Analysis

Thèse de doctorat de Universiti Teknologi PETRONAS et l'Université Paris-Saclay préparée à l'universiti Teknologi PETRONAS et l'université d'Evry Val d'Essonne

École doctorale n°580 Sciences et Technologies de l'Information et de la Communication (STIC)
Spécialité de doctorat: Traitement du signal et des Images

Thèse présentée et soutenue à Seri Iskandar, Perak, Malaisie, le 18 décembre 2017, par

Faouzi Adjed

Composition du Jury :

Rachid Jennane Professeur des universités, Université d'Orléans	Président, Rapporteur
Nur Ashidi Bin Mat Isa Full Professor, Universiti Sains Malaysia	Rapporteur
Vincent Vigneron Maître de conférences - HDR, Université d'Evry Val d'Essonne	Examinateur
Mahmod Bin Othman Associate Professor, Universiti Teknologi PETRONAS	Examinateur
Fakhreddine Ababsa Professeur des universités, Arts et Métiers ParisTech	Directeur de thèse
Ibrahima Faye Associate Professor, Universiti Teknologi PETRONAS	Co-Directeur de thèse

Thèse de doctorat

université PARIS-SACLAY
ÉCOLE DOCTORALE
Sciences et technologies de l'information et de la communication (STIC)

Titre : Segmentation et Détection du Cancer de la Peau en Utilisant la Variation Totale et l'Analyse Multi-résolution

Mots clés : Segmentation, Détection, Variation Totale, Analyse Multi-résolution, Imagerie médicale

Résumé : Les décès du cancer de la peau sont majoritairement des mélanomes malins. Il est considéré comme l'un des plus dangereux cancer. A ses débuts, les mélanomes malins sont traités avec des simples biopsies et sont complètement curable. Pour cela, une détection précoce est la meilleure solution pour réduire ses conséquences désastreuses. Imagerie médicale telle que la dermoscopie et les caméras à images standard sont les outils disponibles les plus adaptées pour diagnostiquer précocement les mélanomes. Le diagnostic assisté par ordinateur (CAD) est développé dans le but d'accompagner les radiologistes dans la détection et le diagnostic. Cependant, il y a un besoin d'améliorer la précision de la segmentation et de détection des lésions. Dans ce travail, le modèle de Chan et Vese a été adapté pour segmenter davantage les variations à l'intérieur des lésions avec un résultat très encourageant. La deuxième tâche consiste à extraire des caractéristiques afin de discriminer les mélanomes. Deux méthodes ont été développée, une se basant sur l'irrégularité des bords des lésions et l'autre par la fusion des caractéristiques texturales et structurelles. Les résultats ont montrés de bonnes performances avec une précision de 86.54% et de 86.07%, respectivement.

Title : Skin Cancer Segmentation and Detection Using Total Variation and Mutiresolution Analysis

Keywords : Segmentation, Detection, Total Variation, Multiresolutional Analysis, medical imaging

Abstract : The vast majority of skin cancer deaths are due to malignant melanoma. It is considered as one of the most dangerous cancers. In its early stages, malignant melanoma is completely curable with a simple biopsy. Therefore, an early detection is the best solution to improve skin cancer prognostic. Medical imaging such as dermoscopy and standard camera images are the most suitable tools available to diagnose melanoma at early stages. To help radiologists in the diagnosis of melanoma cases, there is a strong need to develop computer aided diagnosis (CAD) systems. The accurate segmentation and classification of pigment skin lesions still remains a challenging task due to the various colors and structures developed randomly inside the lesions. The current work focused on two main tasks. In the first task, a new approach of the segmentation of skin lesions based on Chan and Vese model is developed. The model is adapted to segment the variations of the pigment inside the lesion and not only the main border. The subjective evaluation, applied on a database of standard camera images, obtained a very encouraging results with 97.62% of true detection rate. In the second main task, two feature extraction methods were developed for the analysis of standard camera and dermoscopy images. The method developed for the standard camera skin cancer images is based on border irregularities, introducing two new concepts, which are valleys and crevasses as first and second level of the border irregularity. The method has been implemented on DermIs and DermQues, two databases of standard camera images, and achieved an accuracy of 86.54% with a sensitivity of 80% and a specificity of 95.45%. The second method consisted of a fusion of structural and textural features. The structural features were extracted from wavelet and curvelet coefficients, while the textural features were obtained from the local binary pattern operator. The method has been implemented on the PH2 database for dermoscopy images with 1000-random sampling cross validation. The obtained results achieved an accuracy, a sensitivity and a specificity of 86:07%, 78.93% and 93.25%. Compared to the existing methods, the proposed methods in this work show very good performances.

Université Paris-Saclay
Espace Technologique / Immeuble Discovery
Route de l'Orme aux Merisiers RD 128 / 91190 Saint-Aubin, France

DEDICATION

To my beloved Dad and Mum.

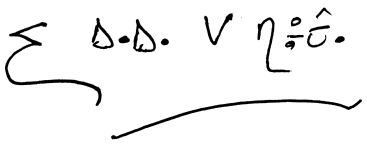

ACKNOWLEDGEMENTS

Firstly, I would like to thank the two universities that were part of this joint supervision, Université d'Evry Val d'Essonne, Paris Saclay and Universiti Teknologi PETRONAS, for the opportunity they gave me to be part of their Ph.D program. They both collaborated and contributed to the succeed of this Ph.D study.

I would like to express my sincere gratitude to my supervisors, Associate Professor Ibrahima FAYE and Professor Fakhreddine ABABSA for their continuous support, their patience and constant motivation, but also for the hard questions which encouraged and guided me to widen my research from various perspectives. Without their high quality supervision this work would not have been accomplished. I would like to thank also my co-supervisor in UTP, Associate Professor Sarat CHANDRA DASS.

Besides my supervisors, I would like to give my high, respectful gratitude to Professor Rachid JENANE, Professor Nur Ashidi BIN MAT ISA, Doctor Vincent VIGNERON and Doctor Mohamed BIN OTHMAN for accepting to be part of the committee members, and for their brilliant comments and suggestions.

I especially thank Virginie BRIANTAIS, medical expert, and Dalil ICHALAL, image processing expert, for evaluating my recent work, and providing good advice and perspectives.

A special gratitude to CISIR and IBISC Laboratory for their hospitality, a wonderful workspaces and facilities provided. My special gratitude to Sabine Segala, Marité QUINTIN, Professor Gilles DUC and Bahrul Ilmi. I am also grateful to all my collegues at the CISIR Laboratory, for their wonderful company and support, especially

to Dr. Munsif, Dr. Jamal, Dr. Abu Elhassan, Amjad, Altahir, Nirbhay and Dr. Vedpal for their support during this work. I also would like to thanks IBISC collegues for their wonderful company and support, especially to Aylen, Dr. Alia, Dr. Abdelkader, Mahmoud, Dr. Junior and Ludovic.

I would like to thank my friend Peter and his wife Keri for their help and support, my friends Emefa, Sheela, Djoudi, Mounir, Krimo and all my friends of ACKB association for their support and encouragement.

I would like to express my eternal appreciation towards my brother Hassan and my sister-in-law Nadège, my nieces Pauline and Lisa, my nephew Akli and his wife for their support and continuous help during this three years of instability between two countries.

I would like to thank all my brothers and sisters living in Kabylia (Algeria), Slimane, Hayet, Zahir, Ferdjallah, Nabil, Toufik, Karima and all my nephews and nieces.

Finally, and most important, I want to thank my parents, Hadi and Nouara, who have been there unconditionally and urged me to be better. This accomplishment would not have been possible without them.

TABLE OF CONTENTS

LIST OF TABLES

LIST OF FIGURES

LIST OF ABBREVIATIONS

$ABCD$	Asymmetry, Border, Color, Diameter
Acc	Accuracy metric
ANN	Artificial Neural Network
$ANOVA$	Analysis Of Variance
AUC	Area Under Curve
CAD	Computer Aided Diagnosis
CIE	International Commission on Illumination
CNN	Convolutional Neural Network
DCT	Discrete Cosine Transform
DFT	Discrete Fourier Transform
DWT	Discrete Wavelet Transform
EM	Expectation Minimization
Ep	Error probability
FCM	Fuzzy C-Mean
$FDCT$	Fast Digital Curvelet Transform
FFT	Fast Fourier Transform
FN	False Negative
FP	False Positive
FPR	False Positive Rate
$GPAC$	Graph Partitioning Active Contours
GVF	Gradient Vector Flow
$ISIC$	International Skin Imaging Collaboration
JRC	Joint Reverse Classification
kNN	k-Nearest Neighbor
LBP	Local Binary Pattern
MLR	Multi-scale Lesion-biased Representation
NPR	Negative Predictive value

PDE	Partial Differential Equation
PH^2	PH^2 Database
PPR	Positive Predictive value
RGB	Red Green Blue channel
ROC	Receiver Operating Characteristic
ROI	Region Of Interest
SCF	Skin Cancer Foundation
$SIFT$	Scale Invariant Feature Transform
Sen	Sensitivity metric
Spe	Specificity metric
$SPAM$	Sequential Pattern Mining
SPT	Steerable Pyramids Transformation
SSA	Stacked Sparse Auto-Encoder
Std	Standard deviation
SVM	Support Vector Machine
$TDLS$	Texture Distinctiveness Lesion Segmentation
TD	Texture Distinctiveness
TDR	True Detection Rate
TN	True Negative
TP	True Positive
TV	Total Variation
VP	Validation Performance
Vs	Versus
WHO	World Health Organization

NOMENCLATURE

$\mathbb{C}$	Set of complex numbers
div	Divergence
α	alpha
∂	differential partial
δ	delta
Δ	Delta
ε	epsilon
Γ	Gamma
χ	khi
$\subset$	inclusion
$\inf$	infinite
λ	lambda
μ	mu
$\mathbb{N}$	Set of positive integer numbers
∇	nabla
ν	nu
ω	omega
Ω	Omega
π	pi
Π	Product (PI)
ϕ	phi
Φ	Phi
φ	varphi
ψ	psi
$\mathbb{R}$	Set of real numbers
$\mathbb{R}^2$	Set of two dimensional real numbers
θ	theta

$\cup$	union
ξ	xi
$\mathbb{Z}$	Set of integer numbers

CHAPTER 1

INTRODUCTION

1.1 Overview

Melanoma is the most dangerous abnormal skin tissue. Its treatment requires chemotherapy and radiotherapy and it becomes more difficult to treat when it is in advanced stages such as metastasis step [6], where one person die each 54 minutes [2]. The statistics show that approximately $132,000$ melanoma cases and 2 to 3 millions of non-melanoma cases [6,7] are reported annually in the world. In total, it accumulates to 1.6% of cancer cases worldwide [8]. Despite the rarity of this diseases, the vast majority of persons affected by malignant skin cancer deaths within two years [2]. As ozone levels are depleted, the World Health Organization (WHO) [6] estimates that 10% of decrease in ozone level will result in an additional of $300,000$ non melanoma and 4500 melanoma cases. According to WHO and Lee et al. [9], Caucasian populations generally have a much higher risk of getting skin cancer disease than dark-skinned populations. Naturally, brown and black people can usually safely tolerate relatively high levels of sun exposure without getting sunburns or greatly increasing their skin cancer risk. In contrast, people with pale or freckled skin, fair or red hair and blue eyes belong to the highest risk group. Followed by people with dark hair and eyes who do not normally get sunburns are at medium risk of skin cancer developing [6]. According to the World Health Organization, the following items present a set of risk factors of skin cancer: fair skin; blue, green or hazel eyes; light-coloured hair; tendency to burn rather than suntan; history of severe sunburns; many moles and/or freckles; a family history of skin cancer. In the United States and worldwide, skin cancer incidence is reported as one of the most

increasing tumor. The risk of developing invasive melanoma was estimated to 1 in 39 of Caucasian men and 1 in 58 for Caucasian women in American society in 2010 [10].

1.1.1 Causes of Skin Cancer

Cancer starts when cells in the body begin to grow out of control. Cells in nearly any part of the body can become cancer, and can then spread to other areas of the body [11]. Similarly, skin cancer is the uncontrolled growth of abnormal skin cells. It occurs when unrepaired DNA damage to skin cells, most often caused by ultraviolet radiation from sunshine or tanning beds, triggers mutations, or genetic defects, that lead the skin cells to multiply rapidly and form malignant tumors [2].

1.1.2 Types of Skin Cancer

The multitude of benign and malignant melanoma complicates the recognition of skin lesion cases. In the clinical practice, three main types of abnormal skin cells are noticed i.e. *Basic cell carcinoma*, *Squamous cell carcinoma* and *Melanoma* [11, 12]. The Skin Cancer Foundation (SCF) [2], further into these, characterizes three more kinds of abnormal cells, i.e., *Actinic keratosis*, *Merkel cell carcinoma* and *Atypical moles*, which are less common. Figure 1.1 illustrates the six types of skin lesions. It notices also that the atypical moles are the second most dangerous cells after melanoma cases.

Figure 1.1: Different kinds of skin cancer classified by the Skin Cancer Foundation [2]

According to Skin Cancer Foundation [2], the difference between these abnormality tissues are:

- Actinic Keratosis, also known as a solar keratosis, is a crusty and scaly growth. It is considered as pre-cancer because if left alone, it could develop into a skin cancer.

- Merkel cell carcinoma is a rare and aggressive skin cancer that is at high risk of recurring and spreading (metastasizing) throughout the body. But, it is 40 times rarer than melanoma.

- Basic cell carcinoma is the most occurring form of skin cancer. It often looks like open sores, red patches, pink growths, shiny bumps or scares. This skin cancer very rarely spreads.

- Squamous cell carcinoma is the second most common form of skin cancer. It often looks like scaly red patches, open sores, elevated growths with a central depression, or warts.

- Atypical moles are unusual-looking benign moles, also known as dysplastic nevi. They may resemble melanoma, and people who have them are at increased risk of developing melanoma in a mole or elsewhere on the body. They have 10 times or more the risk of developing melanoma.

- Melanoma is the most dangerous form of skin cancer, these cancerous growths develop when unrepaired DNA damage to skin cells, mostly caused by ultraviolet radiation from sunshine or tanning beds, triggers mutations (genetic defects) that lead the skin cells to multiply rapidly and form malignant tumors. The majority of melanomas are black or brown, but they can also be skin-colored, pink, red, purple, blue or white. If melanoma is recognized and treated early, it is almost always curable, but if it is not, the cancer can advance and spread to other parts of the body, where it becomes hard to treat and can be fatal.

It is noticed that the first cause of these skin cancer types are the damage of skin tissue

from exposure to ultraviolet radiations [2, 6, 7, 11].

1.2 Medical Diagnosis

To recognize melanoma cases, dermatologists compare and analyze a multiple signs of each tumor. Mostly, they use two scoring systems based on visual characteristics to recognize the melanoma tissue, which are ABCDE rule [2, 12–15] and Glascow 7-point checklist / 7-point checklist [12, 16–18].

These two scoring systems are well known by medical experts and they constitute the basic methods of comparison for image processing experts. Most of the developed and explored methods are based on these systems, such as Bareiro et al. [19] and She et al. [20] for ABCD rule, and Argenziano et al. [21] for 7-point checklist. The features used in these systems are also explored separately in the goal of melanoma recognition, for example, pigment network [8, 22] and vascular structure [23]. These systems are summarized in the current chapter and detailed in the literature review chapter.

1.2.1 ABCD Rule

The skin cancer foundation explained the ABCD rule, called also ABCDE rule when the evolving feature is available. The meaning used for each case is explained and illustrated below:

- Asymmetry (A): The pigment is considered asymmetric if by drawing one vertical or horizontal line, the two parts of the mole will not be similar.

Figure 1.2: Asymmetry of melanoma compared with benign lesion [2].

- Border (B): More the pigment border is not smooth, more it can be considered as malignant case.

Figure 1.3: Border irregularity between malignant and benign lesions [2].

- Color (C): Most benign pigments have one color (often brown color). Melanoma has a variety of colors (black, red, blue and/or wight).

Figure 1.4: Color variation between melanoma and benign lesion [2].

- Diameter (D): Benign pigments have usually smaller diameter than malignant ones. Melanoma is often greater than 6 mm, but it can be smaller.

Figure 1.5: Diameter in melanoma and benign lesion [2].

- Evolving (E): Over time, benign pigment looks the same. However, malignant melanoma evolves or changes in size, shape, color and/or elevation.

Figure 1.6: Evolving of melanoma over time [2].

Table 1.1: ABCD rule with the interval values of p_i and the weight factor w_i of each component [1].

Feature	Description	Points p_i	Weight factor w_i	sub-score range
Asymmetry	One value of 0.5 for each axis.	$0-2$	1.3	$0-2.6$
Border	Eight segment, one value of 1 for each abrupt pigment cutoff.	$0-8$	0.1	$0-0.8$
Color	One value of 1 for each color: white, red, light brown, dark brown, blue-gray.	$1-6$	0.5	$0.5-3$
Dermoscopic structures	One value for each structure: pigment network, structureless area, dots, globules, branched streaks.	$1-5$	0.5	$0.5-2.5$

Figures from 1.2 to 1.6 illustrate the five rules of ABCD/ABCDE rules showing the difference between malignant and benign lesion. The real computation of ABCD system is done only for the first four components using the following formula:

$$S_{abcd} = \sum_{i=1}^{4} w_i p_i \tag{1.1}$$

where w_i and p_i are the weight and the value attributed to each point. They are summarized in table 1.1 as explained by Capdehourat et al. [1], according to Stolz et al. [14]. Knowing that the evolution of the lesion over time is the most missed data, then the feature given by the item E is used only for visual comparison by dermatologists when it is available.

The evaluation of ABCD rule is performed following equation (1.1) using the scores given in the table 1.1 to classify the pigment into three cases, benign, clinically doubtful and malignant [1]:

$$\begin{cases} S_{abcd} < 4.75 & \text{then the pigment is benign} \\ 4.75 \leq S_{abcd} \leq 5.45 & \text{then the pigment is clinically doubful} \\ S_{abcd} > 5.45 & \text{the pigment is malignant} \end{cases}$$

Table 1.1 expresses the description of each feature of the system and gives their different point values and weight factors.

1.2.2 7-point Checklist

The 7-point checklist [17] and Glascow 7-point checklist system [18], summarized by Capdehourat et al. [1] (see Figure 1.7) and Korotkov et al. [12], is another scoring system based on seven criteria divided into two sets. For Glascow 7-point checklist, the major criteria are changes in shape, size and color, and the minor criteria are diameter, inflammation, crusting and sensory changes. The 7-point checklist criteria works in the same way, with some differences and more details, as presented below:

- Atypical pigment network: Black, brown, or gray thickened and irregular lines segments in the lesion.
- Blue-whitish veil: Irregular, confluent, gray-blue to whitish-blue diffuse pigmentation that can be associated with pigment network alteration, dots/globules, or streaks.
- Atypical vascular pattern: Linear-irregular and/or dotted red vessels not seen in regression area.
- Irregular streaks: Pseudo pods or radial streaming irregularities arranged at the periphery of lesion.
- Irregular pigmentation: Black, brown or gray featureless areas with irregular shape and/or distribution.
- Irregular dots/Globules: Black brown, or gray rounded to oval, and variously sized irregularity structures distributed in the lesion.
- Regression structures: White scar-like areas and/or blue pepper-like areas (gray-blue areas and/or multiple blue-gray dots).

Table 1.2: The major and minor criteria of 7-point checklist and the different weights for each criterion [1].

Major criteria	Score	Minor criteria	Score
Atypical pigment network	2	Irregular streaks	1
Blue-whitish veil	2	Irregular pigmentation	1
Atypical vascular pattern	2	Irregular dots/globules	1
		Regression structures	1

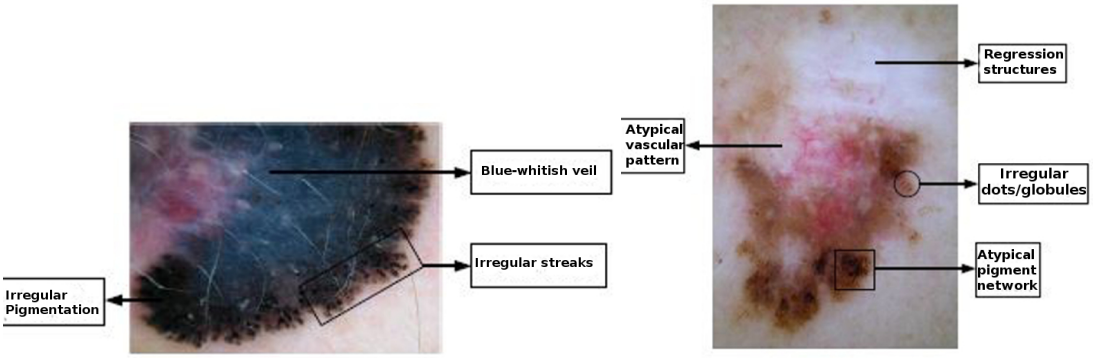

Figure 1.7: 7-point checklist illustration [1].

For 7-point checklist, the scores given to each point, the same for Glascow 7-point checklist, are 2 for major criteria and 1 for minor ones as summarized in table 1.2. The evaluation of the score follows the following formula:

$$s_{7pc} = \sum_{i=1}^{3} M_i + \sum_{j=1}^{4} m_j \tag{1.2}$$

where M_i and m_j define the i^{th} major and j^{th} minor criteria respectively.

The classification following this system is also based on thresholding functions into two different classes [1]:

$$\begin{cases} S_{7pc} < 3 & \text{the pigment is benign} \\ S_{7pc} \geq 3 & \text{the pigment is malignant} \end{cases}$$

Table 1.2 details the major and minor criteria of 7-point checklist system.

1.3 Computer Aided Diagnosis Systems

Computer Aided Diagnosis (CAD) systems have been developed in several contributions of medical imaging [24–26]. The objective of CAD systems is to provide a computer output as a second opinion in order to assist radiologists on interpretation to improve the accuracy of diagnosis and reduce the image reading time [27]. A CAD system is generally identifying two types of systems depending upon its main function i.e. Computer Aided Detection (CADe) system and Computer Aided Diagnosis (CADx) system. It is also explored for the early both detection and diagnosis [28]. A CAD system is applied on different tumor images such as mammograms, dermoscopy, MRI, radiography, etc. A CAD system was already known in the 1960s and became more interesting topic in the 1980s, where many investigations and researches were explored in some laboratories and hospitals [12]. Since 2000s, the number of papers in CAD system are mostly increased in the achievement of the detection and the diagnosis of melanoma [24, 27].

The CAD system applied in medical imaging contains five main steps from the image acquisition to the classification and diagnosis:

1. **Image acquisition:** In image processing, this step is considered as source or data for the next steps. In addition to that, there are many important and consistent informations from the acquisition to help the image processing experts to have a baseline and an intuitive work direction to explore.

2. **Image enhancement:** The objective of this step is to reduce noises and all artifacts in the images. These artifacts in most cases depend on the kind of image acquisition technique employed, and represent, for example, numbering in mammogram images, hair and blood vessels in dermocopic images.

3. **Segmentation:** The segmentation of the Region Of Interest (ROI) is an important step in CAD system. The multitude of skin cancer images makes the segmentation task more difficult. It becomes one of the hardest and most challenging task in CAD system.

4. **Feature extraction:** Once the ROI is isolated, the objective of this step is to provide the best descriptor to extract features which discriminate the database into two or more classes.

5. **Classification and detection:** The final step is classification and diagnosis where the proposed system is observed and analyzed. Depending on the feature extracted and the number of classes desired, the choice of the classifier is primordial to get better results on the detection. According to the classifier used, the classification rate is evaluated following some performance metrics, such as accuracy, sensitivity, specificity and receiver operating characteristic (ROC).

CAD system is developed in melanoma recognition as well. Following the five steps of the system, there are many methods adopted or developed specifically for melanoma detection. The next chapter summarizes the literature review on skin cancer detection according to these steps, it makes also in evidence the logic of these steps on CAD system and the different contributions in each step.

1.4 Problem Statement

Melanoma treatment needs chemotherapy and radiotherapy, as breast cancer, blood cancer, brain tumor, lung cancer, and other cancer types when they reach metastasis state [2, 29]. To avoid these painful procedures and receive successful treatment, early detection is one of the most reliable solutions.

The CAD systems explored for improving the accurate decision is still in development. Nowadays, as reported by Korotkov et al. [28], many CAD systems are available for pigment skin lesions detection such as Dell'Eva-Burroni Melanoma Image processing Software which is the most cited in the literature and gives lower performances in real applications. However, it is difficult to draw overall conclusions regarding the performance of these systems. The different image acquisition (dermoscopic, clinical and standard camera images) in structured studies complicates furthermore the classification task in one global methodology. Thus, the current CAD systems are still far from

perfection and need more developments to improve the detection and the diagnosis of melanoma. Despite, the improvements of CAD systems over years, there are still some challenges involved, such as accurate and adaptive segmentation. Moreover, to classify the skin pigment lesions into malignant and benign cancer, two major problems are evoked.

- Firstly, the accurate segmentation is the first challenging task to improve in the first plan the detection of suspicious lesions, and in the second plan the classification of these lesions into malignant and benign.

- Secondly, the extraction of the most discriminative set of features describing the relevant characteristics separating the pigment lesions into benign and malignant skin cancer.

In addition to that, the key to improve the real output quality of CAD systems is to apply the proposed methods on free public datasets for the comparison of all developed algorithms. To reduce also the human error of diagnosis, each pigment skin lesion should be accompanied by the ground truth and diagnosis reported from several dermatologists [12].

1.5 Research Objectives

The main objective of this thesis is to improve melanoma detection and recognition. To accomplish this objective, the PhD work was oriented into the following specific directions:

- To investigate a method of segmentation adapted for skin lesions characteristics, that could segment even the small regions inside the skin pigment lesion.

- To develop a method of features extraction based on fusion of structural and textural features.

- To develop a method based on border irregularities of pigment lesions.

1.6 Research Hypothesis

To achieve our research objectives, the following research hypothesis are made:

- A total variation method exploring an extension of Chan and Vese model would be efficient for segmentation of regions of interest in skin lesion images.
- A fusion of structural and textural features exploring the Local Binary Pattern operator and multiresolution analysis methods (curvelet and wavelet transform) on dermoscopic image database would be efficient to discriminate further between malignant and benign lesion.
- An investigation of geometrical characteristics based on the border irregularities may provide a description of pigment skin lesions.

1.7 Scope of Research Work

The scope of the work is to aid and improve the Computer Aided Diagnosis based on image processing methods. The work is concentrated on two main directions, segmentation and features extraction. The first direction is based on Chan and Vese model. The model was extended and adapted for skin cancer segmentation. In addition to the whole region of interest, the algorithm segments the inter-regions of the lesions. The second part of the work consists of extracting the most discriminant features, either for dermoscopic and standard camera images. For dermoscopic images, multiresolution analysis using wavelet and curvelet were combined with local binary pattern and used for feature extraction to discriminate skin lesions. For standard camera images, border smoothness and irregularities are explored and developed, introducing valleys and crevasses concepts as features to make border between malignant melanoma and benign skin lesion (non-melanoma) images. All results of developed methods and comparisons are highlighted and discussed.

1.8 Thesis Organization

The work of this thesis is organized into the following six chapters:

Chapter 1 describes the skin cancer, computer-aided diagnosis tasks, objectives and contributions of the current work.

Chapter 2 presents a literature review of CAD systems and different methods developed for skin cancer enhancement, segmentation, feature extraction and finally the detection and recognition step.

Chapter 3 contains mathematical tools used in the current work. It is divided into three sections which are Total Variation, Multiresolution Analysis (Fourier transform, wavelet, ridgelet and curvelet) and finally the classifiers used (support vector machine and artificial neural network).

Chapter 4 introduces the methodology of the proposed system. It provides all the details of the techniques developed during this PhD work.

Chapter 5 reports the obtained results from the proposed methodology and its comparison to existing methods and algorithms. It also illustrates different intermediate steps of the work.

Chapter 6 concludes the overall work of the thesis and gives recommendations for the future work. It enumerates the scientific papers published in workshops, conferences and journals.

CHAPTER 2

LITERATURE REVIEW

2.1 Overview

Skin cancer recognition on CAD systems has been an active research area for more than 30 years back [28]. For instance, many methods have been developed and explored for melanoma detection [30]. Korotkov and Garcia [12] presented an interesting overview of used and explored methods on clinical and dermoscopic images from 1984 to 2012. Their review is organized following ABCDE [31] criteria and other methods developed in clinical and computer-aided diagnosis system (CAD) from the data acquisition step to the classification and diagnosis. Maglogiannis and Doukas [16] have also presented in 2009 an overview on CAD system methods. A non exhaustive comparison of the most important implementations is reported, specifically features selection such as color and border, and wavelet coefficients. They also presented the classifiers often used in the literature, such as Artificial Neural Network and Support Vector Machine. Masood and Al-Jumaily [32] in 2013 presented a review of techniques and algorithms used in skin cancer, and also a comparison of performances of these methods on skin lesion recognition. Recently, in 2015, Celebi et al. [33] presented a state of the art survey on the 50 published border detection methods. The authors evaluated the subjective and objective evaluations and their impact on the quality of segmentation results of skin border lesions. The conclusions of these review papers are detailed below in the different steps of CAD system.

As mentioned in the Introduction chapter (Chapter 1), the two scoring systems, ABCD rule and 7-point checklist, well known by the clinicians and dermatologist in

clinical diagnosis and by non dermatologists in screening procedures are detailed in this chapter. In this topic, the scoring system related to ABCD rule was proposed by Friedman [13] in 1985 and developed by Stolz et al. [14] in 1994. This system is widely used in clinical practice [12]. Following each feature, the system is divided into points values and weight factors as detailed in Table 1.1 in the last chapter.

According to Capdehourat et al. [1], the scoring system for ABCD rule follows equation (1.1) (page: 6). Where p_i represents the number of points attributed to each feature and w_i is the weight factor as explained in table 1.1.

The classification of the ABCD system scoring is based on two thresholds following the value of S_{abcd} given in equation (1.1). Therefore, if $S_{abcd} < 4.75$ the lesion is classified as benign, if $4.75 \leq S_{abcd} \leq 5.45$ the lesion is considered as clinically doubtful and if $S_{abcd} > 5.45$ then the lesion is classified as malignant. It can be seen from the table 1.1 that border irregularity feature has less impact, with variation from 0 to 0.8, comparing to other features with variation from 0 to more than 2.5.

The 7-point checklist was proposed by Argenziano et al. [17], which is another variation of pattern analysis with fewer criteria for identification and analysis [1]. The idea of 7-point checklist system is to attribute the score of 2 for major and 1 for minor criteria as summarized in the table 1.2.

The classification is performed following a fixed threshold equal to 3 separating the pigment lesions on two classes. Thus, the pigment is classified as benign if the total value is lower than 3 (Total ≤ 3), on the other side it is classified as malignant if the total is greater than 3 (Total > 3) as explained in the previous chapter. Argenziano et al. [21] in 2011 and Walter et al. [34] in 2013 presented a new version of 7-point checklist to improve the accuracy of diagnosis.

Dolianitis et al. [35] compared 4 dermoscopic algorithms, ABCD rule, pattern analysis, Menzies method and 7-point checklist. The study showed that the best results are obtained by Menzies method with an accuracy of 81.1%, followed by ABCD rule with an accuracy of 79%, 7-point checklist is in the third place with an accuracy of 77.2%

and in the last position, the pattern analysis algorithm. They reached the same conclusion that Carli et al. [36], where 7-point checklist is more sensitive than ABCD rule and pattern analysis. However, in their study (Dolianitis et al.), the Menzies method showed the highest sensitivity of 84.6%, followed by 7-point checklist with 81.4% and ABCD rule with 77.5%, and finally, pattern analysis had the lowest sensitivity of 68.4%. On the other hand, the highest value of specificity of 85.3% is reported by pattern analysis followed by ABCD rule with 80.4% and Menzies method with 77.7% and in the last position 7-point checklist with a specificity of 77.2%. This study was conducted by the ground truth of sixty-one medical experts, but only on 40 melanocytic skin lesions.

In the literature, most CAD system papers contribute in one or more than one area of image processing, which include image preprocessing, segmentation, feature extraction and finally the classification and diagnosis. The techniques developed in image preprocessing are presented in section 2.2 where the main objective is to enhance the image quality and remove noise. Then, it is followed by the segmentation techniques treated in section 2.3 for the detection of the Regions of Interest. Methods explored for feature extraction to discriminate the lesions are presented in section 2.4. Finally the classification and diagnosis treated in section 2.5 describes the most cited classifiers and methodologies used for melanoma recognition. The different obtained results are described continuously following the main area of contribution.

2.2 Preprocessing: Image Enhancement

The main objective of image enhancement is to improve the quality and readability of the images. In the literature, it is also known as the preprocessing image step. In skin cancer images, the goal of this step is specially to remove the artifacts, such as hair and human made artifacts. Image enhancement is also used to improve the contrast quality for the exploration and visibility of details. Therefore, to compensate the imperfection of image acquisition and eliminate different artifacts, many methods and algorithms are developed and explored on various skin lesion databases. The dermoscopic images artifacts can be obtained and observed as uneven illumination, dermoscopic gel, black

frames, ink markings, rulers and air bubbles. In fact, the border detection can also be affected by intrinsic cutaneous features such as blood vessels, hairs, and skin lines [16]. In the literature, according to Koroktov [28], artifacts are divided into two sets, artifacts rejection and image enhancement. Artifacts rejection contains hair, air bubbles, specular reflections and ink marking. In the other part, image enhancement contains color correction and calibration, illumination correction, contrast enhancement and edge enhancement. In 2009, Celebi et al. [37] focused on the importance of the current step in border detection, mentioning the most important used methods such as Gaussian and Median filters.

In dermoscopic images, the most common artifact, and necessary to remove, is the hair. Many methods and algorithms are presented in the literature to remove the hair when it is not shaved before the acquisition step. Therefore, the typical algorithm of hair removal methods is based on two main steps:

1. The hair detection: it consists on detecting and removing the different hairs in the image using algorithms of detection. Most developed methods in this step use segmentation because the hair is an integral component compared to other noise types.

2. The image restoration: the restoration or inpainting step consists on filling the space occupied by the removed hair with proper intensity and color values. The image quality can be affected when the density of hair is big in the lesion border. Also, the texture of the pigment can be affected in some cases. Therefore, the shaving of the concerned area, when it is possible, is a good solution and compromise to reduce diagnosis errors.

Many methods are explored in the hair removal task. In the literature, DullRazor software [38], proposed in 1997, is the first widely adopted method for removal-of hair [12]. DullRazor performs the identification of the dark hair location using morphological closing operation, the verification of hair pixel shape and the replacement using bilinear interpolation, and the smoothness of replaced pixels with median filter. In 2008, Wighton et al. [39] proposed an alternative method for the inpainting step of

DullRazor software. In addition to the interpolation used in DullRazor software, the authors explored other information, like the direction of the border using Laplacian to regulate and measure the smoothness.

In 2011, Kiani et al. [40] proposed an improvement of DullRazor method using different approaches. The authors used Prewitt filter for edge detection and Radon transform for predominant direction of the hair, they also used different masks to isolate the hair from other noises. Following the same idea, Toossi et al. [41] proposed a morphological operator using adaptive canny edge detector for hair detection and multi-resolution coherence transform inpainting technique to repair and replace smoothly the emplacements of removed hair. On a database of 50 images, the method achieves 88.3% of diagnostic accuracy and 9.9% of error segmentation. Nguyen et al. [42] used universal matched filtering kernel and local entropy thresholding to get raw binary hair mask. Therefore, a combination of morphological thinning with Gaussian curve fitting is used for refining and verification of hair masks. Xie et al. [43] focused their research on repairing removed hair using PDE-based image inpainting. The method proposed by the authors contains three main parts, morphological closing is used for enhancement in the first step, followed by hair segmentation using statistical thresholding and extracted by the elongate of connected regions, and at the end they used PDE-based image inpainting for restoration. The authors applied their proposed method on 80 images (40 images without hair and 40 with hair). The obtained result showed 5% of errors for the case without hair and 18% for the images containing hair. Following the same idea Fierose et al. [44] proposed PDE-based image inpainting for restoration combined with top-hat operator (morphological enhancement) for segmentation and Otzu threshold for hair detection. Applying the current method on 20 images, the results showed an error of 15.6%. Huang et al. [45] explored multi-scale curvilinear matched filtering for hair detection and linear discriminant analysis for image restoration. Abbas et al. [46] proposed a matched filtering with first derivative-of-Gaussian method for hair detection. This approach showed accurate results, but the multitude of parameters complicates its implementation. Applied on 100 dermoscopic images, the method showed a diagnostic accuracy of 93.3%. The authors applied the same method in the next published paper [47,48] when hair removal was needed. Barata et al. [49] used a bank of directional

filters and PDE-based interpolation for hair detection and inpainting, respectively.

Gómez et al. [50] proposed an unsupervised algorithm based on Independent Histogram Pursuit. This algorithm estimates a set of linear combinations of images bands to enhance the different structures of the image. The results obtained showed an increment of border quality detection. Following the similar objective of contrast enhancement, Celebi et al. [51], proposed for a given RGB image input, they maximize the histogram bi-modality measure to increase the contrast between the lesion and the background. Madooei et al. [52] explored artifacts removal and image enhancement on 120 images based on the effect of light-intensity on the edges. The experience was implemented on border detection after enhancement with a sensitivity of 92% and a specificity of 88%.

Recently, in 2015, Koehoorn et al [53] proposed a new approach based on thresholding set decomposition and morphological analysis using gap-detection by multi-scale skeletons. Mizaarlian et al. [54] proposed an alternative approach to detect hair in dermoscopic images using the measurement of turbulence quaternion [55] and dual matched filters for hair suppression. For the restoration, the authors used the interpolation used in DullRazor software developed in [38]. On a database of 40 dermoscopic image and 94 synthetic images, the results obtained for hair segmentation are 86% and 85% of accuracy for dermoscopic and synthetic images respectively. The results of enhancement gave 90% and 96% of sensitivity for dermoscopic and synthetic images respectively.

To remove other artifacts such as capillary and blood vessels, many methods are also developed and explored. Huang et al. [56] extracted capillaries from skin lesions, they used a compact set of 1 curvilinear and 2 color parameter features and trained using SVM classifier to detect the different capillaries. Applying the proposed method on a database of 49 images with 21 visible capillaries and 28 non visible capillaries. The authors obtained 98.8% of accuracy, 90.5% of sensitivity and 89.3% of specificity. Earlier, Argenziano et al. [23] described the different vascular structures and its association with various melanocytic and nonmelanocytic tumors using statistical tests, such as χ^2 and Fisher tests. On a database of 531, the dots vessels showed a positive prediction on melanocytic lesions of 90%.

Abbas et al. [47] also treated specular reflexion reduction using Fourier transform and median filter for air bubbles or dermoscopic-gel reduction. Barata et al. [49] used in their work a sub-band thresholding for the intensity to reduce the reflexion to enhance the quality of images in pigment network detection.

Table 2.1 summarizes some methods used for hair detection and inpainting steps with the results obtained for each one. Most of the presented methods in this table had compared their result to DullRazor software.

Table 2.1: Comparison of different used methods on hair-removal task

Method	**Hair detection**	**Restoration**	**Database**	**Results**
DullRazor [38]. (1997)	Generalized morphological closing operator	Bilinear interpolation	5 images	Visual presentation of the segmentation
Kiani et al. [40]. (2011)	Perwitt edge detector	Color averaging	5 images	Visual presentation and comparison with DullRazor
Toossi et al. [41]. (2013)	Adaptive canny edge detector	Multi-resolution coherence transform inpainting	50 images	88.3% of diagnostic accuracy and 9.9% of error segmentation
Nguyen et al. [42]. (2010)	Universal matched filtering kernel and Gaussian fitting	Linear interpolation	not available	visual illustration on synthetic and real images
Xie et al. [43]. (2009)	Top-hat operator + elongate function for thresholding	PDE-based image inpainting	80 images: 40 with hair, 40 without hair)	5% of false hair error and 18% of misclassified

Method	**Hair detection**	**Restoration**	**Database**	**Results**
Fiorese et al. [44]. (2010)	Top-hat operator + Otzu Threshold	PDE-based image inpainting	20 images	15.6% of misclassified
Huang et al. [45]. (2013)	Multiscale matched filters	Median filtering	20 images	81% of true hair detection
Abbas et al. [48]. (2011)	Derivative of Gaussian	Coherence transport	100 images	Diagnostci accuracy of 93.3%
Mizaarlian et al. [54]. (2014)	Quaternion color curvature filter	Bilinear interpolation [38]	40 dermoscopic and 94 synthetic images	$\approx$ 85% of accuracy for hair detection and over then 90% of sensitivity for both databases
Koehoorn et al. [53]. (2015)	Gap- detection by multi-scale skeletons	Fast Marching method [57]	300 images	Visual comparison with methods presented in [38, 40, 43–45, 47].

In hair segmentation and removing, there have been many contributions and less for published papers analyzing on tubular structures and vessels. In the state-of-the-art research, the results obtained of most papers are based more on visual analysis and comparison. We notice that the majority of methods developed for skin image enhancement are based on thresholding. Despite the multitude approaches, it is very difficult to draw a clear conclusion due to the use of private databases and the application of these methods on small datasets.

2.3 Segmentation

The accurate detection of skin lesion border is the most important step and the crucial stage for classification and diagnosis. In image processing, many methods and algorithms were developed and applied in different databases. As mentioned in the previous chapter, the border detection is not so trivial and it has some shortcomings and problems [28]. Two points are related, firstly, there are the ground truth problem done by dermatologists which is difficult to discriminate by algorithms and reproduce by the human observers, where the variation in contrast or blur [58] are not visible or well explored by naked eyes. Secondly, the issue between the manual and the automated segmentation is the morphological structure of the lesion as explained by Celebi et al. [37], specially the low contrast between the lesion and the normal skin and the fuzzy lesion borders in some cases.

The multitude of lesion development and its appearance in dermoscopic images complicates and influences the choice of the best method to detect lesion border [12,28, 37]. Therefore, the current subsection is organized following three major methods sets explored in image segmentation in generally, and skin lesion images particularly. In the first step, the methods developed using total variation segmentation are presented, then followed by multiresolution analysis and finally, those using thresholding approaches. Other various methods, that do not belong to these sets are also studied and explored. Recently, Celebi et al. [33] reviewed the border lesions detection and classified them into twelve categories, such as Histogram thresholding, clustering and active contours, etc.

2.3.1 Total Variation Segmentation

In the literature, as in general image processing, many methods are developed and/or implemented for skin lesion segmentation. Using total variation regularization, Abbas et al. [47] for the segmentation part, used a modified region-based active contours (RACs) developed by Lankton et al. in [59]. The current method explored the same

concept of Chan and Vese model [60], and its generalization [61] proposed for the resolution of Mumford-Shah function [62] (see chapter 3). On a database of 320 images, the results present over than 90% true detection rate (TDR) and less than 10% of false positive rate (FPR). For the same objective, Safi et al. [63] applied another generalization of Chan and Vese Model developed by Li et al. [64] (see chapter 4). Using ABCD rule for feature extraction and SVM classifier on a database of 4240 benign and 232 malignant moles, the performance evaluation was conducted using a 10-fold cross-validation and it performed a true detection rate over than 98% for all 10 tested cases. Another extension of the model is presented recently by Kang et al. [65].

In 2009, Silviera et al. [66] compared 6 methods of segmentation, adaptive thresholding (AT), gradient vector flow, adaptive snake (AS), level set of Chan and Vese model (C-LS), expectation-minimization level set (EM-LS) and fuzzy-based split-and merge (FBSM) algorithm. The comparison shows that the best result of false positive rate (FPR) of 2.55% is given by C-LS method, but the results are lower for true detection rate (TDR) of 83.39% comparing to Adaptive snake with a TDR of 95.47%. In 2015, an extension of Chan and Vese model applied on dermoscopic images is developed [67], the proposed extension is detailed in Chapter 4.

2.3.2 Multiresolution Analysis

Multiresolution analysis is also used for segmentation of pigment skin lesions. Therefore, Castillejos et al. [68], in 2012, mixed wavelet transform [69] with Fuzzy K-Means Clustering algorithm, Fuzzy C-means algorithm and Cluster Preselection Fuzzy C-Means algorithm using all color channel for segmentation. On a database of 50 images, the diagnostic performance was quantified by the AUC measure, the best result was performed using Daubechies wavelet with an AUC value over than 0.96 for the three combinations. In another way, Ma et al. [70, 71] used wavelet decomposition banks [72] to discriminate melanoma and non-melanoma cases, the artificial neural network (ANN) classifier is used for classification. The authors applied the approach on a database of 134 skin lesion images with 72 melanoma and 62 benign lesions. The

obtained results achieved a sensitivity of 90% and a specificity of 83%.

A comparison between wavelet [73] and curvelet transforms [74] for segmentation and identification of melanoma was implemented by Abu Mahmoud et al. [75]. Using the two layers back-propagation neural network classifier on 448 digital skin lesion images, the result showed a better performance for curvelet compared to wavelet transform. The accuracy obtained using curvelet transform is 86.57%, which is much higher than the result obtained by wavelet transform with 58.44% of accuracy. Erkol et al. [76] proposed the gradient vector flow to find the border of skin lesions under 20 iterations. On a database of 100 dermoscopic images (30 malignant melanoma and 70 benign lesions), 13.77% of error detection is obtained.

2.3.3 Thresholding Approaches

The idea of thresholding method is one of the simplest approaches of segmentation. The structure of these kind of methods is mostly to separate the image following some limits applied on gray-scale into binary image. Mostly, these methods are complemented by other approaches as morphological operators.

The thresholding approaches by morphological operators segmentation is one of the most known method and used in border detection in different imaging databases [77–82]. In skin cancer images, the morphological segmentation was used by Ganster et al. [83]. The authors explored a gray-scale morphology for segmentation. The method based on three algorithms of thresholding, global thresholding, dynamic thresholding and they also explore the blue color channel of RGB and CIE-Lab color space on 4000 lesion images, and after rejection of 159 images considered as rejected due to segmentation failures, they obtained around 96% of correctly segmented skin lesion images. Earlier, Shmid [84] used anisotropic diffusion and morphological flooding on dermoscopic lesion detection. In [66], the adaptive thresholding showed a potential result compared to other used methods in terms of TDR and FPR performances. It performed a better result of true detection rate and false detection rate in benign and malignant

melanoma than gradient vector flow method, and it showed an equivalent result comparing to other methods. In 2013, Celebi et al. [82] proposed an automated fusion of thresholding method with a Markov random field, applied on 90 dermoscopic images (23 malignant melanoma and 67 benign lesions), and compared to the state of the art methods expressing the result using exlusive-OR errors of $9.16 \pm 5.21\%$.

Otsu thresholding segmentation [85] is developed and applied for automatic border detection in dermoscopic images [75, 86–89]. This method is always combined with other methods to perform the segmentation. In Abbas et al. [88], the authors proposed a combined algorithm of Otsu thresholding algorithm and a morphological reconstruction-based algorithm. The authors presented a result of 92.10% of TDR and 6.41% of FPR on a database of 100 dermoscopic images.

2.3.4 Other Segmentation Methods

Genetic algorithms [90] were used by Xie et al. [91], where a self-generating neural network and the genetic algorithm were combined for the segmentation of dermoscopic images. Watershed technique [79, 92] was also used for lesion segmentation by Wang et al. [93]. It was applied on 100 skin lesions and had a percentage error of 15.98%. An anisotropic mean shift based on Fuzzy C-Mean (FCM) algorithm variant is used by Zhou et al. [94], where the authors utilized an anisotropic mean shift algorithm coupled with fuzzy c-means for the segmentation. Sobiecki et al. [95] used Gap-sensitive segmentation on digital images. The authors also applied their method on skin cancer images. Glaister et al. [96] used TDLS algorithm for textural feature extraction joined with TD metric to calculate the dissimilarity of the texture. Applied to 126 standard camera images, the segmentation results achieved an accuracy of detection of 98.3%, a sensitivity of 91.2% and a specificity of 99%. An unsupervised segmentation algorithm using k means clustering under spatial constraints was also proposed by Zhou et al. [97]. Qi et al. [98] applied a fully deep constitutional neural network to automatically segment melanoma. the authors learned their model on 2000 training images and tested on 600 images, then validated on 150 images. However, the authors illustrate

visually their results and they did not present any performance due to the small dataset used for learning step.

Table 2.2 summarizes the different methods of segmentation explored for skin lesion images. For each paper, the method used, the result obtained and the size of the dataset (number of images) are mentioned.

Table 2.2: Comparison and summary of some different methods used for segmentation

Authors	**Segmentation method**	**Database**	**Results**
Abbas et al. [47] (2011)	Region-based Active Contours [59]	320 images	TDR of 92.17% and FPR of 5.62%
Safi et al. [63] (2011)	Multipahse segmentation with TV and H^1 regularization [64]	4472 images	Accuracy of 98.57% with a TDR of 99.1%
Casttilejos et al. [68] (2012)	Wavelet Transform mixed with three variants of FCM algorithm	50 images	AUC value over then 0.96
Clawson et al. [99] (2009)	Harmonic wavelet transform [100]	30 images	With ground truth of two experts: 1St- Acc: 93.3%, Sen: 50%, Spe: 100%. 2nd-Acc: 93.3%, Sen: 95.2%, Spe: 88.9%
Ma et al. [71] (2013)	Wavelet decomposition bank [72]	134 images	Spe: 90.32%, Sen: 83.33% and Area of ROC: 89.07%.
Ganster et al. [83] (2001)	Gray-scale morphological segmentation	4000 images	Around 96% of correct segmentation.

Authors	Segmentation method	Database	Results
Abu Mahmoud [75] (2013)	Wavelet and curvelet transforms	448 images	Using ANN, 58.44% and 86.57% of accuracy for wavelet and curvelet transforms resp.
Glaister et al. [96] (2014)	Texture Distinctiveness Lesion Segmentation (TDLS) algorithm	126 images	Accuracy detection of 98.3%, a sensitivity of 91.2% and a specificity of 99%.

The majority of developed methods for segmentation step are based on usual methodologies developed in image processing segmentation. we can notice that Safi et al. [63] claimed an accuracy of 98.57% on a database 4472 images, however the authors did not highlight the parameters used in the model knowing that the model is an extension of Chan and Vese model which is dependent on parameters chosen. It can be seen also that Clawson et al. [99], on a database of only 30 images, the results obtained by their model shows a big difference sensitivity performance between the ground truth of two experts (50% and 95.2%). We noted also that the accuracy is affected by the difference between malignant and benign lesions. Therefore, there is a need to develop an adapted and specified method for skin lesions. From the literature, it can be seen that majority of contributions used a private databases which is very hard to re-implement the different methods. It can be seen also that the segmentation step development for skin cancer is not highlighted since few years. In the current work, an adequate and accurate segmentation for skin cancer using an extension of Chan and Vese model is developed.

2.4 Feature Extraction

Feature extraction of melanoma is the most important stage for the classification and diagnosis step (next stage). The main task of this step is to extract the discriminant features to aid the separation of malignant and benign skin lesions. To correctly diagnose

and classify the lesion, the features extracted have to represent in the best way the characteristics of the tumor that can be used and understood by the computer. In hospitals as mentioned before, medical doctors use two famous scoring systems as features, ABCD criteria (or rule) [2, 13] and 7-point checklist [31]. The ABCD rule (Asymmetry, Border irregularities, Color variation and Diameter) is more used and explored than 7-point checklist.

In the literature, most of the papers develop their methods according to one or more points of ABCD rule, specially Asymmetry [20, 89, 101–105], Border irregularities [20, 63, 70, 82, 88, 105–111] and Color variation [20, 63, 88, 104, 112–120]. The non common utilization of the Diameter does not mean that it is useless comparing to the other ABCD rule points, but in most of the cases the diameter is missed data. Nevertheless, it was used by Shen et al. [20].

Many other methods of image processing are also used, specially textural and structural features. In Abbas et al. [121], in addition to color-related features, the authors combined them with textural ones extracted from Steerable Pyramids Transformation (SPT) algorithm, and performed a sensitivity of 89.28%, a specificity of 93.75% and an area under AUC of 0.986. Abu Mahmoud et al. [75] explored discrete wavelet and discrete curvelet transforms as features for melanoma recognition. For smart-phone-based real-time system, Abuzaghleh et al. [118] proposed fast Fourier transform (FFT) mixed with discrete cosine transform applied on color and shape for feature extraction. Earlier in 2009, Clawson et al. [99] used Harmonic Wavelet Transform [100] for border smoothness features on 30 dermoscopic images. Using the ground truth of two experts and C5 algorithm with 10-fold cross-validation, the results show an accuracy of 93.3% for both experts, and a sensitivity of 50% and 95.2% and a specificity of 100% and 88.9% for the ground truth of expert 1 and expert 2, respectively. Codella et al. [122] used Sequential Pattern Mining (SPAM) algorithm to learn dictionaries constructed on color (RGB) and gray level spaces of the dataset. The authors applied the approach on ISIC database of 4624 images with 334 melanoma, 144 atypical nevi and 2146 benign

lesions. Using SVM classifier, the results obtained showed an accuracy of 93.1%, a sensitivity of 94.9% and a specificity of 92.8%. Local Binary Pattern (LBP) [123, 124] operator is also used for feature extraction on dermoscopic images by Gonzáles et al. [125] and Adjed et al [126].

Sadghi et al. [127], to classify absent, regular and irregular streaks, which are important for melanoma detection inspired from 7-point checklist system, used the orientation and spatial arrangement of streak lines. Takruri et al. [128] proposed the extraction of features on wavelet or curvelet coefficients applied on gray scale lesions with color features obtained from original images. Using SVM classifier, the results performed an accuracy of 87.1%, a sensitivity of 86.4% and a specificity of 88.1% for the system based on wavelet features and an accuracy of 83.6%, a sensitivity of 76.9% and a specificity of 85.4% for the system based on curvelet features.

Cavalcanti et al. [129] is a typical work following all the steps of ABCD rule on standard images database. Therefore, for asymmetry they used two axis passing through the center of the pigment, and magnitude of gradient using Sobel operator. They explored the values of pixel intensities in color variation channel for color features. However, on standard camera images, the morphological and vascular structures are not visible. On a database of 220 images (138 melanoma and 82 benign lesions), they performed an accuracy of 93.63%, a sensitivity of 94.92% and a specificity of 91.46% using kNN classifier. Exploring the same method, Amelard et al. [105] extracted features using multi-stage illumination algorithm and defined a set of high level intuitive features to quantify the asymmetry and border irregularities as [129]. They applied their algorithm on a database of 206 standard digital camera images. Using SVM classifier, the results obtained performed an accuracy of 81.26%, a sensitivity of 84.04% and a specificity of 79.91%. Sabbaghi et al. [130] explored the Bag-Of-Feature using SIFT (Scale Invariant Feature Transform) descriptor mixed color identification [131] to extract the features. Two classifiers are used to evaluate the proposed method. Firstly, they employed linear SVM for the classification step, and secondly, they used Stacked Sparse Auto-Encoder (SSA) neural network variant. The results achieved by these methods on a database of 814 images are 85% and 95% of accuracy for SVM and SSA, respectively. Bi et

al. [132] proposed a multi-scale lesion-biased representation (MLR) and performed the classification under joint reverse classification (JRC) model. The results obtained on a database of 200 dermoscopic images are 87.50 of sensitivity, 93.13% of specificity and 90.31 of accuracy. However, the authors did not cross validate the obtained results of the proposed method. Recently, Li and Shen [133] used deep learning network to detect melanoma. Applying straight-forward CNN algorithm for segmentation and lesion index calculation unit for classification. On ISIC database containing 2750 images, the method showed an accuracy of 92.2%, a sensitivity of 78.9% and a specificity of 97.5%. On the same database, Gal et al. [134] and Lopez et al. [135] proposed a bayesian convolutional neural network and convolutional neural network, respectively, Gal et al. obtained an AUC of 0.75 and Lopez et al. obtained an accuracy of 81%. In the same idea, Esteva et al. [136] applied a deep convolutional neural network on a database of 129450 clinical images into $2,032$ different diseases. Their results were compared to 21 board-certified dermatologists.

Table 2.3: Comparison and summary of some different methods used for feature extraction and their obtained results

Authors	**feature extraction method**	**Database**	**Obtained results**
Codella et al. [122] (2015)	Sequential Pattern Mining	2624 images	Accuracy of 93.1%, Sensitivity of 94.9% and specificity of 92.8%
Abuzaghleh [118] (2014)	Fast Fourier transform mixed with discrete cosine transform	200 images	90.6%, 91.3% and 97.7 of accuracy of common, atypical and melanoma resp.
Abbas et al. [121] (2013)	Combination of color-related feature and Treeble Pyramid transformation	1039 images	Sensitivity of 89.28%, specificity of 93.75% and area under AUC of 0.986.

Authors	**feature extraction method**	**Database**	**obtained results**
Sadghi et al. [127] (2013)	Spatial arrangement and orientation of streak lines to detect regular and irregular streaks	945 images	Accuracy of 78.3% with AUC od 83.2% for absent/present and an accuracy of 83.6% with AUC of 88.9% for regular/irregular.
Takruri et al. [128] (2014)	Wavelet and curvelet features	448 images	Wavelet: Acc: 87.1%, Sen: 86.4% and Spe: 88.1%. Curvelet: Acc: 83.6%, Sen: 76.9% and Spe: 85.4%
Cavalvanti et al. [129] (2011)	Computerization of ABCD rule	220 images	An accuracy of 93.63%, a sensitivity of 94.92% and a specificity of 91.46%
Amelard et al. [105] (2014)	Multi-stage illumination algorithm	206 images	An accuracy of 81.26%, a sensitivity of 84.04% and a specificity of 79.91%.
Sabbaghi et al. [130] (2016)	SIFT mixed with color identification algorithm under SVM and SSA classifiers.	814 images	With SVM An accuracy of 85%, and with SSA an accuracy of 95% a sensitivity of 94.9% and a specificity of 95.4%.
Bi et al. [132] (2016)	MLR method under JRC model for classification.	200 images	An accuracy of 90.31%, a sensitivity of 87.50% and a specificity of 93.13%.
Li et al. [133] (2017)	CNN algorithm for segmentation and lesion index calculation unit for classification.	2750 images	An accuracy of 92.2%, a sensitivity of 78.9% and a specificity of 97.5%.

Authors	feature extraction method	Database	obtained results
Codella et al. [137] (2017)	combination of hand-coded feature extractors, sparse-coding methods, SVMs, with fully CNN	1279 images	An accuracy of 76%, a sensitivity of 82% and a specificity of 62%.

It can be seen that the most of recent contributions of skin cancer recognition are developed in feature extraction area such as presented in table 2.3. However, the results are still should improved specifically the decrease of false negative cases such as the results obtained by Li et al. [133] using CNN method. Another problematic can be seen in the literature is that most of contributions are not validating their obtained results such as Cavalvanti et al. [129] and Bi et al. [132]. Therefore, there is a need to develop and adapt a new approach of feature extraction following a rigorous methodology of work by validation and parameters highlighting.

2.5 Classification

The classification and diagnosis is the last step of the CAD system on melanoma recognition. The classification stage uses the selected features in the previous section to separate the database into different groups. The result can be binary as malignant / benign or typical / atypical, ternary as common nevus / atypical nevus / melanoma, or more than three groups.

To accomplish the classification task, many classifier methods are explored and used depending on the descriptor used for feature selection. The performance of the whole proposed method depends extremely on the couple descriptor / classifier. The review of Korotkov et al [12] enumerated several methods of classification used in the literature. According to the classifier used, many different performance metrics are used as

accuracy, TDR, FPR or AUC. These performance metrics are explained and detailed in subsection 3.5.4.

Support Vector Machine (SVM) classifier [138] and Artificial Neural Network methods (ANN) [139] are the most used for classification of skin cancer images. The mathematical theory of these two classifiers are explained in the next chapter. Thus, the SVM and the ANN classifiers divide the dataset into two sets, one for training and the other for tests. In most of cases, 70% of the data is used for training and 30% is used for tests. The SVM classifier was used in [19, 56, 63, 104–106, 111, 118, 119, 122, 126, 130, 140–146] and ANN was used in [71, 75, 111, 112, 122, 125, 130, 143, 144, 146–148]. In addition to these two classifiers, there are also many other classifiers used in melanoma recognition such as the k-Nearest Neighbor (kNN) classifier [83, 129, 140], Discriminant Analysis [45, 58, 144], Decision trees [1, 8, 129], Regression Analysis [111, 147, 148] and AdaBoost [1, 8, 140]. The review of the comparative studies achieved by Masood et al. [32] concluded that SVM classifier outperforms decisions trees, and many other statistical classifiers.

Abuzaghlegh et al. [118], proposed to classify the PH^2 Database [149] into binary and ternary results. The ternary results used to classify between typical, atypical or melanoma and the binary is to classify only between normal and abnormal lesions. The authors used SVM classifier using 75% for training and 25% for tests. On the same database (PH^2), Barata et al. [141] used SVM classifier with the χ^2 kernel, the performance of the contribution is computed by the adjusted accuracy calculated with some interval of accuracy metric. In the same work, the authors are applied also their method on bigger database from the ERDA database [150]. AdaBoost with C4.5 decision trees was used by Capdehourat et al. [1] and performed their results by specificity and sensitivity metrics.

Table 2.4 summarizes the different classifier utilized in the literature for classification and recognition of melanoma. As already mentioned above, it can be seen easily from the table that the most used classifiers are SVM and ANN.

Table 2.4: Summary of the most used classifiers in skin cancer recognition

Classifier	Author references
Support Vector Machine	[19,56,63,104–106,111,118,119,122,126,128, 140–146]
Artificial Neural Network	[71,75,91,106,111,112,122,125,143,144,146–148,151]
k-Nearest Neighbor	[83,129,140,146]
Decision Trees	[1,8,99,129]
Discriminant Analysis	[45,58,144]
Regression Analysis	[111,147,148]
AdaBoost	[1,8,121,140].

2.6 Summary

In the literature, skin cancer detection and classification is developed and explored by many researchers. There are two major topics where the contributions are focused. These two topics are the lesion segmentation and the descriptors for feature extraction. The multitude of artifacts in skin lesion images increases the contributions in image enhancement, specially for hair removing and blood vessels. Computer Aided Diagnosis systems for pigmented skin lesions have achieved good performances. However, the results obtained and methods proposed cannot provide the best diagnostic results as clinicians, they are only used as second opinions during screening procedure [28].

The segmentation was studied in different views. Many approaches and methods were adapted and/or developed. Therefore, as it is detailed in section 2.3, the segmentation methods used the total variation methods following Mumford and Shah theory, specially Chan and Vese model and its extensions. The multiresolution analysis was also used for pigment lesion segmentation as wavelet and curvelet transforms. The thresholding methods were also mostly used for segmentation.

The choice of the descriptor to use and/or to develop for feature extraction is more

difficult and more complicate than other steps. Unlike segmentation, where the objective is to find the border lesion, the descriptor's objective is to develop an adaptive method to discriminate widely the lesions. It can be textural, statistical, structural or geometrical features. In skin cancer images, many feature extraction methods are formulated and developed from the two scoring systems used by clinicians in the hospitals, ABCD rule and 7-point checklist. Other methods also used different mathematical tools and descriptors such as Fourier, wavelet and curvelet coefficients. The major limitation of ABCD rule and 7-point checklist is that the two systems are based on visual interpretation, which is subjective between dermatologists. The cancerous lesions are random biological phenomena manifesting various structures in sizes, shapes and densities. Therefore, there is a need to perform and develop an accurate descriptor. Two research directions should be further investigated which are structural and textural features. The structure of lesion boundaries and the texture inside the lesions have an important information for discrimination and characterization of melanoma. Wavelet coefficients are ideal for single point discrimination but not for edges which characterize the lesion boundaries. Thus, curvelet coefficients can achieve better characterization. In addition to curvelet, a fusion of these coefficients with textural information of the lesion need to be investigated. On the other side, the investigation of the geometrical information from the borders with a new approach challenging irregular versus smooth border is also another direction for the discrimination of melanoma.

Various classifiers are used in CAD systems for skin cancer recognition. Artificial Neural Network and Support Vector Machine are the most common used. Commonly, skin cancer lesions are classified following two or three classes which are benign / malignant and nevus / atypical / melanoma.

The different metric performances used for each classifier makes harder the comparison between the results of the different proposed methods. In addition to that, the absence of a large public available benchmark dataset accompanied by the ground truth and the diagnosis from several dermatologists makes really hard, even impossible to compare objectively the approaches developed in the literature.

CHAPTER 3

MATHEMATICAL TOOLS

3.1 Overview

This chapter presents the theoretical background of the explored methods in the current work which is divided into three main parts. Section 3.2 provides total variation theory of Mumford and Shah and Chan and Vese model well, used for segmentation in image processing [152, 153]. The multiresolution analysis is presented in section 3.3. It provides an overview of the history of multiresolution analysis and the need of the development of new applications. It starts by introducing Fourier transform, followed by wavelet and ridgelet and finally by curvelet transforms. Section 3.5 gives an introduction of the mathematical background of the two used classifiers, Artificial Neural network and Support Vector Machine. Finally, this chapter ends by a short summary given in section 3.6.

3.2 Total Variation

In classical analysis, the total variation for function f for one variable defined on the interval $[a, b] \subset \mathbb{R}$, is given by the following formula:

$$TV(f) = \sup_{I} \sum_{i=0}^{I} |f(x_{i+1}) - f(x_i)| \tag{3.1}$$

where $I = \{I_1, I_2, ..., I_p\}$ is a partition of $[a, b]$ for $i \in \{1, ..., p\}$, $x_i \in I_i$.

The total variation of function $f \in \mathbb{R}^n$ where $n > 1$ used in the current work is defined as follow:
Let Ω be an open subset of $\mathbb{R}^n$ and $f \in L^1(\Omega)$, then the total variation is:

$$TV^n(f) = \sup \Big\{ \int_\Omega f(x)\ \text{div}\phi(x)dx;\ \ \phi \in \mathcal{C}_c^1,\ \|\phi\|_{L^\infty(\Omega)} \leq 1 \Big\} \tag{3.2}$$

where $\mathcal{C}_c^1$ is the set of continuously differentiable functions of compact of Ω and $\|\phi\|_{L^\infty(\Omega)}$ is the essential infimum norm.

3.2.1 Mumford Shah Function

Mumford and Shah applied the total variation for image segmentation in 1989 [62]. Let $R \in \mathbb{R}^2$ the domain divided in n disjoint subsets R_i where a smooth function f_i is defined and Γ will be the union of boundaries parts of the R_i inside R . Let I be the given image and f a differentiable function on R, then the energy to minimize is :

$$E(f, \Gamma) = \mu^2 \int \int_{\mathbb{R}} (f - I)^2 dxdy + \int \int_{R-\Gamma} \|\nabla f\| dxdy + \nu|\Gamma| \tag{3.3}$$

where $|\Gamma|$ represents the total length of the curve Γ, μ and ν are the regulation parameters.

3.2.2 Chan and Vese Model

To minimize the given energy in equation (3.3), Chan and Vese [60] proposed to minimize first, the following energy function:

$$F_C(C) = \lambda_1 \int_{inside(C)} |I(x,y) - c_1|^2 dxdy + \lambda_2 \int_{outside(C)} |I(x,y) - c_2|^2 dxdy \tag{3.4}$$

where C is a given curve in the domain R and c_1, c_2 are the averages of I inside and outside C. Using this formulation, the function $F_C(C)$ is minimized on the boundary of the object.

Therefore, the energy functional is defined by $F(c_1, c_2, C)$ given below:

$$F(c_1, c_2, C) = \mu \,\text{Length}(C) + \nu \,\text{Area}(inside(C)) + F_C(C) \tag{3.5}$$

Using a zero level set of Lipschitz function $\phi : \Omega \to \mathbb{R}$, then :

$$\begin{cases} C = \partial\omega = \{(x, y) \in \Omega;\ \phi(x, y) = 0\} \\ inside(C) = \omega = \{(x, y) \in \Omega;\ \phi(x, y) > 0\} \\ outside(C) = \Omega\backslash\omega = \{(x, y) \in \Omega;\ \phi(x, y) < 0\} \end{cases} \tag{3.6}$$

Where $\omega \in \Omega$ and $C = \partial\omega$.

Using the heaviside function H and the dirac function δ_0 given in equation (3.7), the curve C and the areas inside and outside the level set function ϕ given in equation (3.6) are expressed by equation (3.8)

$$H(z) = \begin{cases} 1 & \text{if} \quad z \geq 0 \\ 0 & \text{if} \quad z < 0 \end{cases} \qquad \delta_0 = \frac{d}{dz} H(z) \tag{3.7}$$

$$\begin{cases} C = \text{Length}(\phi = 0) = \int \delta_0(x, y)|\phi(x, y)|dxdy \\ \text{Inside}(C) = \text{Area}(\phi(x, y) > 0) = \int_\Omega H\big(\phi(x, y)\big)dxdy \\ \text{Outside}(C) = \text{Area}(\phi(x, y) < 0) = \int_\Omega \Big(1 - H\big(\phi(x, y)\big)\Big)dxdy \end{cases} \tag{3.8}$$

Then, equation (3.4) is also expressed by the heaviside function H:

$$F_C(c) = \lambda_1 \int_\Omega |I(x, y) - c_1|^2 H\big(\phi(x, y)\big)dxdy + \lambda_2 \int_\Omega |I(x, y) - c_2|^2 \big(1 - H(\phi(x, y))\big)dxdy \tag{3.9}$$

Therefore, the energy given in equation (3.5) becomes:

$$\begin{aligned} F(c_1, c_2, \phi) &= \mu \int \delta_0(x,y)|\phi(x,y)|dxdy + \nu \int_\Omega H\big(\phi(x,y)\big)dxdy \\ &\quad +\lambda_1 \int_\Omega |I(x,y) - c_1|^2 H\big(\phi(x,y)\big)dxdy \\ &\quad +\lambda_2 \int_\Omega |I(x,y) - c_2|^2 \big(1 - H(\phi(x,y))\big)dxdy \end{aligned} \tag{3.10}$$

where,

$$c_1 = \frac{\int_\Omega I(x,y)H(\phi(x,y))}{\int_\Omega H(\phi(x,y))} \tag{3.11}$$

$$c_2 = \frac{\int_\Omega I(x,y)\big(1 - H(\phi(x,y))\big)}{\int_\Omega \big(1 - H(\phi(x,y))\big)} \tag{3.12}$$

The energy to minimize for the segmentation of Chan and Vese model is given by equation (3.10).

3.3 Multiresolution Analysis

In this section, the multiresolution analysis is introduced. Mathematical theories of Fourier, wavelet, ridgelet and curvelet transforms are presented.

The Fourier transform has the ability to represent any integrable function in the frequency domain with a limitation of stationarity in time [154]. With wavelet transform, the time representation is resolved, however the line singularity of edges in wavelet transforms need many coefficients. An extension was presented which is ridgelet transform for detection of edges with less coefficients. The incapability to detect the angle of edges using ridgelet transform, curvelet transform was introduced to fit better the curves and edges. Curvelet and wavelet transforms are used in the proposed work, they are introduced in next sections and used in the next chapter.

3.3.1 Fourier Transform

Let $f : \mathbb{R} \to \mathbb{C}$ an integrable function, the Fourier transform of f is conventionally noted $\hat{f}$ decomposes into frequencies. Therefore, the function f is the continuous-time function defined in spatial domain, and $\hat{f}$ is its Fourier transform defined in frequency domain given by the following equation:

$$\hat{f}(\xi) = \int_{-\infty}^{\infty} f(x)\, e^{-2\pi x i \xi} dx \tag{3.13}$$

The inverse Fourier transform of $\hat{f}$, under suitable conditions is given by:

$$f(x) = \int_{-\infty}^{\infty} f(\xi)\, e^{2\pi i x \xi} d\xi \tag{3.14}$$

This transform is an extension of Fourier series applied on periodic functions using the properties of sine and cosine. Therefore, suppose that T is large enough that the interval $[-T/2, T/2]$ contains F non identically zero. Then, the nth Fourier coefficients c_n is given by the following equation:

$$c_n = \frac{1}{T} \int_{-T/2}^{T/2} f(x)\, e^{-2\pi i (n/T) x} dx \tag{3.15}$$

Equation (3.14) can be written using Fourier coefficients. Then, lets $\xi_n = n/T$ and $\Delta\xi = 1/T$:

$$f(x) = \sum_{n=-\infty}^{\infty} \hat{f}(\xi_n)\, e^{2\pi i \xi_n x} \Delta x = \sum_{n=-\infty}^{\infty} c_n\, e^{2\pi i (n/T) x} \tag{3.16}$$

In signal and image processing, the discrete Fourier transform (DFT) is applied. In the one-dimensional case (signals), the Fourier transform is given by the function f above. This signal is divided into N sequences denoted $f_0, f_1, ..., f_{N-1}$. Then the DFT of f is:

$$\hat{f}_k = \sum_{n=0}^{N-1} f_n\, e^{-2\pi i k n / N}, \quad k \in \mathbb{Z} \tag{3.17}$$

The inverse DFT is as continuous case given by the following equation:

$$f_n = \frac{1}{N} \sum_{k=0}^{N-1} \hat{f}_k \, e^{2\pi i k n / N} \tag{3.18}$$

For image which is 2 dimension matrix $M \times N$, the DFT of the function $f(x, y)$ is denoted by F(m,n) given by:

$$F(m, n) = \sum_{x=0}^{M-1} \sum_{y=0}^{N-1} f(x, y) \, e^{-2\pi i (xm/M + yn/n)} \tag{3.19}$$

where $m = 0, 1, ..., M-1$ and $n = 0, 1, ..., N-1$.

By the same, the inverse DFT in 2 dimensions is given by the function f below:

$$f(x, y) = \frac{1}{MN} \sum_{m=0}^{M-1} \sum_{n=0}^{N-1} F(m, n) \, e^{2\pi i (xm/M + yn/n)} \tag{3.20}$$

Different algorithms of fast Fourier transforms were implemented and combined with band filtering and convolutions. However, the Fourier transform indicates the spectral information without the instant when it happens [155]. In image implementation, Mallat [73] noticed that an apple in the corner of a given image required many Fourier coefficients to represent a localized event. Indeed, the Fourier transform $\hat{f}(\xi)$ depends on the values $f(t)$ for all times $t \in \mathbb{R}$. Therefore, to analyze or represent any local property of $f(t)$ from $\hat{f}(\xi)$ is difficult.

3.3.2 Wavelet Transform

Wavelet transform was introduced by Grosmann and Morlet [156] using translation and dilations on a 1square integrable function $\psi \in L^2(\mathbb{R})$. The wavelet transform is defined by the following formula:

$$\psi_{a,b}(x) = \frac{1}{\sqrt{a}} \psi\Big(\frac{t-b}{a}\Big) \tag{3.21}$$

where $a > 0$ defines the scale and b the shift.

A multiresolution approximation of $L^2(\mathbb{R})$ is a sequence $(V_j)_{j\in\mathbb{Z}}$ of closed subspaces of $L^2(\mathbb{R})$, such that:

$$\{0\} \subset \cdots \subset V_1 \subset V_0 \subset V_{-1} \subset \cdots \subset L^2(\mathbb{R}) \tag{3.22}$$

Let $\phi(x)$ be a real square integrable function defined by:

$$\phi_{j,k}(x) = \sqrt{2^j}\phi(2^j x - k), \quad k \in \mathbb{Z} \tag{3.23}$$

Then, $\{\phi_{j,k}\}_{j,k\in\mathbb{Z}}$ is the orthonormal basis of V_j [69].

All the functions expressible with this basis are referred to the closed span of the expansion set:

$$V_j = \text{Span}\{(\phi_{j.k}, k \in \mathbb{Z})\} \tag{3.24}$$

where if $f(x) \in V_j$, then $f(x) \in \text{Span}\{(\phi_{j.k}, k \in \mathbb{Z})\}$, and $f(x) = \sum_k \alpha_k \phi_{j,k}(x)$.

The subspace of $L^2(\mathbb{R})$, W_j designs the orthogonal complements of the subspaces V_j defined above, such that:

$$V_j \oplus W_j = V_{j-1} \tag{3.25}$$

In multiresolution analysis, the subspaces V_j are generated by the function $(\phi_{j,k})_{k\in\mathbb{Z}}$ and The subspace W_j is generated by a scaling function $(\psi_{j,k})_{k\in\mathbb{Z}}$ as given below:

$$W_j = \text{Span}\{(\psi_{j.k}, k \in \mathbb{Z})\} \tag{3.26}$$

then, the subspace V_j represents the large scale and W_j represents the small scale (details).

Let $f(x)$ be a one-dimensional discrete function as sequence of numbers, the discrete wavelet transform coefficients are defined as:

$$C_\phi(j_0,k) = \frac{1}{\sqrt{M}} \sum_{x=0}^{M-1} f(x)\phi_{j_0,k}(x) \tag{3.27}$$

$$D_\psi(j,k) = \frac{1}{\sqrt{M}} \sum_{x=0}^{M-1} f(x)\psi_{j,k}(x) \tag{3.28}$$

where $j > j_0$, M is power of 2 which ranges from 2 to $j-1$ and $C_\phi(j_0,k)$, $D_\psi(j,k)$ are the approximation and details coefficients respectively. Using these coefficients, the signal function $f(x)$ can be reconstructed as:

$$f(x) = \frac{1}{\sqrt{M}} \sum_k C_\phi(j_0,k)\phi_{j_0,k}(x) + \frac{1}{\sqrt{M}} \sum_{j=j_0}^{\infty} \sum_k D_\psi(j,k)\psi_{j,k}(x) \tag{3.29}$$

The implementation of wavelet transform was presented by Mallat [69] introducing a set of filters $(h_l)_{l\in\mathbb{Z}}$ and $(g_l)_{l\in\mathbb{Z}}$ where:

$$\phi_{j,k} = \sum_l h_l \phi_{j+1,2k+l} \tag{3.30}$$

$$\psi_{j,k} = \sum_l h_l \psi_{j+1,2k+l} \tag{3.31}$$

and

$$h_l = (-1)^n g_{1-l} \tag{3.32}$$

Therefore, the approximation and details coefficients are computed.

In two dimensions case, there are one scaling function $\phi(x,y)$ and three directional

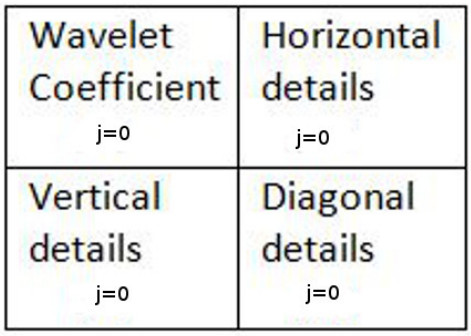

Figure 3.1: Wavelet representation scale j=0

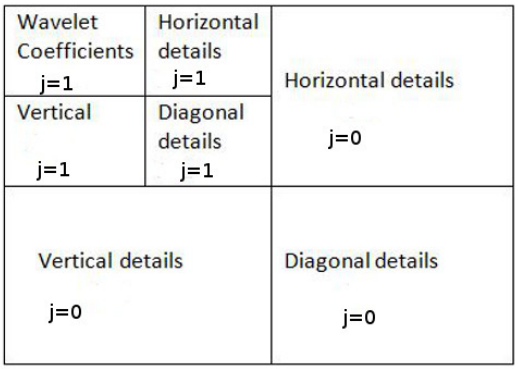

Figure 3.2: Wavelet representation scale j=0 and j=1

wavelets as defined below:

$$\begin{cases} \phi(x,y) = \phi(x)\phi(y) \\ \psi^H(x,y) = \psi(x)\phi(y) \\ \psi^V(x,y) = \phi(x)\psi(y) \\ \psi^D(x,y) = \psi(x)\psi(y) \end{cases} \tag{3.33}$$

where ψ^H, ψ^V and ψ^D measure the horizontal, vertical and diagonal variation respectively as represented in figures 3.1 and 3.2.

Finally, the wavelet coefficients of a given image I $(M \times N)$ are computed using the following formulas:

$$W_{\phi}(j,k) = \frac{1}{\sqrt{MN}} \sum_{x=0}^{M-1} \sum_{y=0}^{N-1} I(x,y)\phi_{j,k}(x,y) \tag{3.34}$$

$$W_{\psi}^{H}(j,k) = \frac{1}{\sqrt{MN}} \sum_{x=0}^{M-1} \sum_{y=0}^{N-1} I(x,y)\psi_{j_k}^{H}(x,y) \tag{3.35}$$

$$W_{\psi}^{V}(j,k) = \frac{1}{\sqrt{MN}} \sum_{x=0}^{M-1} \sum_{y=0}^{N-1} I(x,y)\psi_{j_k}^{V}(x,y) \tag{3.36}$$

$$W_{\psi}^{D}(j,k) = \frac{1}{\sqrt{MN}} \sum_{x=0}^{M-1} \sum_{y=0}^{N-1} I(x,y)\psi_{j_k}^{D}(x,y) \tag{3.37}$$

The potential of wavelet representation had a wide impact in theory and in practice. It's used for non-linear approximation, compression and image denoising on different databases. But wavelet is less efficient in some cases for line singularities [157].

3.3.3 Ridgelet Transform

The Ridgelet transform was introduced by Candés and Donoho [158] and Finite ridgelet transform for image representation [157] by Do and Vetterli. Ridgelet transform has the ability to detect line singularities.

The continuous ridgelet transform is defined for each $a > 0$, $b \in \mathbb{R}$ and $\theta \in [0, \pi/2]$ by the bivariate function $\psi_{a,b,\theta} : \mathbb{R}^2 \to \mathbb{R}^2$:

$$\psi_{a,b,\theta}(x) = a^{-1/2}\psi\Big(\big(x_1\cos(\theta) + x_2\sin(\theta)\big)/a\Big) \tag{3.38}$$

This function is an extension of wavelet transform, where when $(x_1\cos(\theta) + x_2\sin(\theta)$ is constant the two functions are equal. In addition to that the ridgelet transform has the ability to fit easily the lines compared to wavelet transform [158].

Let $f(x)$ be an integrable bivariate function, the ridgelet transform of f is R_f given below:

$$R_f(a,b,\theta) = \int \psi_{a,b,\theta}(x)f(x)dx \tag{3.39}$$

Do and Vetterli [157] proposed the finite ridgelet transform for image representation, they used the inner product of finite radon transform and wavelet transform.

The Ridgelet transform is efficient for the detection of straight lines, unless it is inefficient for curves fitting.

3.3.4 Curvelet Transform

The Curvelet transform was designed to represent edge and curve singularities more efficiently than previous transforms presented in this chapter. It needs fewer coefficients to describe edges and curves through the directional parameter added.

Curvelet Transform was introduced in 2000 by Candes and Donoho [159], they presented the second generation of curvelet [160] known as the fast digital curvelet transform (FDCT) in 2006, which is less redundant and it has better performances than its predecessors. Curvelets have the capability to detect finest edges, those can present more details in curvelet coefficients [161].

Curvelet transforms are defined in two dimensions, with spatial variable x and frequency-domain variable w. The polar coordinates of the frequency-domain are r and θ. Two windows $W(r)$ and $V(t)$ called *radial window* and *angular window* respectively [160]. These windows will always obeying the following admissibility conditions:

$$\sum_{j=-\infty}^{\infty} W^2(2^j r) = 1, \qquad r \in (3/4, 3/2) \tag{3.40}$$

$$\sum_{l=\infty}^{\infty} V^2(t-l) = 1, \qquad t \in (-1/2, 1/2) \tag{3.41}$$

The frequency window U_j, in Fourier domain given by equation (3.42), represents

a polar *wedge*, which is supported by $W(t)$ and $V(t)$.

$$U_j(r,\theta) = 2^{-3j/4}\big(2^{-j}r\big)V\Big(\frac{2^{\lfloor j/2\rfloor}}{2\pi}\Big) \tag{3.42}$$

At scale 2^{-j}, orientation θ_l and position $x_k(j,l)$, the curvelet transform function of $\{x=(x_1,x_2)\}$ is given by equation (3.43).

$$\varphi_{j,l,k}(x) = \varphi_j\left(R_{\theta_l}\Big(x - x_k^{(j,l)}\Big)\right) \tag{3.43}$$

Where R_θ is the rotation in radians and φ_j is the waveform and its Fourier transform $\hat{\varphi}(w) = U_j(w)$ given in equation (3.42). It is considered as *mother* curvelet in the sens that all Curvelets are calculated by rotations and translations of φ_j [160].

The curvelet coefficient, c given in equation (3.44), it is obtained by the inner product between the element $f \in L^2(\mathbb{R}^2)$ and the curvelet transform $\varphi_{j,k,l}$.

$$c(j,k,l) = \int_{\mathbb{R}^2} f(x)\overline{\varphi_{j,k,l}(x)}dx. \tag{3.44}$$

Fast Discrete Curvelet Transform (FDCT) via wrapping was introduced by Candes et al. in their second generation of curvlet [160]. This implementation is based on wrapping of Fourier samples with a 2D image as input in a Cartesian array form $f[m,n]$ where $0 \le m \le M$, $0 \le n \le N$, M and N are the dimension of the array (image). Then, the discrete coefficients of FDCT are given below:

$$c^D(j,l,k_1,k_2) = \sum_{0\le m\le M,\ 0\le n\le N} f[m,n]\varphi^D_{j,l,k_1,k_2}[m,n] \tag{3.45}$$

Equation (3.45) defines the Digital curvelet coefficients. $c^D(j,l,k_1,k_2)$ is indexed by a scale j, an orientation l and the spatial location parameters k_1 and k_2. Where φ^D_{j,l,k_1,k_2} is the digital waveform. These coefficients are used as features in the current

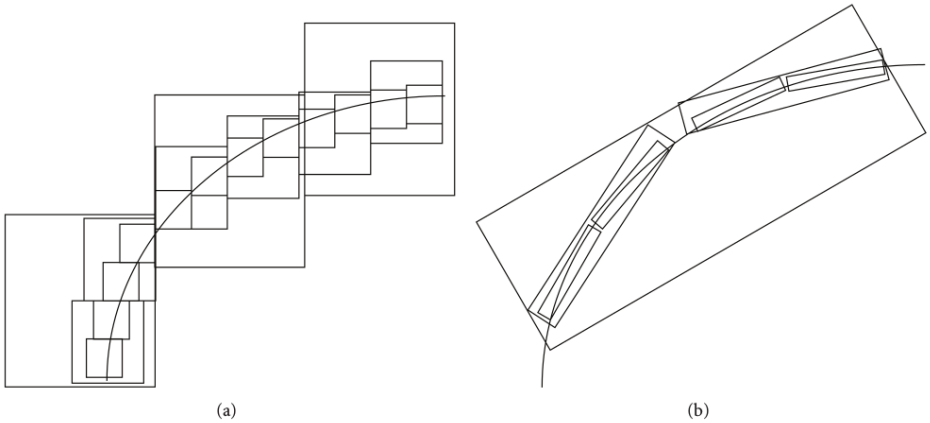

Figure 3.3: A comparison between wavelet (a) and curvelet (b) [3]

work.

Figure 3.3 illustrates the advantages of curvelet transform in curve detection compared to wavelet transform [3]. It can be seen easily that for the same curve curvelet transform is more accurate and needs fewer coefficients than wavelet transform.

3.4 Local Binary Pattern

The Local Binary Patterns (LBP) operator is used for texture description. It is one of the best performing texture descriptors and it has been widely used in multiple applications [162, 163]. This operator was developed by Ojala et al. [123, 124]. Many variants of LBP were developed, for example Heikkila et al. [164] proposed center-symmetric local binary pattern, then, Zhang et al. [165] developed a new approach replacing the neighbor pixels by the mean of the neighbors' blocks, and Wolf et al. [166] proposed novel patches based LBP where they explored the similarities between neighboring patches of pixels. The majority of these developments are applied in face detection and recognition.

The LBP operator attributes for each pixel of the image a new value from 0 to 255 depending on its neighborhood as explained below:

Let the image $I(x, y)$ and g_c denote the gray level of an arbitrary pixel (x, y), *i.e* $g_c = I(x, y)$. And let g_p denote the gray value of the local neighborhood, where P

defines the number of pixels around the point (x, y) with radius R, then :

$$\begin{aligned} g_p &= I(x_p, y_p), \quad p = 0, ..., P-1 \\ x_p &= x + R\cos(2\pi p/P) \\ y_p &= y - R\sin(2\pi p/P) \end{aligned}$$

Assuming that the local texture of the image $I(x, y)$ is characterized by the joint distribution $t(.)$ of gray values of $P + 1$ $(P > 0)$ pixels:

$$T = t(g_c, g_0, g_1, ..., g_{P-1}). \tag{3.46}$$

Without loss of information, the center pixel value can be subtracted from the neighborhood pixel values and equation (3.46) can be written as the following formula:

$$T = t(g_c, g_0 - g_c, g_1 - g_c, ..., g_{P-1} - g_c). \tag{3.47}$$

Assuming that the center pixel is statistically independent to the differences, equation (3.47) is approximated by:

$$T \approx t(g_c)t(g_0 - g_c, g_1 - g_c, ..., g_{P-1} - g_c). \tag{3.48}$$

The important information is given by the differences distribution part *i.e* $t(g_0 - g_c, g_1 - g_c, ..., g_{P-1} - g_c)$. However, the estimation of this distribution from image data is difficult. Ojala et al. [123] proposed to apply vector quantization given by the following formula:

$$t(s(g_0 - g_c), s(, g_1 - g_c), ..., s(g_{P-1} - g_c). \tag{3.49}$$

where $s(z)$,

$$s(z) = \begin{cases} 1, & z \geq 0 \\ 0, & z < 0. \end{cases} \tag{3.50}$$

Then, the generic local binary patterns operator is defined by: [167]:

$$LBP_{P,R}(x_c, y_c) = \sum_{p=0}^{P-1} s(g_p - g_c)2^p \tag{3.51}$$

According to our previous work [126], the choice of $P = 8$ and $R = 1$ is the best case for melanoma description.

Ojala et al. [124] introduced uniform pattern and invariant rotation local binary pattern. The uniform pattern variant indexed by LBP^{u2} keeps only the pattern contains in maximum 2 transition $0/1$ and/or $1/0$, this variant contains 59 combinations. The invariant rotation variant pattern indexed by LBP^{ri} has the same configuration for all rotations, it contains 36 combinations. The invariant rotation uniform pattern variant is an intersection of the uniform patterns LBP^{u2} and the invariant rotation variant LBP^{ri}> It represents only the uniform patterns which has the same configuration in all rotations, then it contains 9 combinations.

3.5 Statistical Classification and Pattern Recognition

The classification is the method which cat attribute from a set of features observed or learned a new class to the studied object not belonging to the learned set. It can be achieved using supervised learning such as Support Vector Machine and Artificial Neural Network or unsupervised learning as K-means clustering and k-Nearest Neighbors. In this section, the representation of basic ideas of support vector machine and artificial neural network are explained.

The pattern recognition is a branch of machine learning focused on description of

patterns. It may use the supervised or unsupervised recognition [168]. The supervised learning utilizes a set of training data which is properly labeled with the correct output. In the other hand, the unsupervised learning assumes training data has not been well-labeled and try to find the best pattern which can make a correct output value for the data.

Depending on the classifier used, many performance metrics can be explored to compare and analyze the obtained results such as accuracy, sensitivity, specificity. The mathematical equations of some of these metrics are given in the current chapter (see section 3.5.4).

3.5.1 Support Vector Machine

Support Vector Machine (SVM) was introduced by Vapnik and Lerner 1963, Vapnik and Chervonenskis 1964, an overview of the basic ideas of SVM and its advanced methods for large datasets are explained and detailed by Smola *et all.* [169]. The basic idea of SVM is introduced and developed in the current subsection.

Let $\{(x_1, y_1), ..., (x_m, y_m)\} \subset \mathcal{X} \times \{\pm 1\}$ a set of empirical data, where $\mathcal{X}$ is some nonempty set that the patterns x_i belongs. Let the function $f : \mathcal{X} \to \{\pm 1\}$. In this current study only the hyperplane classifier is presented. Therefore, considering the class of hyperplanes

$$(w \cdot x) + b = 0 \tag{3.52}$$

where $w \in \mathbb{R}^N$, $b \in \mathbb{R}$ (in the current work, the choice of these parameters are done using Statistic and machine learning toolbox of Matlab 2015).

The decision of SVM corresponds to the results of the following formula:

$$f(x) = sign((w \cdot x) + b) \tag{3.53}$$

To construct an optimal hyperplane, it is needed to resolve the following optimization problem:

$$\text{Minimize } \|w\|^2, \tag{3.54}$$

subject to:

$$\begin{cases} (x \cdot x_i + b) > 1, & \text{if} \quad y_i = 1 \\ (x \cdot x_i + b) \leq -1, & \text{if} \quad y_i = -1 \end{cases} \tag{3.55}$$

The two contrast given in the formula (3.55) can be expressed by:

$$y_i(w \cdot x_i + b) \geq 1 \tag{3.56}$$

The current formulation is used well in perfect separability of the data.

In the case of no-separability, the function to minimize is $|w|^2 + C \sum_{i=1}^{m} \xi_i$ where C is constant and ξ a real small positive ($\xi_i > 0$). The constraint is to verify the following formula:

$$y_i(w \cdot x_i + b) \geq 1 - \xi_i \tag{3.57}$$

To classify the more complex cases, the linear SVM classifier cannot be accurate by constructing only a hyperplane between classes. Therefore, a non-linear SVM classifier was proposed using the following mapping function ϕ:

$$x \mapsto \phi(x) \tag{3.58}$$

Then, equation decision rule, such as given by (3.53) for linear case, is formulated by the following equation:

$$f(x) = w \cdot \phi(x) + b \tag{3.59}$$

Depending on the choice of the mapping function ϕ, different variants of the non-linear SVM classifier could be built, such as the polynomial mapping and the kernel trick.

3.5.2 Artificial Neural Network

Artificial neural network (ANN) commonly referred to *neural network* has its inception for recognition as the human brain computes using different way in separate or parallel, linear and/or non-linear approaches [170]. The first interest given in ANN emerged after the introduction of simplified neurons by McCulloch and Pitts in 1943 [171].

In the literature [172], there are many different ANN models developed and implemented. In the current work, the basic idea on ANN model and the most used method variants are presented.

Let $x_i = (x_{i1}, x_{i2}, \ldots, x_{in})$ be the input vector considered as one neuron i and y_i the output where n represents the number of layers, then the result of y_i is given by the following formula [173]:

$$y_i = f(net(x_i)) \tag{3.60}$$

where f is the activation function and net is called *Network input*. It is very popular such as the sum function given below [172]:

$$net(x_i) = \sum_{j=1}^{n} w_{ij} x_{ij} \tag{3.61}$$

where $w_i = (w_{i1}, \ldots w_{in})$ is the wight vector.

For the output value y_i, the simplest way to compute the activation function is following threshold level system given below:

$$y = f_\theta(x) = \begin{cases} 1 & \text{if} \quad x > \theta \\ 0 & \text{otherwise} \end{cases} \tag{3.62}$$

where θ is the threshold. The formula given in equation (3.62) is the basic idea explored by McCulloch and Pitts in 1943. Many other variants and extensions were explored such as Hebb's method [173] and Auto Regressive (AR) model [170].

The introduction of hidden layers was introduced with the iteration concept between

two instants following some conditions. Let g called the propagation function, then:

$$net_j = g(o_j, w_j) \tag{3.63}$$

where o_j defines the output of the neuron calculated using equation (3.60).

The propagation function g depends on the acceptance condition of the output o_j and controls the evolution of the weight vector w_j. There exist different models developed in the literature. The three models are detailed below:

- Hebbian learning: The basic idea of interconnection of two neurons simultaneously.

$$w_j(t+1) = w_j(t) + x_j o_j(t) \tag{3.64}$$

- Perceptron learning rule: It was introduced for single layer for linearly independent problems.

$$w_j(t+1) = w_j(t) + \delta w_j \quad \text{with} \quad \delta w_j = \eta(o_j(t) - y_j(t))x_j \tag{3.65}$$

  where η is the learning rate.

- Back propagation learning: it defines the multiple layer and it can approximate the nonlinear functions to arbitrary accuracy.

$$\Delta w_{ij}(t+1) = \eta \frac{\delta E}{\delta w_{i,j}} + \alpha \Delta(t) \tag{3.66}$$

  where E designs the average square error, η and α are the learning rate and the momentum respectively.

The last step is the activation function as given by f in equation (3.60) is also explored to make border between classes. Two common activation functions are used [172], threshold function following some threshold θ given by $f_\theta(x)$ in equation (3.62). The second common function is the logistic which is differentiable and used in the

continuous models, as given by the following equation:

$$f(x) = \frac{1}{1 + e^{-x}} \tag{3.67}$$

Thus, f is a continuous function belonging to the interval $[0, 1]$.

3.5.3 Validation of the Results

The validation of the results step is a statistical method to prove that there is an independence in the choice of training and test sets. The cross validation method [174, 175] is the most used in skin cancer recognition. As reported by Massod et al. [32], some articles do not report comparison and cross-validation for their results. They suggested that it is imperative to present in papers these details for the validity of the used methods.

Therefore, to validate the obtained results, the random cross-validation and n-fold cross validation methods [174,175] are applied in the literature. 10-fold cross validation method is the most used in skin cancer. It was used by Barata et al. [49] for the region segmentation and lesion classification. Clawson et al. [99] and Abbas et al. [121] also applied 10-fold cross validation to validate their results. Two-cross validation is also used By Codella et al. [122]. Recently Barreiro et al. [19] used K-fold cross validation to present their result under ABCD rule for feature extraction and sensitivity, specificity and accuracy metrics to assess the result. The value of K began from 3 to 15. D'Alesandro et al. [119], randomly repeated their proposed procedure 10 times to perform the average result, which is called random cross validation.

3.5.4 Performance Metrics

To measure how is close the prediction to the truth, the results of classifiers are evaluated following some performance metrics. Therefore, once the results attribution are computed, four sets are directly obtained:

- True Positives set contains all the malignant melanoma classified as malignant by

the classifier used, and they are noted by TP.

- False positives set contains all the benign lesions incorrectly identified by the classifier used, and they noted FP.

- True Negatives set contains all the benign lesions classified as benign by the classifier used, and they are noted by TN.

- False negatives set contains all the malignant melanoma incorrectly identified by the classifier used, and they are noted FN.

The objective is to reduce the FP and FN to zeros. The false positives entrains more biopsies for medical doctors and analysts. In the other hand, the false negatives is more dangerous due to the non application of any medical treatment for these false negatives (unhealthy people) cases.

Several databases are used in different articles, therefore, for comparison, it is preferable to compute a percentage of detection or precision. For that, many performance equations are suggested and applied on skin cancer classification [32]. The most used performance metrics in melanoma recognition are detailed below:

- Accuracy (Acc):

$$Acc = \frac{TP + TN}{TP + TN + FP + FN} \times 100\% \tag{3.68}$$

- Sensitivity (Sen):

$$Sen = \frac{TP}{TP + FN} \times 100\% \tag{3.69}$$

- Specificity (Spe):

$$Spe = \frac{TN}{TN + FP} \times 100\% \tag{3.70}$$

- Positive predictive value (PPR):

$$PPR = \frac{TP}{TP + FP} \times 100\% \tag{3.71}$$

- Negative predictive value (NPR):

$$NPR = \frac{TN}{TN + FN} \times 100\% \tag{3.72}$$

- Error probability (Ep):

$$Ep = \frac{FP + FN}{TP + TN + FP + FN} \times 100\% \tag{3.73}$$

- ROC curve : a plot of the true positives TP-rate versus false positives FP-rate.

These metrics are evaluated for classification and recognition step. But, they can be adapted for segmentation results, for example, attributing the variables FP, TP, FN and TN to pixels belonging into regions of interest or background.

3.6 Summary

This chapter introduced a mathematical background of the different methods used in next chapter. It provides as well a deep theoretical understanding of these methods. The chapter is divided into four parts:

1. It started by the Total Variation theory, explaining the Mumford and Shah function and the minimization developed by Chan and Vese. This theory is primordial to explain the extension of Chan and Vese model proposed in the next chapter for skin lesion segmentation.

2. Then, it is followed by the multiresolution analysis theory, where wavelet and curvelet transforms are introduced to be used in the next chapter. It provides also the the multiresolution analysis development starting by Fourier transform into curvelet transform explaining more the main task and limitations of each transform.

3. The third part provides the Local Binary pattern theory. This method is mixed

with multiresolution analysis and used for feature extraction to discriminate melanoma.

4. The fourth (i.e. last part) provides the statistical classification methods to separate the skin cancer into two or more different sets, explaining more the theory of SVM and ANN classifiers. Then, it provides the statistical validation methods referring some methods used in skin cancer area, and finally, it provides the most used performance metrics in skin cancer.

CHAPTER 4

METHODOLOGY

4.1 Overview

In this chapter, the methods developed on skin cancer detection and recognition that can be used in CAD system are presented. Two domains are mainly developed, which are:

1. Segmentation of skin lesion using the adaption of Chan and Vese model for skin cancer images. This adaption can be seen as an extension of the model for other kind of images.

2. Classification of malignant and benign skin lesion using a new method based on border irregularities.

3. Classification of into malignant and benign lesions using a fusion of structural and textural features.

In this chapter, two domains are developed, the first domain is highlighted and discussed in section 4.2. This method is an adapted segmentation for skin cancer images. It is focused to detect the border between the lesion and the background, and the main variation inside the lesion. The second domain is focused on features extraction presented in section 4.3, where two methods are developed. Firstly, border irregularities information is extracted for each lesion to build a descriptor separating the lesions into malignant and benign cases. Secondly, a fusion of structural and textural features using multiresolution analysis (wavelet and curvelet transforms) and local binary pattern is developed.

4.2 Segmentation

In this section, the proposed extension of Chan and Vese model is introduced as follow:

- Firstly, the work developed by Chan and Vese in 2001 [60] is summarized.
- Secondly, the generalization developed by Vese and Chan in 2002 [61],
- Thirdly, the generalization proposed by Li et al. [64] in 2010.
- Finally, the proposed extension and adaption of Chand and Vese model

The basic idea of total variation segmentation and a brief theory of Chan and Vese model was introduced in the last chapter (section 3.2).

4.2.1 Chan and Vese Model

Chan and Vese model is introduced in [60] and its generalization in [61]. The following definition is the one adapted for image segmentation. This method is used to minimize Mumford and Shah equation [62]

Let Ω be open and bounded set and C an evolving curve in Ω. We consider C as a boundary of an open subset ω of Ω (i.e $\omega \subset \Omega$ and $C = \partial\omega$), in what follows, $inside(C)$ denotes ω and $outside(C)$ denotes the region $\Omega\backslash\bar{\omega}$. The segmentation problem presented in [61] is to solve the following minimization problem:

$$\inf_{u,C}\left\{\int_{\Omega}(u-u_0)^2dxdy+\mu\int_{\Omega\backslash C}|\nabla u|^2dxdy+\nu|C|\right\} \tag{4.1}$$

where μ, ν are fixed parameters to weight the different terms in the energy given by equation (4.1), $u_0 : \Omega \to \mathbb{R}$ is a given bounded image-function, u is an optimal approximation of u_0 and $|C|$ is the length of curves making C.

A given $C = \partial\omega$ (the boudary of open set $\omega \in \Omega$) is presented implicitly as the zero Lipscitz continuous function $\phi : \Omega \to \mathbb{R}$ such that $\phi(x, y) < 0$ in ω, $\phi(x, y) > 0$ in

$\Omega \setminus \omega$ and $\phi(x, y) = 0$ on $\partial\omega$. Using the following Heaviside function $H(z)$.

$$H(z) = \begin{cases} 1 & \text{if } z \geq 0 \\ 0 & \text{if } z < 0 \end{cases}$$

The length of C and the area of ω can be expressed respectively by [61]:

$$|C| = \int_{\Omega} |\nabla H(\phi)|, \quad |\omega| = \int_{\Omega} H(\phi) dxdy \tag{4.2}$$

Thus, Chan and Vese model is expressed by the following formula [60]:

$$\begin{aligned} F(c_1, c_2) &= \int_{\Omega} (u_0 - c_1)^2 H(\phi) dxdy \\ &\quad + \int_{\Omega} (u_0 - c_2)^2 (1 - H(\phi)) dxdy \\ &\quad + \int_{\Omega} |\nabla H(\phi)| \end{aligned} \tag{4.3}$$

Where c_1 and c_2 are the averages of u_0 inside the curve C (area of ω) and respectively outside (area of $\Omega \setminus \omega$). These constants (c_1 and c_2) are given by the formula (4.4) and (4.5) after approximation and regularization.

Considering H_ε and δ_ε any C^1 approximation and regularization of H and δ_0 function, as $\varepsilon \to 0$ and with $H'_\varepsilon = \delta_\varepsilon$. The constants c_1 and c_2 are given by the following formula:

$$c_1(\phi) = \frac{\int_{\Omega} u_0(x, y) H_\varepsilon(\phi(t, x, y)) dxdy}{\int_{\Omega} H_\varepsilon(\phi(t, x, y)) dxdy}, \tag{4.4}$$

$$c_2(\phi) = \frac{\int_{\Omega} u_0(x, y) H_\varepsilon(1 - \phi(t, x, y)) dxdy}{\int_{\Omega} H_\varepsilon(1 - \phi(t, x, y)) dxdy}, \tag{4.5}$$

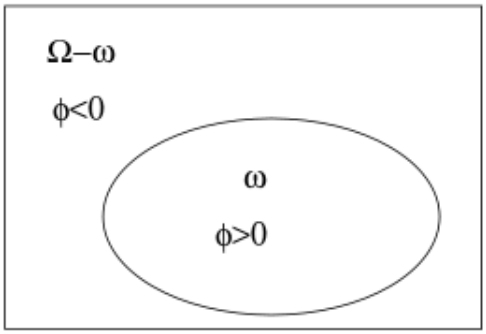

Figure 4.1: *The zero level set function. The boundary C is illustrated by the ellipse which is equivalent to $\phi(x, y) = 0$ and it separates the domain Ω into 2 regions $\phi(x, y) > 0$ and $\phi(x, y) < 0$.*

In figure (Fig.4.1), Ω is represented by the square and the curve C by the ellipse where $\phi(x, y)$ is positive inside and negative outside the elliptic curve.

4.2.2 Generalization of Chan and Vese model

The first generalization of this method was proposed by the same authors [61]. Using a union of zero level set functions ϕ_i, equation (4.3) becomes:

$$\begin{aligned} F_n(c, \Phi) &= \sum_{1 \leq I \leq 2^m} \int_\Omega (u_0 - c_I)^2 \chi_I dxdy \\ &\quad + \sum_{1 \leq i \leq m} \nu \int_\Omega |\nabla H(\phi_i)|. \end{aligned} \tag{4.6}$$

Where $c = (c_1, c_2, ..., c_n)$, $\Phi = (\phi_1, \phi_2, ..., \phi_n)$ and ξ_I is the characteristic function for each class I.

Figures (Fig. 4.2) and (Fig. 4.3) illustrate the cases 2 and 3 zero level sets function respectively. Ellipses and circles represent the curve C and the different classes of ϕ_i.

As noted in [64], the generalization developed by Vese and Chan considers only the cases 2^m, with $m \in \{0, 1, 2, ...\}$. Therefore, for any $m > 2$, at least, one situation N with $N \in]2^{m-1}, 2^m[$ is ignored.

Li et al. [64] proposed in 2010 a new generalization of Chan and Vese model. Their

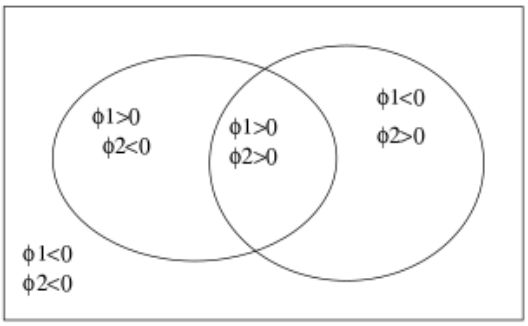

Figure 4.2: *C is represented by the 2 curves $\{\phi_1 = 0\} \cup \{\phi_2 = 0\}$ which gives 4 distinct regions illustrated in this figure, 3 in the foreground and the background.*

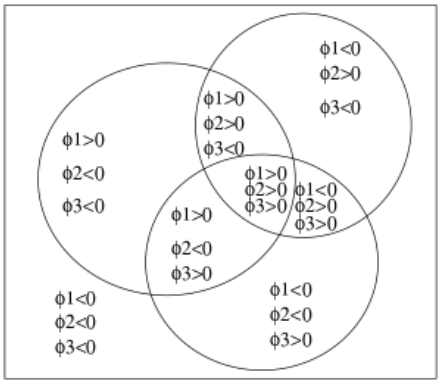

Figure 4.3: *C is represented by the 3 curves $\{\phi_1 = 0\} \cup \{\phi_2 = 0\} \cup \{\phi_3 = 0\}$ dived it to 8 regions with the background.*

main work is to find a global formula for each N between 2^{m-1} and 2^m, with $m \in \{0, 1, 2, ...\}$, using smooth membership function $u_i \in [0, 1]$. Therefore, the energy given in equation (4.1) is reformulated as the following formula:

$$\begin{aligned} F(\{u_i\}_{i=1}^m, \{c_k\}_{k=1}^N) &= \sum_{i=1}^m \int_\Omega |\nabla u_i| dx \\ &+ \lambda \sum_{k=1}^N \int_\Omega |u_0 - c_k| M_k^N dx \end{aligned} \tag{4.7}$$

where for $k_0 = N - 2^{m-1}$, $k_1 = k - k_0$ and $b_i^{m,k-1} = 0 \vee 1$ with $S_k^m = \sum_{i=1}^m b_i^{m,k_1}$, then:

$$\begin{cases} M_k^{2^m} = (-1)^{s_k^m} \Pi_{i=1}^m (u_i - b_i^{m,k-1}) \quad \text{if } N = 2^m \\ M_k^N = (-1)^{s_k^m} \Pi_{i=1}^m (u_i - b_i^{m,k-1}) \quad \text{if } 2^{m-1} < N < 2^m \text{ and } k = 1, \cdots, k_0 \\ M_k^N = (-1)^{s_{k_1}^{m-1}} \Pi_{i=1}^m (u_i - b_i^{m-1,k-1}) \quad \text{if } 2^{m-1} < N < 2^m \text{ and } k = 2k_0 + 1, \cdots, N \end{cases} \tag{4.8}$$

For $N = 3$, the following formula of M_n^k is obtained:

$$M_1^3 = u_1 u_2, \quad M_2^3 = u_1(1 - u_2), \quad M_3^3 = 1 - u_1. \tag{4.9}$$

Equation (4.9) can be written by zero level set function ϕ and the Heaviside function H used in Chan and Vese model:

$$\begin{cases} u_1 u_2 & \propto & H(\phi_1)H(\phi_2) \\ u_1(1 - u_2) & \propto & H(\phi_1)(1 - H(\phi_2)) \\ 1 - u_1 & \propto & 1 - H(\phi_1) \end{cases} \tag{4.10}$$

The existence of soft segmentation developed in equation (4.8) requires to satisfy two constraints. The first one requires that each membership function u_i belongs to the interval $[0, 1]$. Then, the second is the constraint of summation of all the soft membership functions to be one [176] as given by equation (4.11) below:

$$\sum_{k=1}^{N} M_k^N = 1 \tag{4.11}$$

In the formula (4.9), we notice M_3^3 depends only on the membership function u_1. The interrogations of how and why M_3 can be independent of u_2 using zero level set functions are explained in the next section. The development and the illustration of all possible configurations for the detection of 3 regions is also done.

4.2.3 Proposed Extension of Chan and Vese model

Unlike the generalizations of Chan and Vese model developed only for one configuration, in this current work, the objective is to find for each N, with $2^{m-1} \leq N < 2^m$ ($\Rightarrow N \in \mathbb{N}$), all the possible configurations. This objective will help to segment further the details of skin cancer images.

The idea of this work is to complete the segmentation with unfixed number of zero

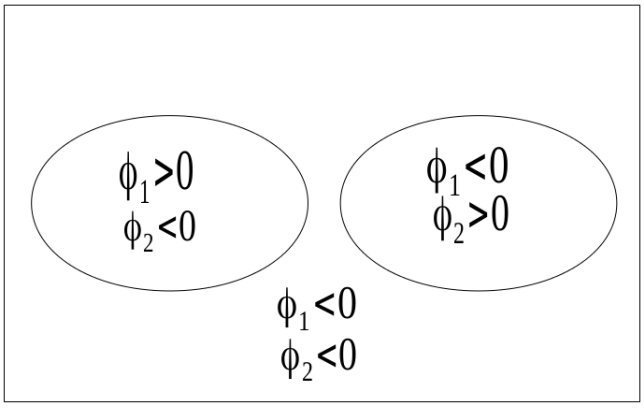

Figure 4.4: *C is represented by the 2 curves without intersection between ϕ_1 and ϕ_2. It illustrates one possible case of $N = 3$.*

level set function ϕ_i. Therefore, for each number of zero set level functions ϕ_i, all possible configurations are studied. Furthermore, the challenge is to choose the best configuration for the segmentation of a given image without fixing the number of ϕ_i beforehand. In this work, the detection of three regions $(N = 3)$ are developed using 2 zero level set functions. An overview for four and five regions is also discussed.

In the general case, the energy of minimization given in equation (4.3) becomes another minimization which takes all the possible combinations for each number of zero level sets:

$$F_N = \inf_{N,j} \left\{ \inf_{c,\Phi} F_{Nj} \right\} \tag{4.12}$$

where j designates the j^{th} combination.

4.2.3.1 Detection of three regions

To detect three regions, exactly two zero level set functions ϕ_1 and ϕ_2 are needed. Thus, to study the case $N = 3$, figures Fig. 4.4 and Fig. 4.5 represent the two possible configurations. the first one considers the null intersection (total separation), and the second one is for the total inclusion. For the inclusion, by symmetry $\phi_1 \subset \phi_2$ is equivalent to $\phi_2 \subset \phi_1$.

The energy represented in Fig. 4.4 and Fig. 4.5 are given respectively by F_{31} and

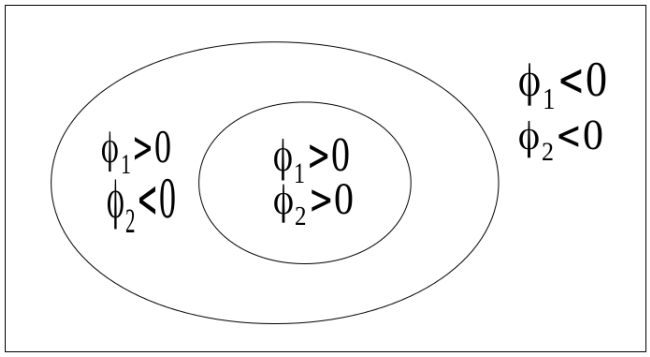

Figure 4.5: *C is represented by the overlapping curves. It is illustrated by $\phi_2 \subset \phi_1$ which is symetric to $\phi_1 \subset \phi_2$.*

F_{32}. Then F_{31} is:

$$\begin{aligned} F_{31}(c,\phi) &= \int_\Omega (u_0 - c_{01})^2 (1 - H(\phi_1)) H(\phi_2) dxdy \\ &+ \int_\Omega (u_0 - c_{10})^2 H(\phi_1)(1 - H(\phi_2)) dxdy \\ &+ \int_\Omega (u_0 - c_{00})^2 (1 - H(\phi_1))(1 - H(\phi_2)) dxdy \\ &+ \nu \int_\Omega |\nabla H(\phi_1)| + \nu \int_\Omega |\nabla H(\phi_2)| \end{aligned} \tag{4.13}$$

and

$$\begin{aligned} F_{32}(c,\phi) &= \int_\Omega (u_0 - c_{11})^2 H(\phi_1) H(\phi_2) dxdy \\ &+ \int_\Omega (u_0 - c_{10})^2 H(\phi_1)(1 - H(\phi_2)) dxdy \\ &+ \int_\Omega (u_0 - c_{00})^2 (1 - H(\phi_1))(1 - H(\phi_2)) dxdy \\ &+ \nu \int_\Omega |\nabla H(\phi_1)| + \nu \int_\Omega |\nabla H(\phi_2)| \end{aligned} \tag{4.14}$$

where $c = (c_{00}, c_{01}, c_{10}, c_{11})$, with:

$$c_{11} = \frac{\int_\Omega u_0 H(\phi_1) H(\phi_2) dxdy}{\int_\Omega H(\phi_1) H(\phi_2) dxdy} \tag{4.15}$$

$$c_{10} = \frac{\int_\Omega u_0 H(\phi_1)(1 - H(\phi_2)) dxdy}{\int_\Omega H(\phi_1)(1 - H(\phi_2)) dxdy} \tag{4.16}$$

$$c_{01} = \frac{\int_\Omega u_0 (1 - H(\phi_1)) H(\phi_2) dxdy}{\int_\Omega (1 - H(\phi_1)) H(\phi_2) dxdy} \tag{4.17}$$

$$c_{00} = \frac{\int_\Omega u_0 (1 - H(\phi_1))(1 - H(\phi_2)) dxdy}{\int_\Omega (1 - H(\phi_1))(1 - H(\phi_2)) dxdy} \tag{4.18}$$

In this special case, equation (4.12) treats only two configurations expressed by equations (4.13) and (4.14) illustrated by figures 4.4 and 4.5. Thus the energy of the image given is expressed by the following formula:

$$F_3 = \inf \ (\inf_{c,\Phi} F_{31}, \inf_{c,\Phi} F_{32}) \tag{4.19}$$

Using equation (4.13) and (4.14), the comparison will be only between the third component of each equation, then equation (4.19) becomes:

$$\begin{aligned} F_3 &= \int_\Omega (u_0 - c_{10})^2 H(\phi_1)(1 - H(\phi_2)) dxdy \\ &+ \int_\Omega (u_0 - c_{00})^2 (1 - H(\phi_1))(1 - H(\phi_2)) dxdy \\ &+ \nu \int_\Omega |\nabla H(\phi_1)| + \nu \int_\Omega |\nabla H(\phi_2)| \\ &+ \inf \Big(\alpha_1, \alpha_2 \Big) \end{aligned} \tag{4.20}$$

where

$$\alpha_1 = \int_\Omega (u_0 - c_{11})^2 H(\phi_1)(H(\phi_2)) dxdy \tag{4.21}$$

$$\alpha_2 = \int_\Omega (u_0 - c_{01})^2 (1 - H(\phi_1)) H(\phi_2) dxdy \tag{4.22}$$

The algorithm will not be more complex in computing, because the comparison is conducted only between the different parts (α_1 and α_2). For example, the background of

the image will be computed once.

In the case where α_2 given in equation (4.22) is minimum then $\phi_2 \subset \phi_1$ as illustrated by figure 4.5. In this case, if $\phi_1 < 0$, it means automatically $\phi_2 < 0$ i.e $(1-H(\phi_1))(1-H(\phi_2))$ is equivalent to $(1-H(\phi_1))$, then equation 4.20 is simplified as follow:

$$\begin{aligned} F_3 &= \int_\Omega (u_0 - c_{10})^2 H(\phi_1)(1-H(\phi_2))dxdy \\ &+ \int_\Omega (u_0 - c_{01})^2 (1-H(\phi_1))H(\phi_2)dxdy \\ &+ \int_\Omega (u_0 - c_{00})^2 (1-H(\phi_1))dxdy \\ &+ \nu \int_\Omega |\nabla H(\phi_1)| + \nu \int_\Omega |\nabla H(\phi_2)| \end{aligned} \tag{4.23}$$

This formulation joints M_3 of equation (4.9) developed by Li et al. [64], where it depends only on ϕ_1.

Using a regularized version of H and the Dirac delta function δ_0 by H_ε and δ_ε respectively. Introducing an artificial time $t > 0$ in the Lipschitz function $\phi(t,x,y)$ with $\phi(0,x,y) = \phi_0(x,y)$ as used by Chan and Vese [60,61]. Keeping c as fixed vector, and minimizing $F31$ and $F32$. The initial contour is giving by the following formulas:

- For $F31$:

$$\begin{aligned} \frac{\partial \phi_1}{\partial t} = \delta_\varepsilon(\phi_1)\Bigg\{ \nu \,\mathrm{div}\Big(\frac{\nabla \phi_1}{|\nabla \phi_1|}\Big) - \Big[-(u_0 - c_{01})^2 H(\phi_2) \\ + \big((u_0 - c_{10})^2 - (u_0 - c_{00})\big)(1 - H(\phi_2))\Big]\Bigg\} \end{aligned} \tag{4.24}$$

$$\begin{aligned} \frac{\partial \phi_2}{\partial t} = \delta_\varepsilon(\phi_2)\Bigg\{ \nu \,\mathrm{div}\Big(\frac{\nabla \phi_2}{|\nabla \phi_2|}\Big) - \Big[-(u_0 - c_{10})^2 H(\phi_1) \\ + \big((u_0 - c_{01})^2 - (u_0 - c_{00})\big)(1 - H(\phi_1))\Big]\Bigg\} \end{aligned} \tag{4.25}$$

- For $F32$:

$$\frac{\partial \phi_1}{\partial t} = \delta_\varepsilon(\phi_1)\Bigg\{\nu \ \text{div}\Big(\frac{\nabla \phi_1}{|\nabla \phi_1|}\Big) - \Big[(u_0 - c_{11})H(\phi_2) \\ ((u_0 - c_{10})^2 - (u_0 - c_{00})^2)(1 - H(\phi_2))\Big]\Bigg\} \tag{4.26}$$

$$\frac{\partial \phi_2}{\partial t} = \delta_\varepsilon(\phi_2)\Bigg\{\nu \ \text{div}\Big(\frac{\nabla \phi_2}{|\nabla \phi_2|}\Big) - \Big[\big((u_0 - c_{11})^2 - (u_0 - c_{10})\big)H(\phi_1) \\ -(u_0 - c_{00})^2)(1 - H(\phi_1))\Big]\Bigg\} \tag{4.27}$$

The soft smooth membership function $u_i \in [0, 1]$ introduced by Li et al. [64] for H^1 regularization is used. Then, in the current studied case, $H(\phi_1)$ and $H(\phi_2)$ are replaced by u_1 and u_2 respectively. These functions are introduced to verify the constraint of summation of all membership functions as required by Shen et al. [176]. Therefore, our system will be presented by the following functions:

- $F31$ will be defined by: $(1 - u_1)u_2$, $u_1(1 - u_2)$ and $(1 - u_1)(1 - u_2)$.
- $F32$ will be defined by: u_1u_2, $u_2(1 - u_1)$ and $(1 - u_1)(1 - u_2)$.

For the energy F_{31} given in equation (4.13) and illustrated in figure 4.4, to put the potential intersection in one of the sets and to respond to the constraint of summation, the following combination: u_1, $u_2(1 - u_1)$ and $(1 - u_1)(1 - u_2)$ is proposed. Therefore, u_1 represents the first choice of the zero level set function, $u_2(1 - u_1)$ represents the second zero set level function excluding u_1 (it pushes to the separability of the two level set functions and reduces the intersection to an empty set), then $(1 - u_1)(1 - u_2)$ represents the image background. This combination is an extension of Chan and Vese model for $N = 3$ not developed by Vese and Chan [61] and neither by Li et al. [64].

For the energy F_{32} given in equation (4.14) illustrated in figure 4.5, knowing that $\phi_1 \subset \phi_2$ the background defined by $(1 - u_1)(1 - u_2)$ can be defined only by $(1 - u_2)$. Therefore, the constraint of summation is satisfied and the current combination will be

presented by: u_1u_1, $u_2(1-u_1)$ and $1-u_2$. It corresponds to the combination developed by Li et al [64]. By symmetry this combination can be expressed by: u_1u_2, $u_1(1-u_2)$ and $1-u_1$.

Then, all the possible configurations by the following system are encompassed as follow:

$$\begin{cases} u_1, \;\; u_2(1-u_1), \;\; (1-u_1)(1-u_2) \\ u_1u_2, \;\; u_2(1-u_1), \;\; 1-u_1 \end{cases} \tag{4.28}$$

The system given in equation (4.28) is applied on skin images database. The obtained results and the implementation are illustrated in figures 4.12 and 4.13a in the next sub-section (4.2.3.5).

4.2.3.2 Extension to detect four regions

This extension developed can be adapted for the detection of more than 3 regions. Thus, to detect four regions, Li et al. [64] explored the one developed by Vese and Chan [61] using only two sets with intersection as illustrated in figure 4.2.

To detect four regions, a minimum of two sets and a maximum of three sets is needed. The possible configurations are illustrated below with the corresponding equation systems using soft membership function u_i where numerically $u_i = H(\phi_i)$. The proposed systems satisfy the constraint of summation of all membership function to be one given in equation (4.11). At all, 5 configurations are obtained, one configuration using two sets and four configurations using three sets as detailed below:

1. Using two sets ϕ_1 and ϕ_2, there is only one possible configuration to get 4 different regions. It is the alone case developed for total variation segmentation.

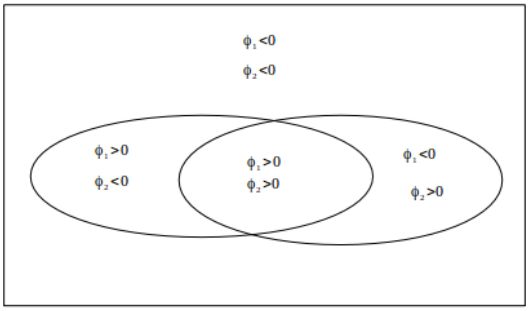

$$\begin{cases} u_1 u_2 \\ u_1(1-u_2) \\ u_2(1-u_1) \\ (1-u_1)(1-u_2) \end{cases}$$

Figure 4.6: *Four regions using two level set functions ϕ_1 and ϕ_2.*

2. Using three sets, the first configuration is presented by total separability between sets. It is equivalent to the first case developed in the current study for the detection of 3 regions illustrated by figure 4.4.

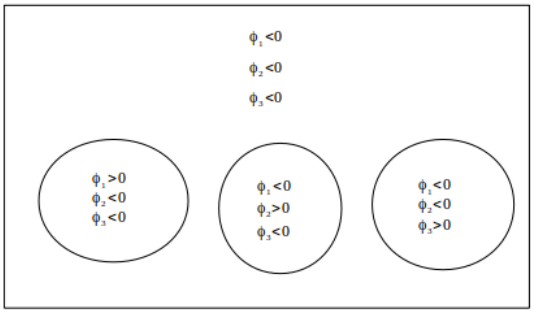

$$\begin{cases} u_3 \\ u_2(1-u_3) \\ u_1(1-u_2)(1-u_3) \\ (1-u_1)(1-u_2)(1-u_3) \end{cases}$$

Figure 4.7: *Four regions using three level set functions ϕ_1, ϕ_2 and ϕ_3 using the total separation method*

3. The second configuration using three sets to detect four regions is characterized by the mixture between inclusion and separability as illustrated below. It illustrates separability between ϕ_2 and ϕ_3 and inclusion of ϕ_1 in ϕ_2.

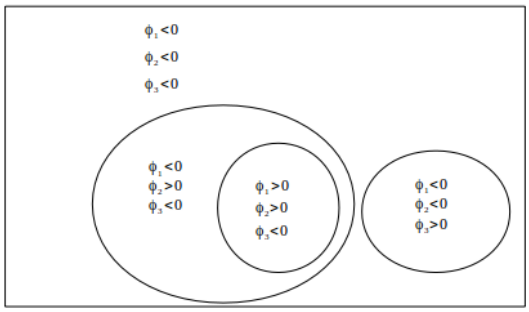

$$\begin{cases} u_3 \\ u_1 u_2(1-u_3) \\ u_2(1-u_1)(1-u_3) \\ (1-u_2)(1-u_3) \end{cases}$$

Figure 4.8: *Four regions using two level set functions ϕ_1, ϕ_2 and ϕ_3 using separation-inclusion*

4. The third configuration using three sets to detect four regions is characterized by the mixture between inclusion of the two sets and their separability as illustrated below. It illustrates separability between ϕ_1 and ϕ_2 and inclusion of ϕ_1 and ϕ_2 in ϕ_3.

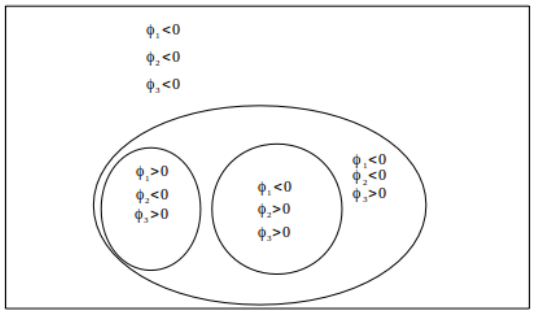

$$\begin{cases} u_1 u_3 \\ u_2 u_3 (1 - u_1) \\ u_3 (1 - u_1)(1 - u_2) \\ (1 - u_3) \end{cases}$$

Figure 4.9: *Four regions using two level set functions ϕ_1, ϕ_2 and ϕ_3 using inclusion-separation.*

5. The last configuration using three sets is presented only by the inclusion of sets as illustrated below. This configuration is equivalent to case developed to detect 3 regions illustrated in figure 4.5.

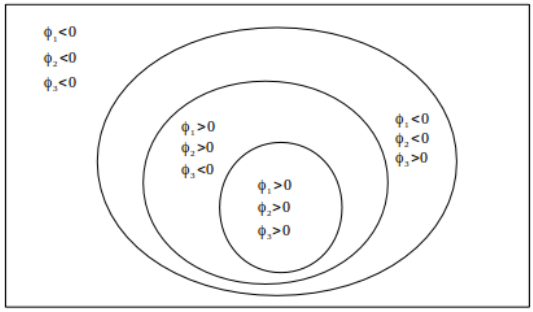

$$\begin{cases} u_1 u_2 u_3 \\ u_2 (1 - u_1) \\ u_3 (1 - u_1)(1 - u_2) \\ (1 - u_2)(1 - u_3) \end{cases}$$

Figure 4.10: *Four regions using two level set functions ϕ_1, ϕ_2 and ϕ_3 using total inclusion.*

4.2.3.3 Extension for five regions

To detect 5 regions, 12 configurations are possible. Thus, the minimum of sets (ϕ_i) required is three and the maximum is four. Therefore, 4 possible configurations in case of three sets (ϕ_i) and 8 possible configurations in the case of four sets (ϕ_i) are obtained.

4.2.3.4 *comparison with Generalization of Chan and vese model*

Figure 4.11 illustrates the generalization of the proposed method compared to the ones developed in the literature. We can see that, in the proposed method, all possible situation are studied to segment efficiently the lesions.

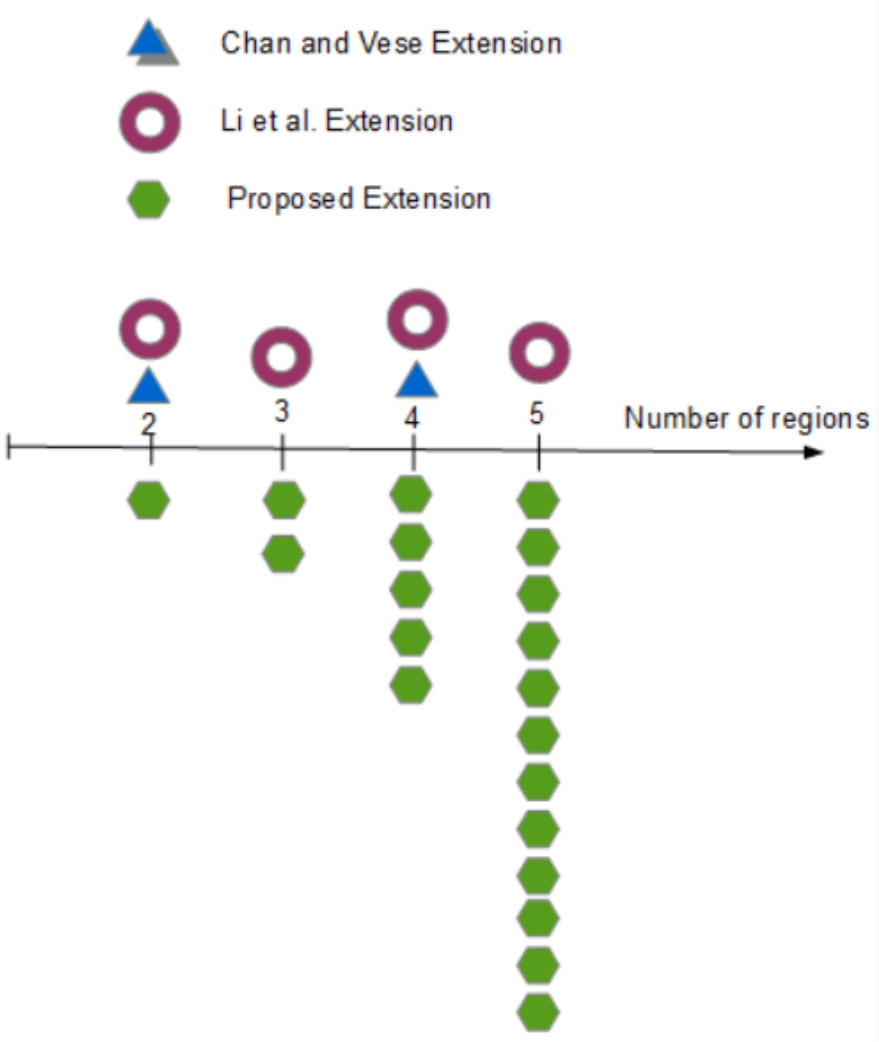

Figure 4.11: *Comparison with existing generalization of Chan and Vese model*

4.2.3.5 *Implementation and illustration*

The implementation of the proposed method is applied on skin cancer images. The illustration of some cases to present the method and its visual effect are shown.

(a) (b) (c)

Figure 4.12: Implementation of the approach using equation (4.13). (a): Original RGB image. (b): Segmentation of the two regions under separability model (equation (4.13)). (c): Global region-based segmentation.

(a) (b) (c)

Figure 4.13: Implementation of the approach using equation (4.14). (a): Original RGB image. (b): Segmentation of the two regions under inclusion model (equation (4.14)). (c): Global region-based segmentation.

Figures 4.12 and 4.13 illustrate the typical results segmentation of the developed approach applying the two versions of $N = 3$ described by equations (4.13) and (4.14)

respectively. It can be seen easily from figures 4.12b and 4.13b the separability and the inclusion of the sets ϕ_1 and ϕ_2 respectively. We notice that the minimization model given in equation (4.19) is not implemented in the current work due to the manual parameterization of Chan and Vese model (ν and dt).

The image used in these figures (4.12 and 4.13) is taken from DermIs (`http://www.dermis.net`) under the name SSM34.

In the next chapter (5), the application of this method is analyzed and discussed. More examples are given and compared to the previous approaches on standard camera skin cancer images. The result of the segmentation are also evaluated by three experts.

4.3 Feature Extraction

4.3.1 Overview

The random development of skin lesions, specially melanoma cases, complicate the classification and the recognition of malignant skin lesions. Therefore, there is a need to develop a discriminant set of features to well classify using CAD system.

In the current section, two distinct methods are developed to recognize benign and malignant lesions. For dermoscopic images, the fusion of structural and textural features is explored, as explained in subsection 4.3.2, and for standard camera images, the border irregularity features is presented in section 4.3.3.

4.3.2 Structural and textural features

The multitude of skin cancer lesions, benign and malignant, complicates the recognition of skin cancer. In addition to that, melanoma is developing randomly in different directions. However, finding the best descriptor to discriminate melanoma is one of the hardest task in medical image processing. In the current study, a set of discriminating features obtained from different descriptors to distinguish benign and malignant cases

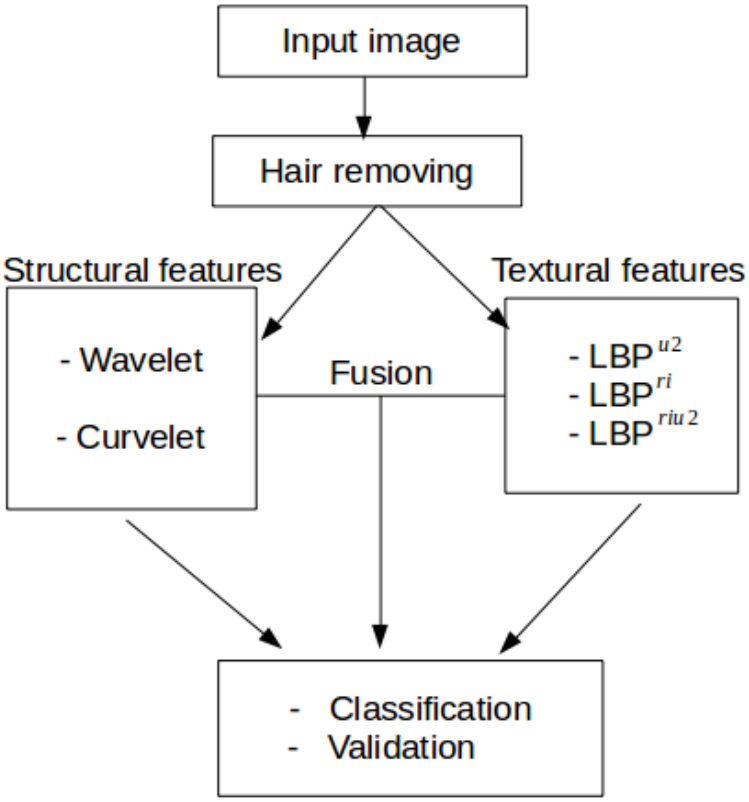

Figure 4.14: Flowchart of structural and textural features fusion proposed in this work.

is presented. Then, two kinds of features are selected and used in dermoscopic images for melanoma recognition as illustrated by the diagram in Fig.4.14.

The fusion of two descriptors introduced in the last chapter (see section 3.3) are explored. Therefore, a set of structural features from multi-resolution analysis methods (wavelet and curvelet coefficients) are used. Further, local binary pattern (LBP) operator is used to extract the textural features. The method is also presented in section 3.4. The details and the implementation of the proposed approach are explained below.

1. First, the structural features are extracted using wavelet and curvelet coefficients. Two level decompositions of Discrete Wavelet Transform (DWT) and Fast Digital Curvelet Transform (FDCT) via warping (see section 3.3) are applied on the melanoma region of interest (ROIs). For each coefficient matrix seven statistical features were computed namely: $Energy$, $Entropy$, $Mean$, $Standard\,deviation$, $Maximum$, $Moment$ and $Homogeneity$.

2. Second, a set of textural features using different variants of local binary pattern (LBP) i.e. rotationally invariant, uniform and non-uniform rotationally invariant distinct textures features are extracted.

3. Then, a feature fusion is performed using the concatenation of structural and textural features of each image.

4. Lastly, SVM classifier is used for classification and diagnosis. Then, $1000-$random sampling cross validation is explored to validate the obtained results.

4.3.2.1 Structural features

The structural features are extracted as follow:

- For wavelet, we used Daubechies 4 waveform, then 8 coefficient matrices are computed, 4 from the first level and 4 from the second level (one approximation coefficient matrix and three details coefficient matrices) using equations (3.34) to (3.37). In total, we extracted 64 features from wavelet transforms.

- For two level of curvelet decomposition 9 curvelet coefficient matrices were obtained for each image i.e. 1 matrix from the first level and 8 matrices from the second level. These matrices are built using equation (3.45) detailed in the next section. Thus for each level, seven statistical features were computed. Thus a total of 63 features from curvelet two level decompostion were obtained.

4.3.2.2 Textural features

For textural features, Local Binary Pattern (LBP) operator is used to extract local textural variations. Thus, depending on the variant of LBP operator as detailed in section 3.4, three LBP variants are explored in the current work. Therefore, we have:

- 59 textural features from LBP^{u2} (Uniform pattern).

- 36 from LBP^{ri} (invariant rotation).

- 9 from LBP^{riu2} (Invariant rotation uniform pattern).

Indeed, only radius $R = 1$ and eight neighborhood pixels ($P = 8$) are used in the experiments. Here it is worth mentioning that all the features were normalized to the range $[0 - 1]$ and their influence before and after fusion can be recorded in validation performances.

4.3.2.3 Implementation

The proposed approach is implemented on the public database PH^2 presented by Mendocca et al. [149]. A descriptive and statistical analysis of the database is also achieved and presented in next chapter. The result of this analysis is compared to the known ABCD rule used in the hospitals.

Many implementations are computed separately and/or by combination between structural and textural features selected. The obtained results of the three variants of LBP methods (invariant rotation LBP, uniform Pattern LBP and invariant rotation uniform pattern LBP), wavelet and curvelet coefficients, and the different combination are validated using random sampling cross validation under SVM classifier with linear kernel. Then, a comparison with the exiting results in the literature using the same database is also achieved. The results are presented and discussed in chapter 5.

4.3.3 Border Irregularity Features

The geometrical characteristics of borders are explored by the approach developed in this section. Therefore, the proposed work is divided mainly into two main stages. First, the standardization of image direction which is a kind of normalization of the database to have the same view for all images. Second, the border feature are extracted using two new concepts, valleys and crevasses, to explore the irregularities for diagnosis.

4.3.3.1 Standard image orientation

Different illumination conditions, skin tones, hairs on the skin and varying the angle of image acquisition, add noise to this images. These artifacts make the feature extraction more challenging. Thus, a preprocessing is required to remove these additional noises. Once the noise is removed, there is a need to present all the images in one standard view. Hence, in the current study, a conversion of the images into one common view is presented. Thus, the approach to normalize the images is presented.

The proposed method is applied when the region of interest (ROIs) are detected and boxed using bounding box and coordinates of ROIs from the binary images of ground truth given in the database. The dimensions of the bounding box depend on the size of the abnormal region itself. The ROI used are extracted manually, and taken as ground truth to show the contribution of the current approach.

To resolve this issue and standardize the size, the following strategy is adopted:

- Firstly, the minimization of the unwanted area using rotation of the ROIs from 0 to 180 degrees. Then, the box of ROI containing small area is selected.

- Secondly, horizontal (or vertical) orientation of boxes is chosen for standard view. Figure 4.15 illustrates the reorientation and the choice of direction on our database. It can be seen that ROI box is minimized to contain only the lesion. The image provides from DermIs website (`www.dermis.net`) under the name of SSM26a.

The algorithm 1 summarizes the different steps of the standard image orientation method.

Algorithm 1 Standard Image Orientation Algorithm

img: Image input
for $\alpha = 1$ to 180 **do**
    new_img = rotate(img, α)
    box_img = detection of the box containing the ROI.
    [a(α), b(α)] = size(box_img)
end for
[M, ind] = min(a)
std_img = rotate(img, ind)
std_box = detection of the box containing the ROI

(a) (b) (c) (d)

Figure 4.15: Illustration of the normalization of the images using standard view orientation approach. (a): Original RGB image. (b): The ROI of the lesion. (c): The isolation of the ROI. (d): Reorientation of the ROI to horizontal view. The image is provided from DermIs website (`www.dermis.net`) under the name of SSM26a.

4.3.3.2 Border feature extraction

The border irregularities are one of the widely visible features to explore for discrimination. However, the benign lesion borders are not so smooth to fit them with a mathematical function. Malignant and benign lesions can be developed in different ways as indexed by Lee et al. [108]. The construction of these features is started by the idea of evaluation of border irregularities exploring different features which are more local. It is based on algorithm detecting each two consecutive null derivation of the border curve. However, it is very difficult to formulate the analytic function of each lesion border. Then, an new algorithm is implemented to express this need. Two new concepts, valleys and crevasses, are extracted as first and second level of border irregularity.

To detect these new concepts, a newer and simpler algorithm exploring the border irregularities in four directions is proposed. The horizontal direction explores all pixels from right to left and vice versa, and vertical direction explores the pixels from up to down and vice versa. Figure 4.16 illustrates the four directions applied in the proposed

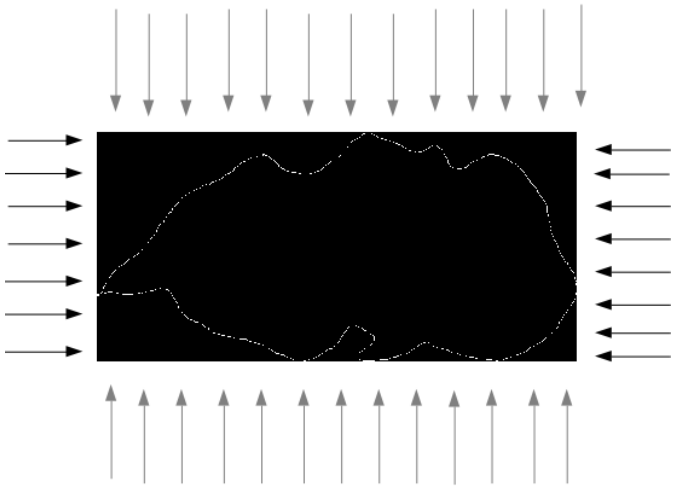

Figure 4.16: Four direction to detect the regular border. Horizontal direction: left to right and right to left. Vertical direction: up to down and down to up.

approach. This algorithm is applied on the standard oriented images explained in the last sub-section (4.3.3.1).

The four directions shown in Figure 4.16 are divided into two groups, horizontal and vertical. Thus, for each line and column of pixels, the area between the box limit and the first contact of the arrow with the ROI's edge are isolated and removed. Thus, only the missed areas are kept. Therefore, if the border is more regular, all the outside part of the pigment will be detected and removed. In the other case, more the border is irregular, more it misses many parts of the outside part of the pigment.

Two kinds of missed parts are noted. Firstly, valley part is the missed one using only one direction (horizontal or vertical) separately. Secondly, the crevasse part is the missed one using both directions in the same time, the crevasse have almost the cul-de-sac geometrical form. Figure 4.17 illustrates the valley and the crevasse cases. They can be considered as the first and the second level of the border irregularities.

These border irregularities quantified by the valleys and crevasses are used as features exploring the size and number of the concepts detected. Thus, let v denotes valleys and c crevasses, two counting functions are defined, N to compute the number of areas

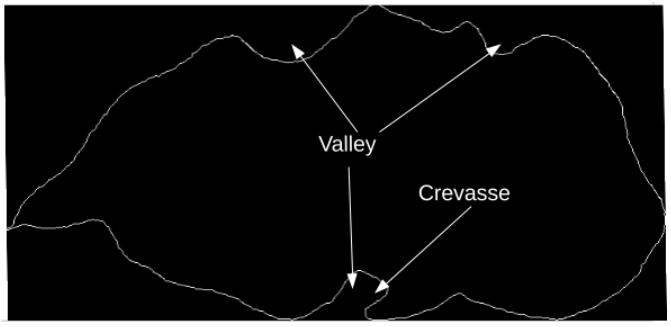

Figure 4.17: Illustration of the valley and the crevasse cases: Valley: using only one direction (horizontal or vertical) and Crevasse: Using two directions (horizontal and vertical)

detected and S to compute the size of each area detected. Therefore, 8 features are extracted and divided in 2 groups, globals and locals. The global ones are the features not depending on some thresholds and the local ones are those depending on these thresholds. The choice of these global and local features is done gradually to increase the performance of classification between the malignant and benign lesions.

The first group contains 4 global features concerning the total number of valleys and crevasses detected and their total size as detailed below.

- $N(v)$ is the number of valleys and $N(c)$ is the number of crevasses.
- $S(v)$ is the size of all valleys and $S(c)$ is the size of all crevasses.

The second group contains 3 other features computing the number and the size of detected valleys and crevasses greater or smaller than two thresholds τ_v and τ_c respectively. These features are added in order to increase the performance of detection and decreasing the noises of border segmentation i.e a crevasse detected with a size of one or two pixels will be less important than a crevasse of fifty pixels of size, for example. Then, the following equations are formulating these three local features.

- $N(\mathbf{1}_{S(v)\geq\tau_v})$ and $N(\mathbf{1}_{S(v)<\tau_v})$ quantify the number of valleys greater/smaller than the threshold τ_v.
- $N(\mathbf{1}_{S(c)\geq\tau_c})$ quantify the number of crevasses greater than the threshold τ_c

where,

$$\mathbf{1}_{\mathbf{S(x)}\geq\tau} = \begin{cases} 1 & S(x) \geq \tau \\ 0 & otherwise \end{cases} \quad \text{, with} \quad \begin{cases} x \in \{v, c\} \\ \tau \in \{\tau_v, \tau_c\} \end{cases} \tag{4.29}$$

Finally, the eighth features is the ratio of pigment pixels over the box area, this feature is introduced to moderate the differences of image dimensions in the database which are standard camera dataset with different size. It contains also information due the global border irregularity i.e after standardization step, the area of the background of the image is minimized, then the ratio is behaving like the relation of p-norms, where the border defines the 2-norm and the box the $\inf -norm$ as illustrated in figure 4.18. This value is defined by Γ-value given by the following equation:

$$\Gamma = \frac{Area(r)}{Area(b)} \tag{4.30}$$

where r denotes the Region of Interest (ROI) and b the selected box containing the ROI.

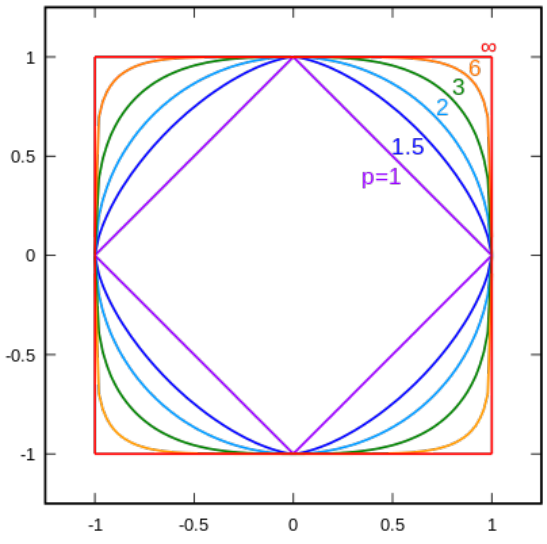

Figure 4.18: p-norms illustration

Therefore, combining all the characteristics defined above, for each image a set of

8 features are extracted, as summarized by the variable $feat$ given by equation (4.31):

$$\begin{aligned} feat \;\; = \;\; & \Big\{ N(v), N(c), N(s(v)), N(s(c)), N(\mathbf{1}_{s(v)\geq\tau_v}), \\ & N(\mathbf{1}_{s(v)<\tau_v}),\; N(\mathbf{1}_{s(c)\geq\tau_c}), \Gamma \Big\} \end{aligned} \tag{4.31}$$

where $\tau_v, \tau_c \in \mathbf{N}$ chosen empirically. In the implementation of the algorithm, τ_c is fixed to 2 and $\tau_v \in [0, 100]$.

The two steps of the current approach is implemented on skin database provided from standard camera. The results are presented and discussed in the next chapter.

4.4 Summary

This chapter provides the three methods developed in the current work.

- Firstly, the extension of Chan and Vese model is explored, which is a generalization of the model and an adaption for skin cancer images characteristics. It was adapted to segment the small details inside the lesions, such as colors and pigment areas and structures.

- Secondly, a fusion by concatenation of structural and textural features are explored and developed to discriminate benign and malignant pigment skin lesions. The structural features are obtained exploring a wavelet and curvelet transforms, while the textural features are obtained exploring local binary pattern operator.

- Thirdly, a method based on border irregularities is developed, introducing two new concepts in skin images which are valleys and crevasses as first and second level of border irregularities. A normalization of skin cancer view is also proposed in the method as preprocessing step.

The proposed methods are applied on skin cancer databases. The results are presented in the next chapter.

CHAPTER 5

RESULTS AND DISCUSSION

5.1 Overview

The obtained results from the three proposed methods of the current work are presented and discussed in this chapter. Firstly, it started by the introduction of the different databases used which are dermoscopic images and standard camera images. Secondly, it is followed by the obtained results from the three methods developed which are, segmentation of the region of interest using the extension of Chan and Vese model, the fusion of textural and structural features and border irregularity features. Finally, the comparison of the obtained results with the existing methods is performed.

5.2 Datasets

Two different acquisition of database, dermoscopic and standard camera images, are used in the current work divided following their acquisition mode into dermoscopic and standard camera images. The two sets contains 406 images, 200 are dermoscopic and 206 are from standard camera. The two databases, dermoscopic and standard camera images, are presented in subsections 5.2.1 and 5.2.3, respectively.

5.2.1 Dermoscopic Images Database

PH^2 Database was introduced in 2013 by Mendoca et all. [149] and more detailed in 2015 by the same authors [177]. PH^2 is a public and free database, built to perform and

compare the evaluation of several systems. The database was built up through the joint collaboration between Universidade do Porto, Técnico Lisboa, and the Dermatology service of Hospital Pedro Hispano in Matosinhos, Portugal. The acquisition of images was obtained under the same conditions. They are 8-bit RGB color images with a resolution of 768×560 pixels.

The database contains a total of 200 dermoscopic images divided into 160 benign lesions and 40 melanomas. The benign lesions contain 80 common nevi and 80 atypical nevi. The quality, resolution and dermoscopic features of images are highlighted in the current database. Every image was segmented manually and diagnosed by several dermatologists. It contains also the clinical diagnosis and dermoscopic criteria such as asymmetry, color and presence of typical and atypical structures.

Table 5.1 summarizes all the given characteristics in PH^2 database, where sub-feature is describing the different cases of each feature, for example, fully asymmetry is a sub-feature of Asymmetry. The table shows the percentage of the presence / absence of each sub-feature. For each percentage, the number of images is noted between brackets. The table is to be read by columns, thus for example, the common nevus is 96.25% fully symmetric, 2.5% is symmetric in one axis and only 1.25% is fully asymmetric and melanoma is 12.5% fully symmetric, 5% symmetric in one axis and 82.5% fully asymmetric. The table shows the dominant characteristics for each feature. It represents the cross table between characteristics and skin lesions diagnosis.

Based on the given features in table 5.1, intuitively, the most difficult is to recognize the atypical nevus. Thus, for example the asymmetry feature makes a real border between common nevus and melanoma only. The pigment network feature separates more common nevus with a total absent of pigment network to atypical and melanoma. However the dots/globules features are not descriptive between the three cases. We can observe also that streaks and regression area features are more common in common nevus and atypical nevus than melanoma. Blue-whitish veil discriminates better between benign and malignant compared to other features. Finally, the color increases gradually from common nevus to melanoma.

Table 5.1: Summary of the characteristics of PH^2 database representing the percentage of each sub-feature and between brackets the number of images.

Database characteristics		**Common Nevus** (80)	**Atypical Nevus** (80)	**Melanoma** (40)
Asymmetry	Fully symmetric	96.25% (77)	43.75% (35)	12.5% (5)
	Symmetric in 1 Axe	2.5% (2)	33.75% (27)	5% (2)
	Fully Asymmetric	1.25% (1)	22.5% (18)	82.5% (33)
Pigment network	Typical	100% (80)	3.75% (3)	2.5% (1)
	Atypical	0% (0)	96.25% (77)	97.5% (39)
Dots / Globules	Absent	36.25% (29)	50% (40)	45% (18)
	Typical	57.5% (46)	10% (8)	0% (0)
	Atypical	6.25% (5)	40% (32)	55% (22)
Streaks	Absent	98.75% (79)	80% (64)	67.5% (27)
	Present	1.25% (1)	20% (16)	32.5% (13)
Regression area	Absent	100% (80)	95% (76)	47.5% (19)
	Present	0% (0)	5% (4)	52.5% (21)
Blue-whitish veil	Absent	100% (80)	92.5% (74)	25% (10)
	Present	0% (0)	7.5% (6)	75% (30)
Color	1 color	42.5% (34)	25% (20)	0% (0)
	2 colors	53.75% (43)	63.75% (51)	32.5% (13)
	3 colors	3.75% (3)	11.25% (9)	27.5% (11)
	4 colors	0% (0)	0% (0)	32.5% (13)
	5 colors	0% (0)	0% (0)	7.5% (3)
	6 colors	0% (0)	0% (0)	0% (0)

Another way of reading table 5.1 is horizontally. Indeed, it shows the influence of each sub-feature. For example, the typical Dot/Globules feature is more frequently in common nevus than atypical nevus and almost inexistent in melanoma case. However, the atypical Dot/Globules feature shows an opposite behavior with a high presence in melanoma, less in atypical nevus and rarely present in common nevus. A statistical analysis of the database is performed and compared to a based scoring system used in the hospitals in the next sub-section.

From the table 5.1, it can be seen that:

- Asymmetry makes a border between common nevus and melanomas with 96.25% fully symmetric for common nevus and 82.5% fully asymmetric for melanoma. However, for atypical nevus, the asymmetry feature is not significant as shown in the table with 43.75%, 33.75% and 22.5 for asymmetry, symmetric in 1 axis and

fully asymmetric, respectively.

- The pigment network feature makes a border common nevus in one side with 100% typical network and in the other side atypical and melanoma with 96.25% and 97.5% respectively for atypical pigment network feature.

- Dots / Globules feature is more typical for common nevus than atypical nevus and melanoma with 57.5%, 10% and 0%, respectively. Then, the opposite behavior is visible for atypical, where it is rare in commons nevus with 6.25% and more present in atypical nevus and melanoma with 40% and 55%, respectively.

- Streaks feature is more discriminating between common nevus in one side and atypical nevus and melanoma in other side when it is present. However, when it is absent, it is very difficult to conclude regarding the percentage of absence of streaks of common, atypical and melanoma, which are 98.75%, 80% and 67.5%, respectively.

- Regression area is describing the common nevus by the total absence, and more it is present, more there is a high probability to get melanoma.

- Blue-whitish veil has the same behavior than regression area, where is more absent for common and atypical nevus and more present for melanoma.

- Color feature is discriminating melanoma if three or more colors are detected with a percentage of 67.5%, and discriminating common and atypical nevus if two colors or less are detected with a percentage of 96.25% and 88.75%, respectively.

5.2.2 Significance of the database

The significance and the representativeness of the database in medical images is one the most challenging task. The information given by the current database contain almost ABCD rule developed by Stolz et al. [14] and used for comparison by Capdehourat et al. [1] and Dolianitis et al. [35].

The PH^2 database quantifies each pigment following ABCD rule excepting border irregularities. According to Capdehourat et al. [1], the evaluation of ABCD rule follows the scores summarized in the table 1.1 where dermoscopic structures contains pigment network, structures ares, dots, globules and branched streaks. The authors added to these features Blue-whitish veil which is a major criteria of 7-point checklist [1] system. This scoring system is applied on the features described in table 5.1. It followed the method used by Capdehourat et al. [1] where :

- Asymmetry is evaluated from 0 to 2 , with 0 being fully symmetric, 1 for symmetric in one axis and 2 for fully asymmetric. It has the highest weight factor of 1.3.

- Border is evaluated with score from 0 to 8, drawing eight segments; one point is given for each abrupt pigment cutoff with a weight factor of 0.1.

- Color is evaluated from 1 to 6, attributing one point for each color with a weight factor of 0.5. Colors considered are white, red, black, light brown, dark brown and blue-gray.

- Dermoscopic structures encompass five structures which are: pigment network, structureless area, dots, globules and branched streaks. One point per structure with a weight factor of 0.5.

We notice that there are some differences between extracted features in PH^2 database and ABCD rule. Therefore, the threshold of the scoring system is adapted by removing the contribution of border irregularities. Then, the thresholds 4.75 and 5.45 became 4.50 and 5.20, respectively. Therefore, for each image the obtained score value (S_{abcd}) of the function given in equation (1.1) is evaluated as follow:

- benign: if the score is $S_{abcd} < 4.50$,

- clinical doubt: lesion if the score lies between $4.50 \leq S_{abcd} \leq 5.20$,

- malignant: if the score is $S_{abcd} > 5.20$.

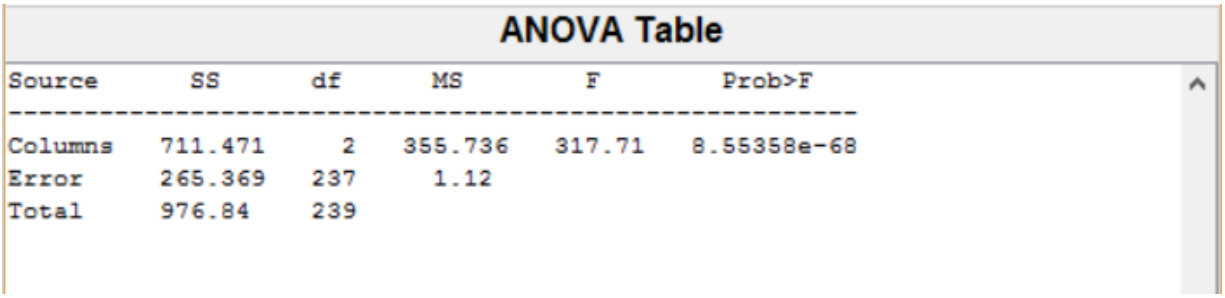

ANOVA Table

Source	SS	df	MS	F	Prob>F
Columns	711.471	2	355.736	317.71	8.55358e-68
Error	265.369	237	1.12		
Total	976.84	239			

Figure 5.1: ANOVA test results

There are other characteristic explored in the database, such as blue-whitish veil, not used in ABCD rule, but used in another scoring system which is 7-point checklist [1]. However, the objective evaluation is difficult to be achieved due the visual features characterized depending only on the decision of absence or presence of each characteristic.

The results reported by Dolianitis et al. [35] are presented in the table 5.2. They are compared to the results obtained from PH^2 database applying ABCD rule. These results show a similar behavior and equivalent results for the three performance metrics which are sensitivity, specificity and accuracy. The threshold of ABCD rule, given in the table **??**, applied on PH^2 database was adapted taking in consideration the missing values of border irregularities. Then, the value of the threshold is reduced to 4.5 and 5.20 in place of 4.75 and 5.45 respectively.

Table 5.2: Result of ABCD rule obtained from PH^2 database

Diagnositic Parameter	Doliantilis et al. [35]	PH^2 Database
Sensitivity	77.5%	77.5%
Specificity	80.4%	97.5%
Accuracy	73.2%	87.5%

Applying Analysis of Variance (ANOVA) on the vector obtained by ABCD rule on the H_0 (same population) against H_1 (different classes). The P-value obtained is less than 0.01 as given in the Matlab table reported in figure 5.1. Then, the hypothesis H_0 is significantly rejected. Thus, the database presents significantly heterogeneous population (more than two classes).

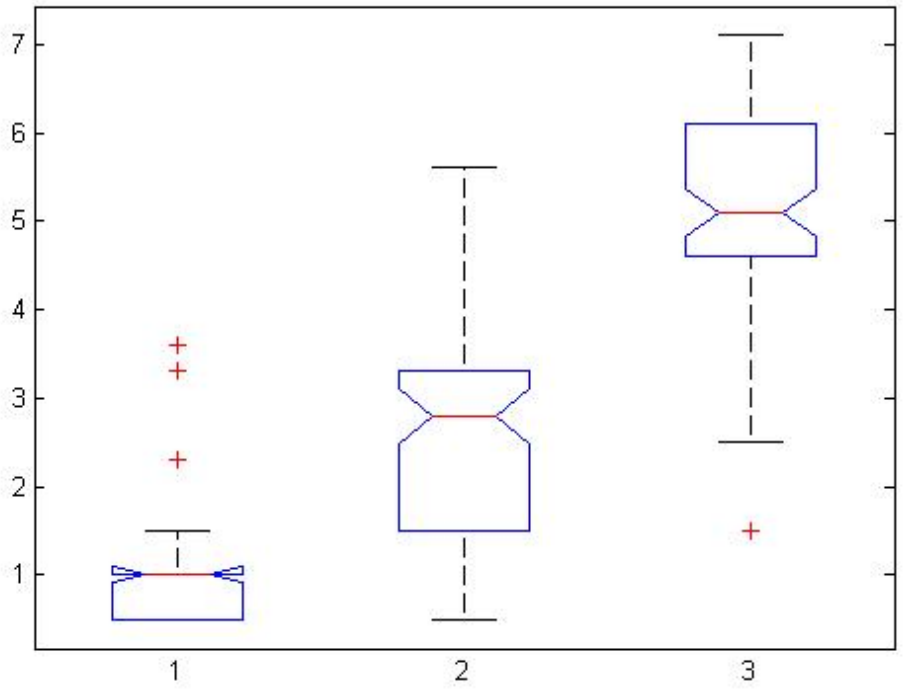

Figure 5.2: Variability of the three classes of the PH^2 database. (1): Common nevus. (2): Atypical nevus. (3): Melanoma.

The box plot in Figure 5.2 illustrates graphically the variability of each group and deduce three different classes in the population.

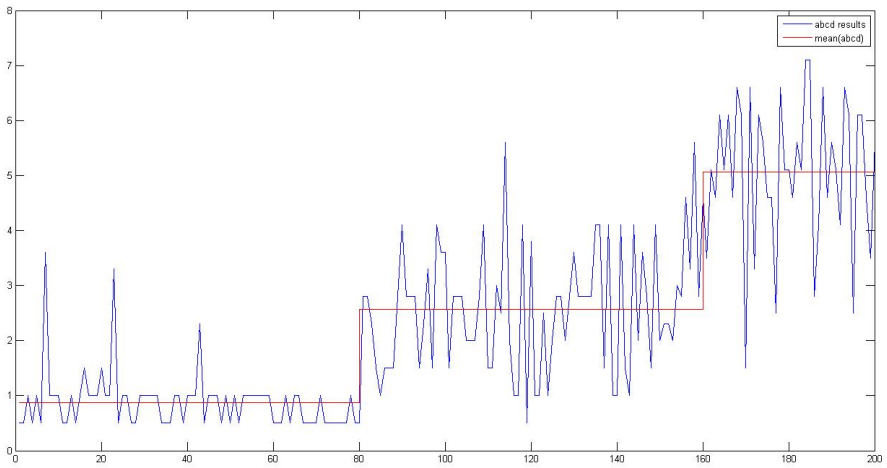

Figure 5.3: Results of ABCD rule system applied on PH^2 database.

Figure 5.3 describes the results of ABCD rule (blue) of the whole database and the mean of each class (red). Descriptively, using ABCD rule results, the graph shows more stability in common nevus lesion than the two other cases (atypical nevus and melanoma).

5.2.3 Standard Camera Images Database

The standard camera image database is provided from two dermatology website, Dermatology Information System (DermIS) [4] and Dermquest [5]. The database contains a total of 206 images where 118 are melanomas cases and 87 are benign lesions. DermIS contains 69 images divided into 43 melanomas and 26 benign lesions and DermQuest contains 137 images divided also into 76 melanomas and 61 benign lesions. Recently (2014) Amelard et al. [105] used this database in his work.

The DermQuest database shows a redundancy of some images due the different acquisition of the same image changing the distance and the view of acquisition. To avoid a confusion and make independence between lesions, only clear images are chosen. Therefore, 40 images are deleted where 38 are melanomas and 2 are benign lesions. Figure 5.4 illustrates one case of redundant images. In this cases the image in figure 5.4a is kept and the other in figure 5.4b is deleted in the database. Thus, the new database contains 166 images divided into 99 melanomas and 67 benign lesions.

(a)

(b)

Figure 5.4: Illustration of the same image acquired with different distance. (a): LMM8_orig image (kept). (b): LMM8_2_orig image (removed) [4].

5.3 Segmentation of Images Results

The obtained results of the extension of Chan and Vese Model proposed in section 4.2 are presented in this section. The implementation of the developed method on different images is presented in the next subsection (5.3.1), then an evaluation of the segmentation is presented in subsection 5.3.2.

The algorithm is implemented in the whole database of malignant and benign lesions presented in section 5.2.3. The following figures illustrate different image segmentations showing visually more and less accurate cases. As mentioned in the literature, the most difficult of the original method is to provide the best parameters of the model to get attended segmentation. Therefore, for each presented image, the two parameters ν and dt are given. An exhaustive table for the whole database is given in the end of the section. The minimization given in equation (4.12) is not implemented in the current work. The reasons are discussed and some methods are suggested in perspectives and future directions.

To remove different noises, the segmentation is applied on cropped and resized image focused on the lesions. It makes the subjective evaluation of experts more confident when the border are formally recognized by the naked eyes.

5.3.1 Implementation

The two methods developed for detection of the three regions illustrated by figures 4.4 and 4.5 are applied and implemented on standard camera images in the database described in subsection 5.2.3. Therefore, two extended models are applied defined by equations (4.13) and (4.14) representing the separation and the inclusion of the two sets ϕ_1 and ϕ_2 respectively.

In this section, the methodology of implementation is presented, the different parameters used and the illustration of some images presenting the advantages and limitations of the method are also highlighted. As mentioned above, the minimization of these

two methods, given by equation (4.19), is not performed in the current work. Then, the results obtained using both methods are presented and illustrated.

5.3.1.1 Segmentation by Inclusion

In this section, equation (4.14) is applied as illustrated. Figure 5.5 presents 4 image examples showing different segmentations obtained. From these examples, it can be seen easily that the algorithm developed follow perfectly the inclusion method explained in section 4.2. The segmentation by inclusion has an effect very important to distinguish between the different lesion darkness regions.

In Figure 5.5, four images are illustrated using the inclusion segmentation method. The first column of the figure shows the original images segmented, the second column illustrates the results of segmentation and finally the third one shows the different regions segmented accounting the background. In the second column, the size of images is reduced to show better the different lesions. The current method is very sensible to noises and borders inhomogeneity [178], as it can be visible in the sub-figure5.5h. For each image, all parameters used in the illustrated segmentation are given. Therefore, we notice that the parameter ν and dt are different for each image and chosen manually. These dependent parameters make the method very difficult for the automation.

5.3.1.2 Segmentation by Separation

The implementation of this second method provides the expected results as shown in figure 4.4. However, the separated cases in the current database are rarely visible due to the fast development of skin lesion [179]. Knowing that our algorithm in this case searches only the convergence of two separated sets. The following examples in figure 5.6 are chosen to illustrate some possible cases .

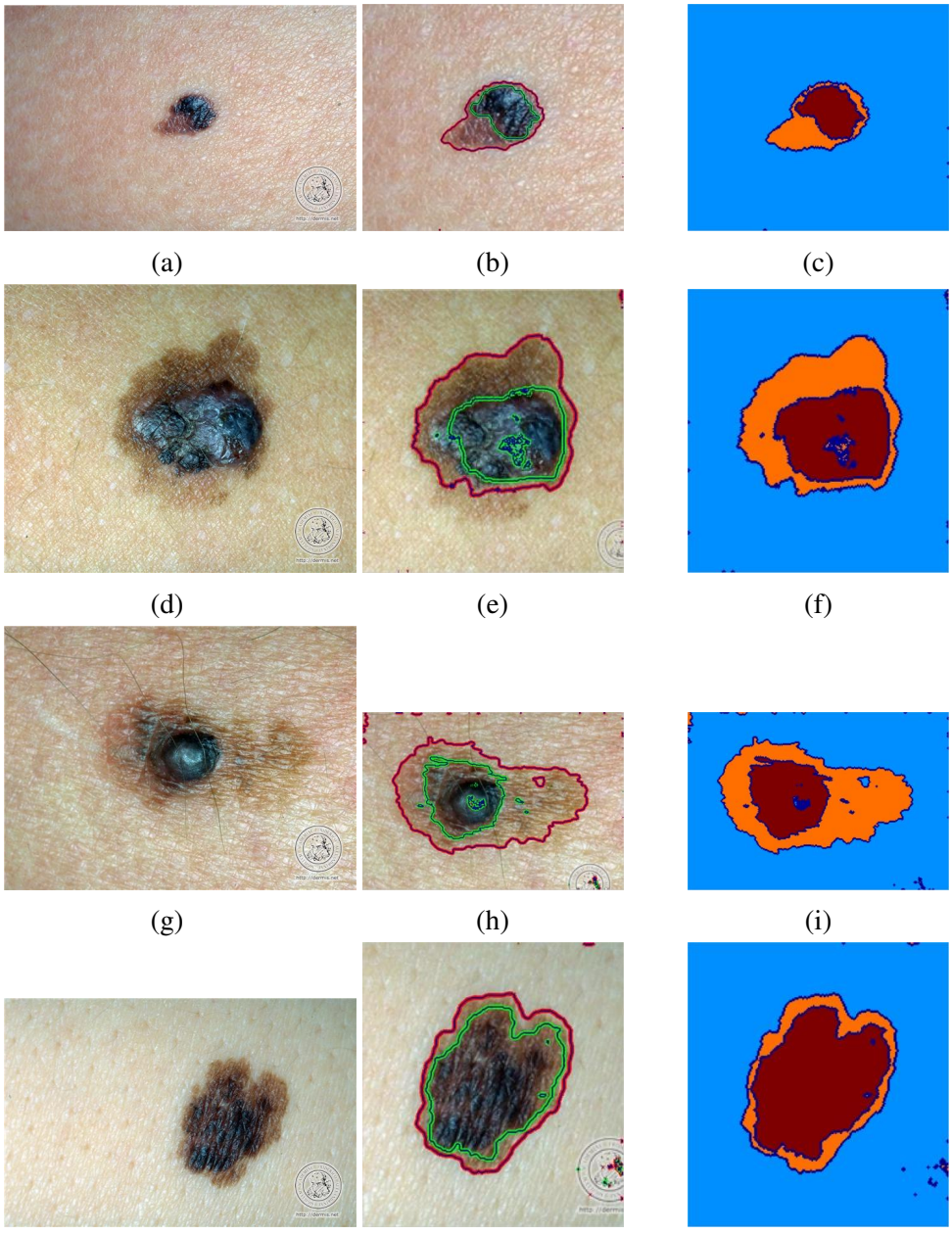

Figure 5.5: Implementation of the approach using equation (4.14) on images from DermIs database. (a): Original RGB image SSM18. (b): Segmentation of the two regions with $\nu = 0.2$ and $dt = 0.5$. (c): Global region-based segmentation. (d): Original RGB image SSM9. (e): Segmentation of the two regions with $\nu = 0.28$ and $dt = 1.5$. (f): Global region-based segmentation. (g): Original RGB image SSM11. (h): Segmentation of the two regions with $\nu = 0.07$ and $dt = 1.5$. (i): Global region-based segmentation. (j): Original RGB image SSM11. (k): Segmentation of the two regions with $\nu = 0.15$ and $dt = 0.3$. (l): Global region-based segmentation.

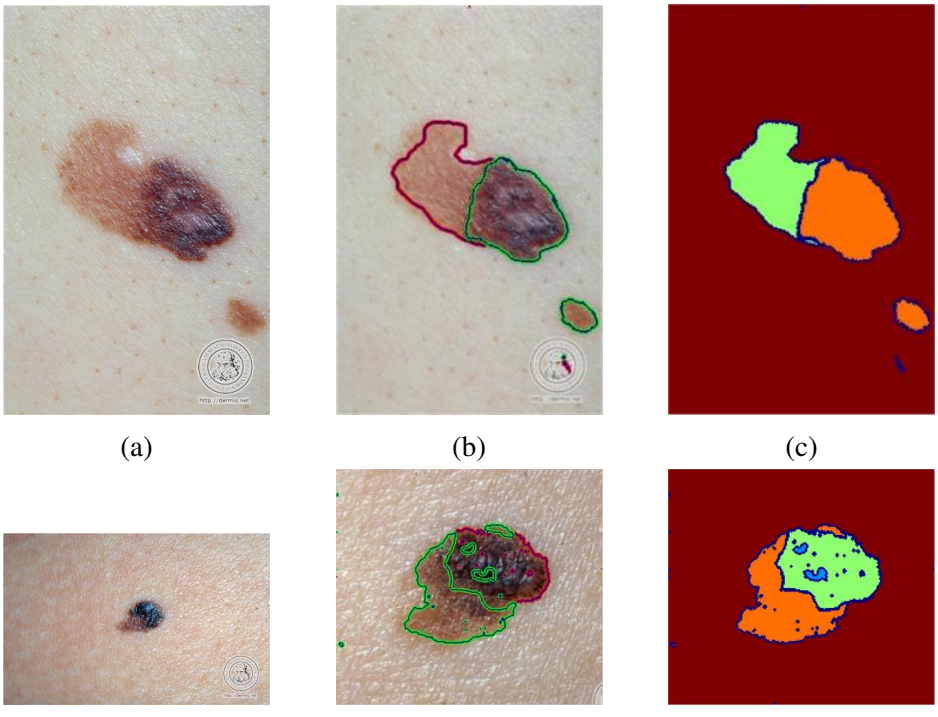

Figure 5.6: Implementation of the approach using equation (4.13). (a): Original RGB image (SSM34). (b): Segmentation of the two regions. (c): Global region-based segmentation.(d): Original RGB image (SSM18). (e): Segmentation of the two regions. (f): Global region-based segmentation

5.3.2 Obtained results

The evaluation of the developed method is highlighted by a subjective evaluation performed by three image processing experts into acceptable and unacceptable segmentation. For each acceptable segmentation a 3 choices of evaluation is proposed which are excellent, good and average. Table 5.3 explains how the experts evaluated the proposed method. In the first step, the experts evaluated the segmentation into acceptable and unacceptable, and in the second step they evaluated separately the acceptable ones into excellent, good or average segmentation. The second intermediate evaluation makes in evidence further the possible improvement of the proposed method. For each expert, only the protocol of evaluation is explained without any influence on their evaluation. Figure 5.7 illustrates an example of the four qualities segmentations explained in table 5.3. Due to the missing of information in the ground truth, it is very difficult to evaluate

the proposed extension using other evaluation methods such as Jaccard Index.

Table 5.3: Subjective evaluation rules.

Evaluation		Description
Acceptable	Excellent	It separates perfectly the two regions and improvement needed.
	Good	It separates very well the two regions but it can be improved
	average	It separates the two regions with small missed parts where the improvement of the segmentation is required.
Unacceptable		It cannot not recognize the two regions or big parts of the lesion are missed.

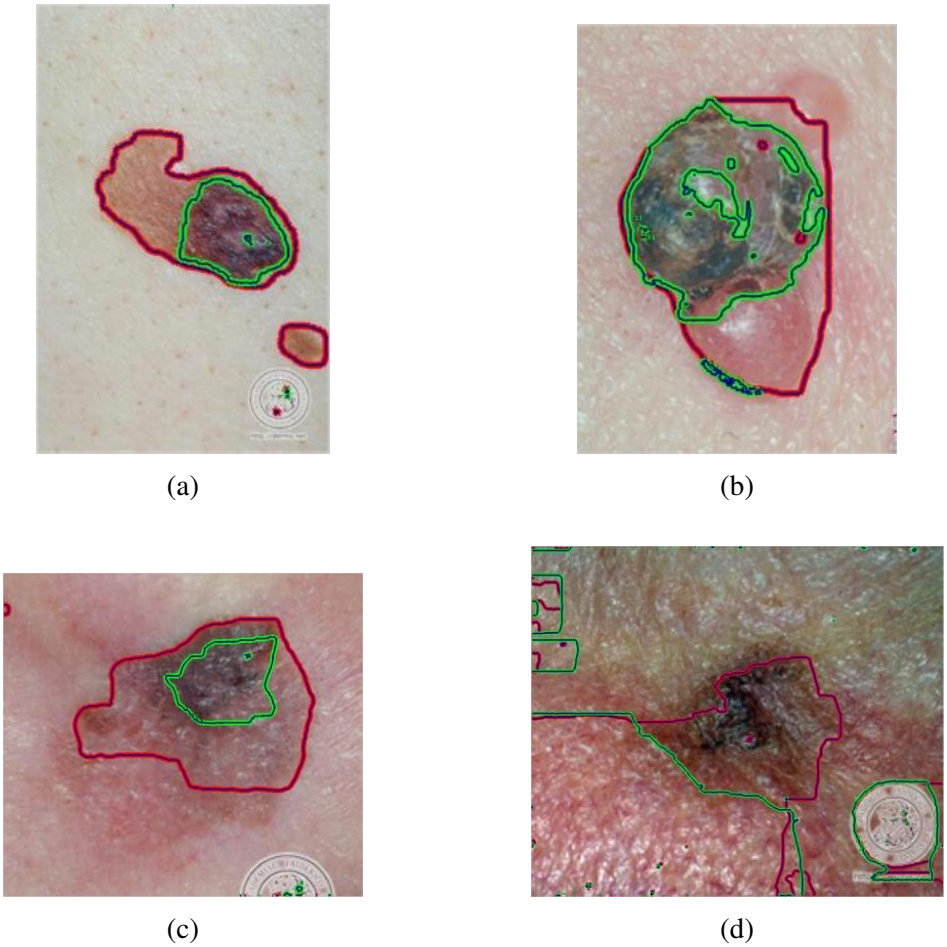

(a) (b) (c) (d)

Figure 5.7: Subjective evaluation examples. (a): Excellent Segmentation. (b):Good Segmentation. (c): Average segmentation.(d): Unacceptable segmentation.

Table 5.4 reports the results of the subjective evaluation performed by two image processing expert (the first expert and the third expert) and medical expert (the second expert). Thus, from the database used, only 2.38% and 6.98% are evaluated as the unacceptable segmentation by the image processing experts respectively. However the medical expert evaluated 9.30% of images as Unacceptable segmentation. For the excellent segmentation, 96.06%, 48.84% and 13.95% are evaluated by the first, second and the third experts. We can notice that the difference between experts are more visible than unacceptable case. The same difference between the experts is visible for good and average segmentation.

Table 5.4: Subjective Evaluation done by image processing expert on the results obtained from the extension of Chan and Vese model by inclusion method

Segmentation quality	First expert	Second expert	Third expert
Excellent segmentation	69.06%	48.84%	13.95%
Good segmentation	$21.42.\%$	23.26%	55.81%
Average segmentation	7.14%	18.60%	23.26%
Unacceptable segmentation	2.38%	9.30%	6.98%

Table 5.5 reports the results of experts for the two cases of evaluation, acceptable and unacceptable. It can be seen that more than 90% of segmentations are evaluated as acceptable by the three experts. Furthermore, these performances are obtained not only for the detection of lesion ROIs but also for the segmentation of the different development of moles in the skin lesion, which is the main objective of the proposed method.

Table 5.5: Subjective Evaluation done by image processing expert on the results obtained from the extension of Chan and Vese model by inclusion method

Segmentation quality	First expert	Second expert	Third expert
Acceptable segmentation	97.62%	90.70%	93.98%
Unacceptable segmentation	2.38%	9.30%	6.98%

It can be seen that for the medical expert, the results of acceptable segmentation is lower than image processing experts. It is explained by the expert that it is not acceptable to miss a malignant parts of the lesion, because to succeed the treatment of cancer they have to treat the whole lesion, and the missing of a small part of lesion can develop other malignant cells. It can be concluded that in hospitals that the false negatives are considered more dangerous than false positives.

Therefore, we can conclude that the proposed method of segmentation highlights the random development of melanoma, it is extended from Chan and Vese model. The objective of current method is to follow the development of the whole lesion and its particular parts of the lesion. The results obtained show an acceptable detection and segmentation over than 90%, and only less than 10% of wrong detection or missed parts in the segmentation. The subjective evaluation is performed by two image processing experts and medical expert. However, to process the current method in a typical CAD system, more developments are needed, specially the automation of all parameters of the model. These points are also discussed in the next chapter in perspective section.

5.4 Multi-resolution analysis results

The results presented in this section refer to the method explained in section 4.3.2. To enhance the quality of images used, the computation of the result was forwarded by the hair removing preprocessing using DullRazor Software as detailed in subsection 5.4.2.

Applying the method on a database of 200 dermoscopic images from PH^2 database [149]. This database contains 160 non melanoma (benign) and 40 melanoma (malignant) images. The classification is performed using SVM classifier with the linear kernel, 70% of the database are used for training and 30% for test. A random sampling cross validation method is applied to validate the obtained results, where thousand (1000) combinations of training and test sets are chosen randomly from the database. Thus, each image is used in average 700 times for training and 300 times for tests. An unbiased standard deviation (Std) for the thousand combinations is also computed for the three performance metrics.

The evaluation is performed between the three sets of skin lesions (common nevus, atypical nevus and melanoma). Thus, to get a representative training set from the benign lesions, 70% of each set are chosen separately as illustrated in figure 5.8. Two cases are computed and analyzed in this study, a separate case which is the recognition of melanoma mixed only with common nevus or atypical nevus. The second case is to recognize melanoma mixed with the whole benign lesions respecting the representativity of common and atypical nevus in training and test sets.

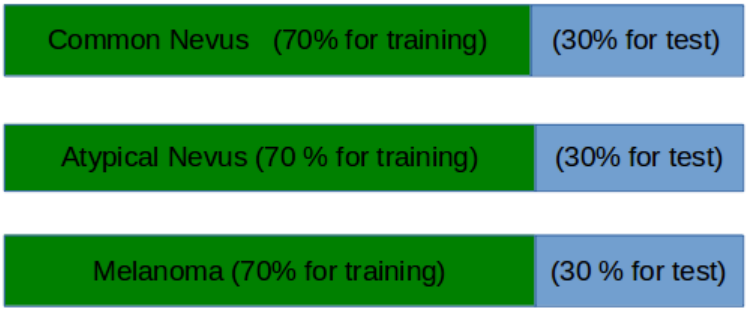

Figure 5.8: Training and test sets selection

The next subsections are organized as follow: Firstly, the technical details of the implementations, secondly the intermediate step which is image enhancement by hair removing and finally the obtained results and discussion.

5.4.1 Technical details

In this section, the details of the implementation are given and explained for further reproduction and comparison. Therefore, for structural features, curvelet and wavelet coefficients are computed for the first and second level. Thus, 9 curvelet coefficients matrices are extracted from each image. Then, for each curvelet coefficient matrix, $Energy$, $Entropy$, $Mean$, $Standard\ deviation$, $Maximum$, $Moment$ and $Homogeneity$ are computed. Then, 7 features from the first level and 56 features from the 8 different angles of the second level are obtained. For wavelet, Daubechies 4 transform is used, then 8 coefficient matrices are computed, 4 from the first level and 4 from the second level (one approximation coefficient matrix and three details coefficient matrices). Computing the same quantities as curvelet coefficient matrices, then for each level 32 features

are extracted. In total, 63 and 64 features are extracted from curvelet and wavelet transforms, respectively.

Depending on the variant of LBP operator as explained in section 3.4, we have 59 textural features from LBP^{u2}, 36 from LBP^{ri} and 9 from LBP^{riu2}. Indeed, in the experiments only radius $R = 1$ and eight neighborhood pixels ($P = 8$) are used.

The evaluation of the proposed method is measured using three performance metrics which are sensitivity (sen), specificity (spe) and accuracy (acc) [33], as given in equations (5.1) to (5.3).

$$sen = \frac{TP}{TP + FN} \tag{5.1}$$

$$spe = \frac{TN}{TN + FP} \tag{5.2}$$

$$acc = \frac{TP + TN}{TP + FN + TN + FP} \tag{5.3}$$

Where TP (True Positives) defines the melanoma classified as melanoma, TN (True Negatives) defines the non melanoma classified as non melanoma, FP (False Positives) and FN (False Negatives) are the non melanoma and melanoma which are not classified on the right set respectively.

Equation (5.3) depends on the number of benign and malignant lesions. To remove this dependence, we estimate the accuracy in the following way:

$$\hat{acc} = \frac{\alpha TP + TN}{\alpha TP + \alpha FN + TN + FP} \tag{5.4}$$

The parameter α is added to compensate the difference of images number in the accuracy performance. This parameter is obtained by the following formula:

$$\alpha = \frac{\#Benign}{\#Malignant} \tag{5.5}$$

Where $\#Benign$ and $\#Malignant$ design the number of benign and malignant images respectively. Therefore, $\alpha = 2$ for the first and second classification (melanoma vs

atypical, and melanoma vs common nevus) and $\alpha = 4$ for the last classification (malignant and benign lesions). The performance results are computed also by accuracy given by equation (5.4).

Equation (5.4) can be also used with different values of the parameter α to give more weight for false negatives or false positives to tolerate or reject some special situations, such as let cancerous patients without treatment which are false negatives. In our case, the α chosen is used just to regulate the difference between benign and malignant lesions. This formulation is equivalent to $(sen + spe)/2$ used in Barata et al. [141]. In the next section, the results show a significant difference between the two metrics.

Figure 5.9a presents the evolution of the modified accuracy ($\hat{acc}$) depending on different values of α, from 0.1 to 5, fixing other variables (sensitivity, specificity, malignant number and benign number). While, Figure 5.9b illustrates the dependence of the accuracy metric (eq.(5.3)) on malignant and benign number, presented by the dark curve. By varying the β value from 0.1 to 5 in $M = \beta B$, where M is malignant number, B is benign number, we can see easily that the accuracy (acc) is strongly dependent on those quantities. The blue color line presents the modified accuracy ($\hat{acc}$), with $\alpha = 1/\beta$, to compensate the difference between malignant and benign number.

Knowing that the database is presented in three different classes: Common nevus, Atypical nevus and Melanoma. Then, to have a representative training set, 70% of each class (common and atypical) is taken for training and the other 30% for test. This choice guarantees the representativeness of atypical and common nevus in training and test sets.

To detect melanoma lesions, the results are classified into three cases . Firstly, we explored the classification between melanoma and atypical nevus. Secondly, we explored classification performance between melanoma and common nevus and finally we performed the classification between melanoma and the whole benign lesions. Three performance metrics i.e. sensitivity, specificity and accuracy/modified accuracy given by equations (5.1) to (5.4) are computed. For each performance, we compute also 1000

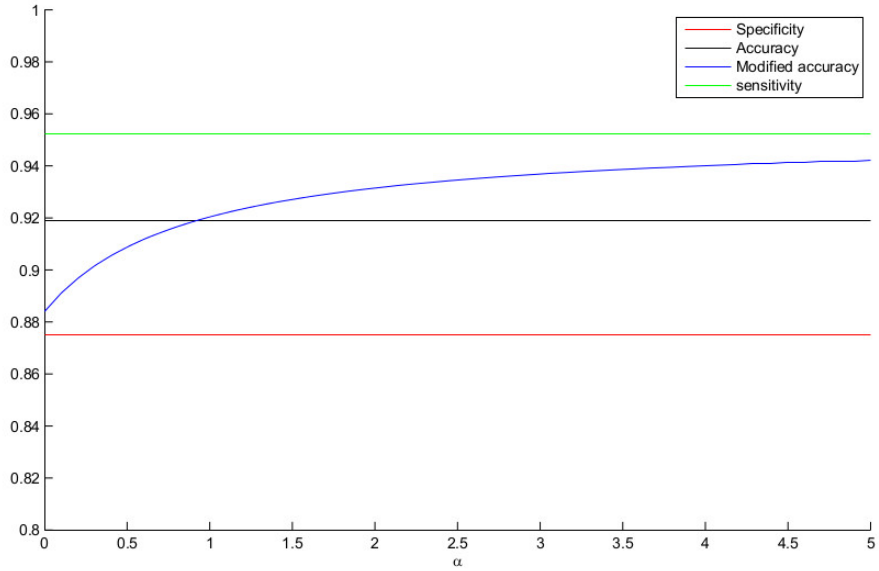

(a)

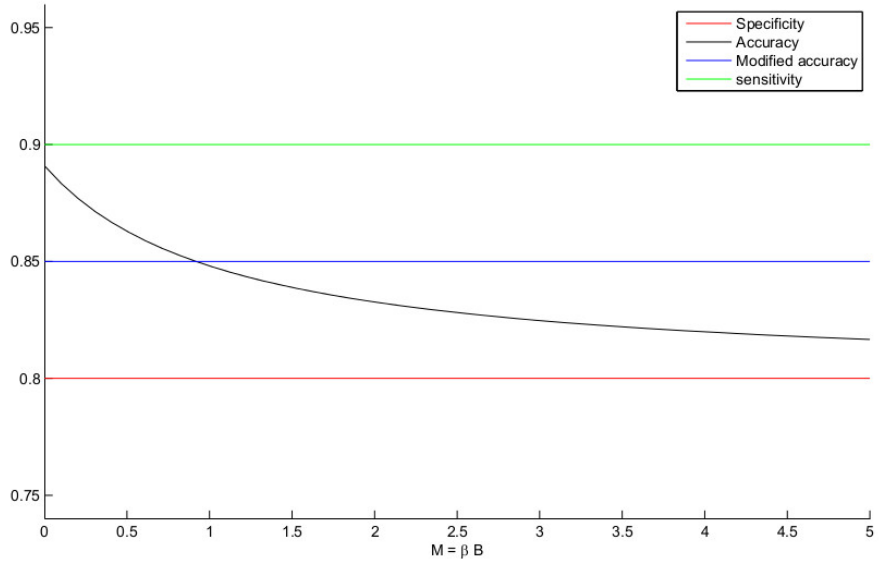

(b)

Figure 5.9: Illustration of the modified accuracy effect's on the obtained result using the formula given by equation (5.4). (a): Modified accuracy ($a\hat{c}c$) in function of α, presented by blue calor. (b):Accuracy (acc) depending on the number of malignant and benign lesions, presented by the dark color.

random combinations for the choice of the training and test sets which is the validation method N-random fold cross validation. In the result tables (5.7, 5.8 and 5.9), VP defines the validation performance and Std represents the standard deviation of the thousand combinations used for validation. The results are divided into three categories which are textural features using local binary pattern operator, structural features using wavelet and curvelet coefficients and finally the mixture of textural and structural features.

5.4.2 Hair removing

The preprocessing step is also implemented in the current work to enhance the image quality. Thus, DullRazor[1] Software is used for hair removing, it was applied on all the visible hairs as illustrated in figure 5.10.

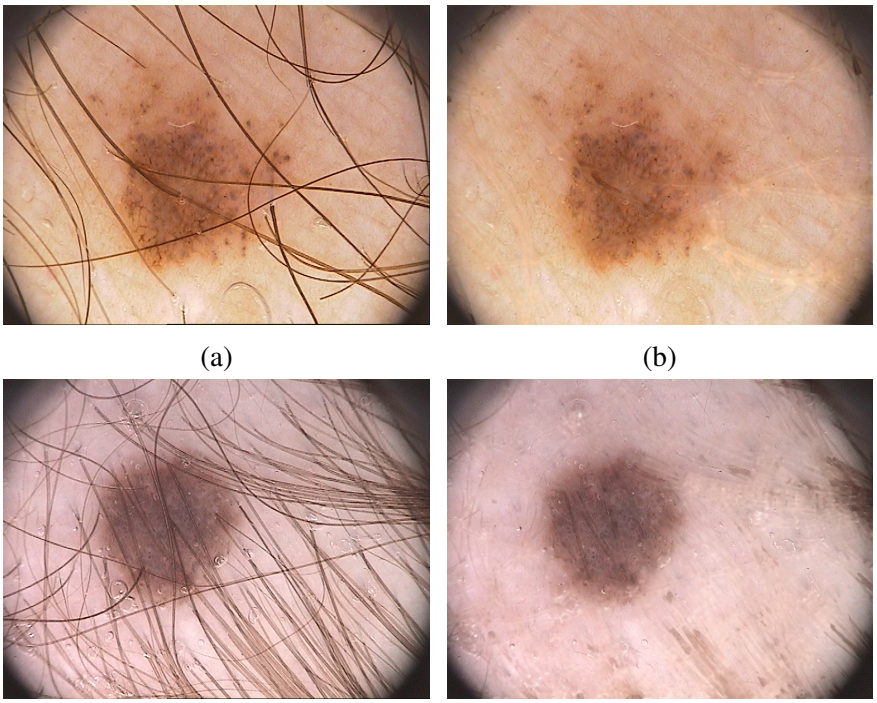

(a) (b)

(c) (d)

Figure 5.10: Hair removing with DullRazor software. (a,c): original images. (b,d): Dullrazor software treatment on the original images.

[1]DullRazor software is available on `http://www.dermweb.com/dull_razor/`

In figure 5.10, two kinds of hair removal are presented, thick and thin, under DullRazor software. It can be seen easily that the skin lesion is more clear and less influenced by the treatment when the hair is thick than thin as illustrated by figures (b) and (d), respectively. Despite that, even in the worst scenario, the lesion is more clear and efficient than before the treatment.

5.4.3 Obtained Results

The recognition of melanoma can be easier or either more difficult depending on the benign lesions set used for classification. Therefore, to reduce this effect of the database, two studies are done for the classification and recognition of melanoma mixed with each set of benign lesions and compared. the other classification is done between melanoma and the whole benign lesions respecting the condition of representativity explained below.

For each classification, 12 evaluation performances are computed. The three variant of LBP operator, wavelet and curvelet coefficients for the non-fusion cases. Six combinations are computed from the fusion of structural features (wavelet and curvelet) with textural ones (LBP variants). Finally, wavelet and curvelet coefficients are mixed, as explored by Li et al. [180] for image compression. Table 5.6 summarizes the number of features of the thirteen combinations studied in the current work. Each fusion is done by the concatenation of vectors obtained from each method.

Table 5.6: Number of features of studied combinations

Features	Methods	Features number	Fusion	Methods	features number
Textural Features	LBP^{ri}	36	Fusion of textural and structural features	LBP^{ri} + Wavelet	100
	LBP^{riu2}	9		LBP^{riu2} +Wavelet	73
	LBP^{u2}	59		LBP^{u2} +Wavelet	123
Structural Features	Wavelet	64		LBP^{ri} + Curvelet	99
	Curvelet	63		LBP^{riu2} +Curvelet	72
Wavelet + Curvelet		127		LBP^{u2} +Curvelet	122

The next subsections present firstly the result classification obtained between melanoma and atypical nevus, then melanoma with common nevus and finally between malignant and benign cases.

5.4.3.1 Melanoma Vs Atypical Nevus

In this part, the classification is focused on the detection and the recognition of melanoma mixed only with atypical nevus, those presented by the second and the third columns in the table 5.1. The results obtained are given in the table 5.7. Therefore, for textural features, the best performances are obtained by LBP^{u2} followed by the LBP^{ri}, and the worst result are obtained by the LBP^{riu2}. For structural features, wavelet shows better results then curvelet for all metrics performances used. The fusion of textural and structural features gives better results in wavelet coefficients with LBP operator and it shows a smallest standard deviation for the variability of validation results expressed by the variable Std. Wavelet with LBP^{u2} improves the three metrics used and gives the best results compared to all the methods and method combinations studied. The fusion of curvelet coefficients with LBP operator improves the sensitivity, specificity and accuracy metrics compared to curvelet and LBP separately. However, wavelet with LBP shows better results than curvelet with LBP.

From this first study, the dominant features are expressed $LBPP^{u2}$ and wavelet methods with an accuracy validation of 80.85% and 84.23%, respectively. It can be seen that the results obtained by the fusion of LBP^{u2} and wavelet shows the best performance with an accuracy validation of 85.20%. However, wavelet with LBP^{ri} and LBP^{riu2} is showing a result lower the wavelet method. In the other case, the fusion is of curvelet and and LBP variants is showing a better results than LBP and curvelet separately. It can be seen also that the the low results are obtained by th LBP^{riu2} variant, it can be explained by the few features used in this method (see table 5.6). Finally, the fusion of wavelet and curvelet, which is the last case studied in the table 5.7, is not showing any increase of performance, oppositely it shows lower performance than wavelet features.

Table 5.7: Results obtained for Melanoma Vs Atypical nevus giving Performance validation VP and the standard deviation Std for 1000 random-cross validation under SVM classifier.

Performances Metrics		Sensitivity (sen)		Specificity (spe)		Accuracy (Acc)		Accuracy ($\tilde{Acc}$)	
Features	Methods	VP	Std	VP	Std	VP	Std	VP	Std
Textural Features	LBP^{ri}	77.44%	11.88	81.97%	8.04	80.46%	5.82	79.70%	6.30
	LBP^{riu2}	74.17%	12.09	73.19%	9.29	73.51%	6.77	73.68%	6.83
	LBP^{u2}	76.55%	12.32	85.15%	7.35	82.28%	5.56	80.85%	6.31
Structural Features	Wavelet	79.47%	12.93	88.99%	7.10	85.79%	6.07	84.23%	6.84
	Curvelet	73.10%	13.56	82.01%	7.56	79.04%	6.14	77.56%	6.85
Fusion of Structural and Textural Features	Wavelet + LBP^{ri}	78.13%	12.08	88.63%	6.90	85.11%	5.49	83.38%	6.42
	Wavelet + LBP^{riu2}	77.51%	12.37	88.22%	5.80	84.62%	5.80	82.86%	6.81
	Wavelet + LBP^{u2}	81.84%	11.29	88.57%	6.80	86.31%	5.48	85.20%	6.24
	Curvelet + LBP^{ri}	79.08%	12.50	85.69%	7.34	83.49%	5.72	82.38%	6.08
	Curvelet + LBP^{riu2}	76.15%	13.31	82.84%	7.66	80.61%	6.25	79.49%	6.83
	Curvelet + LBP^{u2}	78.75%	11.89	86.83%	6.89	84.14%	5.51	82.79%	6.30
Wavelet + Curvelet		78.97%	12.84	85.51%	7.14	83.98%	6.01	82.24%	6.87

5.4.3.2 Melanoma Vs Common Nevus

As mentioned above, the second classification is done only between melanoma and common nevus lesions. Table 5.8 shows the validation performance of sensitivity, specificity and accuracies metrics. Thus, for textural features, LBP^{ri} and LBP^{u2} show a high performances than LBP^{riu2}, and it can be seen that LBP^{ri} is more sensitive and less specific than LBP^{u2}. The textural features performances show that wavelet coefficients discriminate melanoma better than curvelet coefficients and the fusion of the structural and textural features contributes in the reduction of the variability between different combinations in validation step.

It can be seen that the best results validation is performed using wavelet and the fusion of wavelet with different variant of LBP with an accuracy of $\approx 90\%$. The fusion of wavelet and LBP^{u2} is the most stable operator showing the smallest standard deviation value for the three me. It can be seen that wavelet is showing better results than the fusion of wavelet and LPB variants. Therefore, it can be concluded that the fusion has

Table 5.8: Results obtained for Melanoma Vs Common nevus giving Performance Validation VP and the standard deviation Std for the $100-$ random-cross validation under SVM classifier.

Performances Metrics		Sensitivity (sen)		Specificity (spe)		Accuracy (acc)		Accuracy ($a\tilde{c}c$)	
Features	Methods	VP	Std	VP	Std	VP	Std	VP	Std
Textural Features	LBP^{ri}	82.28%	11.11	84.29%	7.71	83.62%	5.72	83.29%	5.88
	LBP^{riu2}	78.92%	12.07	77.68%	8.35	78.09%	6.16	78.30%	6.40
	LBP^{u2}	80.82%	12.56	87.80%	6.78	85.47%	5.74	84.31%	6.70
Structural Features	Wavelet	88.47%	10.36	91.99%	5.67	90.81%	5.23	90.23%	5.65
	Curvelet	80.80%	12.25	84.53%	7.63	83.29%	6.20	82.66%	6.58
Fusion of Structural and Textural Features	Wavelet + LBP^{ri}	88.82%	9.44	90.95%	5.93	90.24%	4.97	89.88%	5.15
	Wavelet + LBP^{riu2}	88.91%	10.06	91.45%	5.85	90.60%	4.99	90.17%	5.54
	Wavelet + LBP^{u2}	89.25%	9.26	90.80%	5.59	90.28%	4.76	90.02%	4.92
	Curvelet + LBP^{ri}	81.25%	11.36	85.68%	7.30	84.20%	5.76	83.47%	5.25
	Curvelet + LBP^{riu2}	81.64%	11.93	85.34%	7.40	84.11%	6.23	83.49%	6.53
	Curvelet + LBP^{u2}	82.86%	11.12	87.17%	6.86	85.73%	5.48	85.02%	6.03
Wavelet + Curvelet		87.73%	10.57	90.40%	6.99	89.51%	5.68	89.06%	6.19

not more contribution on the performance metrics, but the fusion is more contributing on the standard deviation of the results obtaining 4.92 for wavelet + LBP^{u2} compared to 5.65 obtained by wavelet.

5.4.3.3 Melanoma Vs Atypical and Common Nevus

The last performance of the current study is the classification between malignant (melanoma) and benign (atypical and common nevus) lesions. The results are presented in table 5.9. Thus, for textural features, it can be seen that LBP^{ri} is more sensitive and more accurate than the two other variants of LBP operator. The highest specificity results are obtained using LBP^{u2} with a smallest variation compared to the other variants of LBP. The accuracy validation results show 81.76% and 82.10% for LBP^{ri} and LBP^{u2} respectively, and only 76.84% for LBP^{riu2}.

For structural features, wavelet coefficients showed a good performances compared

Table 5.9: Results obtained for Melanoma Vs Atypical and Common nevus giving Performance validation VP and the standard deviation Std for the $100-$ random-cross validation under SVM classifier.

Performances Metrics		Sensitivity (sen)		Specificity (spe)		Accuracy (acc)		Accuracy ($\tilde{acc}$)	
Features	Methods	VP	Std	VP	Std	VP	Std	VP	Std
Textural Features	LBP^{ri}	78.07%	12.35	86.14%	4.80	84.53%	3.89	82.10%	5.90
	LBP^{riu2}	77.74%	11.29	75.95%	5.92	76.31%	4.67	76.84%	6.02
	LBP^{u2}	74.13%	13.01	89.40%	4.52	86.34%	3.82	81.76%	6.28
Structural Features	Wavelet	77.56%	13.17	93.50%	3.48	90.31%	3.44	85.54%	6.54
	Curvelet	70.42%	14.50	89.29%	4.91	85.52%	4.41	79.85%	7.18
Fusion of Structural and Textural Features	Wavelet + LBP^{ri}	75.42%	13.68	93.46%	3.65	89.85%	3.52	84.41%	6.79
	Wavelet + LBP^{riu2}	76.73%	13.49	93.47%	3.59	90.12%	3.44	85.08%	6.67
	Wavelet + LBP^{u2}	78.93%	11.95	93.25%	3.61	90.34%	3.27	86.07%	6.32
	Curvelet + LBP^{ri}	72.35%	13.34	90.56%	4.41	86.92%	3.81	81.46%	6.55
	Curvelet + LBP^{riu2}	70.30%	14.76	89.19%	4.72	85.38%	4.24	79.74%	7.13
	Curvelet + LBP^{u2}	72.67%	12.88	91.09%	3.99	87.40%	3.61	81.88%	6.46
Wavelet + Curvelet		76.16%	14.11	93.13%	3.68	89.74%	3.95	84.64%	6.99

to curvelet coefficients with an accuracy performance of 85.54% and 79.85% respectively. These results gives an opposite conclusion to the ones obtained by Abu Mahmoud et al. [75] where the authors concluded that curvelet coefficients are more efficient than wavelet ones. This results could depend on the database used or the nature of features extracted (for further studies and comparison, Daubechies 4 wavelet transform is used).

The fusion of the wavelet and LBP^{u2} increases considerably the specificity and the accuracy performances and only wavelet with LBP^{u2} for the sensitivity as shown in table 5.9. However the fusion doesn't show a significant effect on sensitivity performance for the fusion of wavelet with LBP^{ri} and LBP^{riu2} respectively.

The best results for all the performances metrics validation is obtained by the fusion of wavelet coefficients and LBP^{u2} with 78.93% of sensitivity validation, 93.25 of specificity validation and 86.07% of accuracy validation. It shows also the smallest standard deviation for the thousand combination of random fold-cross validation used. However,

it can be seen that the fusion is not contributing on specificity compared to wavelet features but it obtained the same performance over than 93%. The Sensitivity which is the evaluation of the number false negatives is lower approaching a performance of 79%, and it should be improved.

5.4.4 Analysis and comparison

From tables 5.7, 5.8 and 5.9, we can deduce by using the two sets of features (textural and structural) that the detection of melanoma mixed with common nevus is easier as compared with melanoma mixed with atypical nevus, which is expected as the class overlap between melanoma and common nevus is less than that between melanoma and atypical nevus. Thus, in table 5.8 we obtained the same behavior of common nevus comparing to ABCD rule scoring system illustrated in figure 5.3. We can conclude that the detection and the recognition performances of melanoma depends on the kind of the benign lesions used for computation.

The fusion of wavelet and LBP^{u2} outperforms all the tested methods in the current work, as it can be seen from the results in tables 5.7,5.8 and 5.9.

In general, curvelets have better performances than wavelets. However, in our case, the results obtained show better performances from wavelet coefficients compared to curvelet coefficients in the three tables. These results can be explained by the multitude of singularity points coming from the random development of skin cancer lesions. It could also be expressed by the redundancy of curvelet coefficients which represent the double of the redundancy of wavelet coefficients [181].

As detailed in section 3.3, wavelets are efficient for singularity points and curvelets are more efficient for the detection or characterization of curves. Therefore, we also evaluate a fusion between the two sets of (wavelet and curvelet) coefficients as Li et al. [180] used for image compression. Thus, the results obtained are not showing any significant improvement in the detection and classification of benign and malignant lesions.

Table 5.10: Comparison of the results of proposed approach with the results of recent methods in the literature using the same database

Method	Method used	sensitivity	specificity	accuracy
Abuzaghleh et al. [118] (2014)	The authors used color and shape geometry features using Fast Fourier Transform (FFT) and Discrete Cosine Transform (DCT). SVM classifier is used on PH^2 Database for 75% for training and 25% for test.	–	–	90.6%
Bi et al. [132] (2016)	The authors used multi-scale lesion-biased representation under joint reverse classification on PH^2. However, the authors did not cross validate the obtained results.	87.50	93.13	90.31%
Barata et al. [141] (2015)	Four algorithms to extract color constancy (Gray World, max-RGB, Shady of Gray and General Gray World). SVM classifier with the χ^2 kernel is used for classification on PH^2 database.	$\mathbf{92.5}\%$	76.3%	84.3%
Proposed method	A fusion textural and structural features. Results of random sampling cross-validation under SVM classifier with the linear kernel used for classification on PH^2 database with 70% for training and 30% for test.	78.93%	**93.25%**	**86.07%**

Table 5.10 presents a comparison of the proposed method with recent works on classification and recognition of melanoma using the same database PH^2. Our proposed method shows the highest performance in terms of specificity and accuracy compared to Barata et al. [141], showing a validated result of 93% and 86% respectively. Although accuracy is higher for Abuzaghleh et al. proposition [118] and Bi et al. [132], they did not perform any validation comparing neither the current work validated by $n-$random sampling cross validation, nor $k-$fold cross validation used by Barata et al. In addition to this, the Abuzaghleh et al. [118] used 75% of the database for training in place of 70% frequently used in the literature. The authors used the fusion of fast Fourier transform with discrete cosine transform, and their results are still less efficient than the proposed method due to the lack of validation of their results. Table 5.11 and figure

Table 5.11: Comparison of the results of proposed approach with the results of recent methods in the literature using the same database

Acc $< 65\%$	$65\% \leq$ Acc $< 75\%$	$75\% \leq$ Acc $< 85\%$	$85\% \leq$ Acc $< 95\%$	Acc $\geq 95\%$
2	37	328	585	48

5.11 are showing the importance of validation, where wa can choose a specific training and test sets to obtain higher result. In addition the this, the authors did not present sensitivity and specificity performances, and no information on training and test sets is presented. Therefore, it is difficult to reproduce the same result for comparison. Furthermore, knowing that the benign lesions are heterogeneous [2], then, if we choose some special configurations of training and test sets we could present higher results than those presented in tables 5.7, 5.8 and 5.9. Thus, the validation result step is crucial for the adaptability of the proposed method.

The known ABCD rule, often used in hospitals manually, has achieved an accuracy of 87.5% as in table 5.2. In this work, the proposed automation of the ABCD rule achieved an accuracy of 86.07% as in table 5.10, which is fairly comparable to the result obtained manually. This achievement shows a great potential of developing CAD system for melanoma detection.

In order to show the importance of the cross validation methods for the obtained results, table 5.11 reports the accuracy performance obtained for each combination of the $1000-$random fold cross-validation used by the proposed method by intervals. Figure 5.11 illustrates the histograms of the thousand combinations. Thus, a probability of 0.633 to obtain an accuracy greater than 85% and only 0.141 to get an accuracy smaller than 80%, and a probability of 0.279 to get an accuracy greater than 90%. Then, without a cross validation methods, it will be difficult to compare objectively between methods.

To conclude, the proposed method achieved the second objective of the current work which is an exploration of sets of features to make a border between benign and malignant lesions. Thus the method shows a significant set of features describing better melanoma and benign lesions. The set of features includes textural and structural

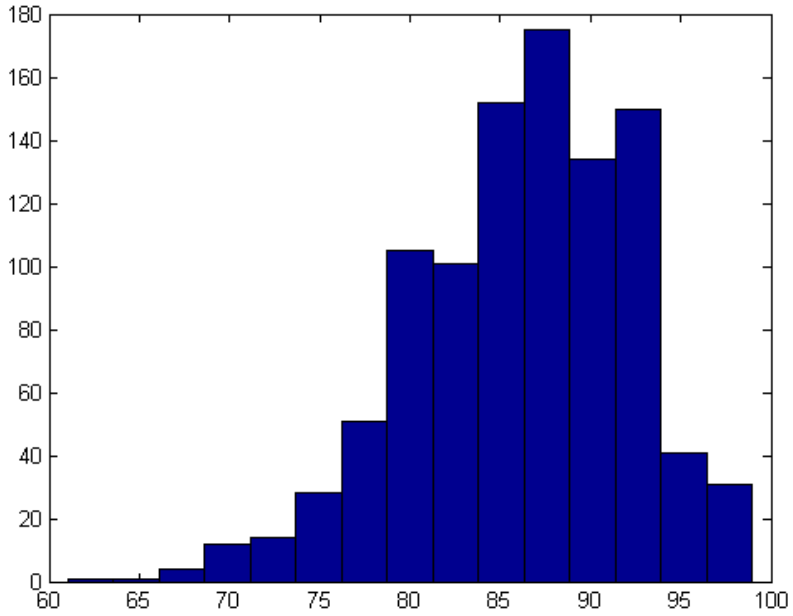

Figure 5.11: histogram of the thousand combinations results for accuracy metric

features extracted respectively from local binary pattern and wavelet and/or curvelet transforms.

The obtained results are performed and validated using the fusion of different combinations of these features under SVM classifier. They are also compared to the previous results presented in the literature performed on the same free public database PH^2. The recognition of melanoma were highlighted mixing with common nevus, atypical nevus and the whole benign lesions. The obtained results are validated using n-fold random sampling cross validation method. This validation is to increase the confidence of the obtained results on different databases which is very important in a typical CAD system.

The results show an accuracy performance of 86.07% for melanoma mixed with the whole benign lesions, 85.20% for melanoma mixed with atypical nevus and finally a performance accuracy of 90.17% for melanoma mixed common nevus. In fact, addition to the performance highlighted in this work, an other contribution consists on the dependence of the performances on the diversity of benign lesions. Thus, more there are common nevus cases, more the performances should be better as it can be seen from the results presented in the two tables 5.7 and 5.8 referring to atypical and common nevus,

respectively.

5.5 Results of Border features

The results presented in this section refer to the method developed in section 4.3.3 applied on a database of 166 standard camera images detailed above in section 5.2.3. Therefore, the proposed method extracts the irregularity border features exploring valleys and crevasses concepts illustrated in figure 4.17. Depending on the number and size of valleys and crevasses detected, for each image 8 different features are extracted, as summarized by equation (4.31). Then, using this set of features, the classification is performed utilizing Support Vector Machine (SVM) with linear kernel.

In the current section, the standard image orientation step is also implemented to normalize all images of the database in the same and common view. This normalization is summarized in algorithm1 and illustrated below in section 5.5.1.1.

Different implementations are explored with the proposed method, one with and the other one without the preprocessing (standard image view) step described above. A comparison between the original and standard image view is also done. The main method of the current work includes the preprocessing step. The following points enumerates the procedure of implementation:

1. Implementation of the proposed method in its integrity using the both algorithms presented in subsections 4.3.3.1 and 4.3.3.2.

2. Implementation of only the first algorithm proposed in subsection 4.3.3.1 for standard view images and its comparison with original images.

Therefore, two kinds of results are presented. Firstly, the main result given by the whole algorithm using border features presented in the previous section. The second result shows the intermediate contribution of standard view images and the effect of the preprocessing step on the proposed method.

5.5.1 Implementation

The implementation describes the preprocessing step detailed in section 5.5.1.1 as the first stage of the algorithm and the extraction of features from border irregularities given in section 4.3.3 as the second stage.

5.5.1.1 Standard view implementation

The single presentation and orientation of malignant and benign melanoma gives the same features characteristics for all images of the database. Therefore, the implementation of the Standard Image Orientation Algorithm (see Algorithm 1) on some skin lesion images (malignant and benign melanoma) is illustrated to show the reorganization and the view standardization of these images.

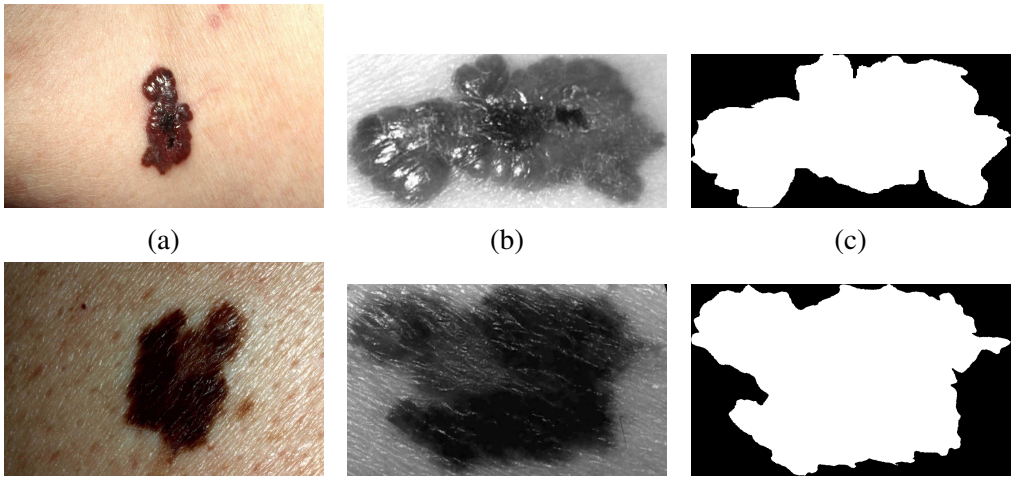

(a) (b) (c)

(d) (e) (f)

Figure 5.12: Single orientation of melanoma sample from DermQuest Database [5]. (a): original malignant image NM61. (b): gray level ROI of the oriented ROI of NM61 image. (c) Binary ROI of the oriented ROI of the image NNM61. (d): Original Malignant image (SSM74). (e):gray level ROI of the oriented ROI of SSM74 image. (f) Binary ROI of the oriented ROI of the image SSM74.

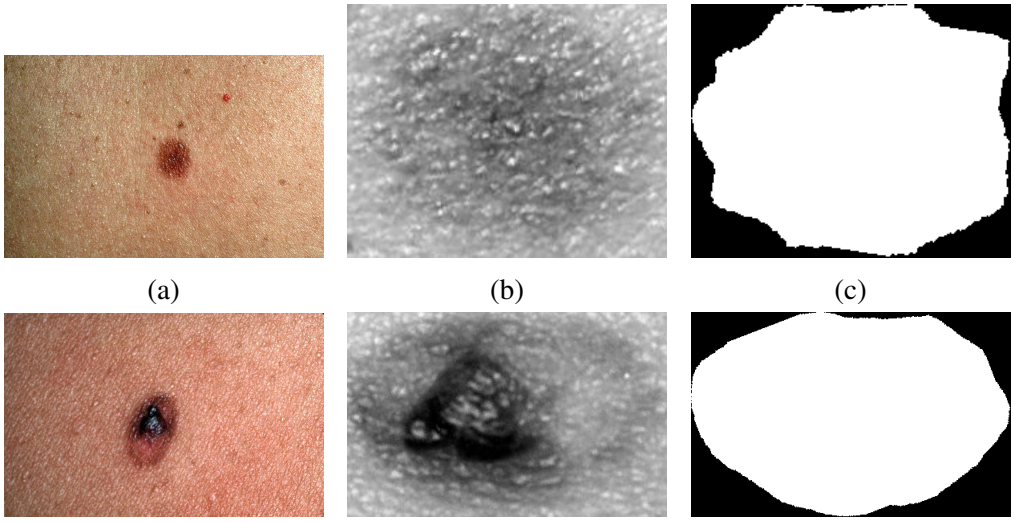

Figure 5.13: Single orientation of benign lesions sample from DermQuest Database [5]. (a): original benign image D45. (b): gray level ROI of the oriented ROI of D45 image. (c) Binary ROI of the oriented ROI of the image D45. (d): Original benign image D54. (e):gray level ROI of the oriented ROI of D54 image. (f) Binary ROI of the oriented ROI of the image D54.

Figures 5.12 and 5.13 show the effect of making images in the same orientation. It can be seen easily that the border in binary image representation is a good descriptor between malignant and benign lesions. It can seen also that the area between pigment and its box is minimized. As mentioned above, the performances of this standardization are presented in section 5.5.2.3 and illustrated in Fig.5.15 in comparison with the original view.

5.5.1.2 Border irregularities implementation

The implementation of proposed work in section 4.3.3.2 is presented and illustrated in the current section.

The detection of border irregularity uses the notion of crevasse and valley as illustrated in Fig.4.17. This algorithm is applied on standard camera image database. The first classification following the number of valleys and crevasses detected are shown in tables 5.12 and 5.13. The results of the two first features of $feat$ given in equation

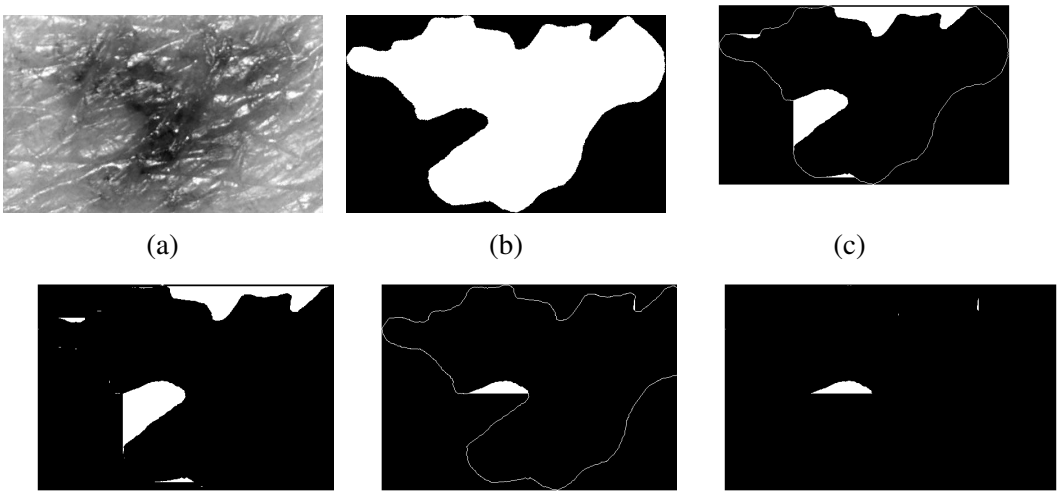

Figure 5.14: Illustration of main stages of border irregularities. (a): Original gray level image. (b): Binary ROI image. (c): valleys areas detected with the edge of the ROI. (d): Valley areas detected (13 elements). (e): Crevasse areas detected with the edge of the ROI. (f): Crevasse areas detected (3 elements).

(4.31), which are $N(v)$ for number of valleys detected and $N(c)$ for number of crevasses detected, are presented and discussed.

Figure 5.14 describes the different steps of valleys and crevasses detection. This example shows well the different sizes of valleys and crevasses. It can be seen easily that the irregularities are exploring the small areas locally and the large areas globally.

5.5.2 Obtained Results

Two results are presented in this section, statistical analysis to illustrate the effect of valleys and crevasses concepts introduction, and SVM classification on the obtained features.

5.5.2.1 Statistical analysis of the results

The number of detected valleys are computed and divided into equidistant segment with length 5 from 0 to 50 as presented in table 5.12. From this table, it can see that

Table 5.12: Number of detected area in equidistant segments using first level of irregularity (horizontal $\bigcup$ vertical). Valley geometrical forms

number of elements	malignant melanoma (99 images)	benign melanoma (67 images)
0 sets	0($\approx 0\%$)	0 ($\approx 0\%$)
[1-5]	2 ($\approx 2\%$)	9 ($\approx 13.4\%$)
[6-10]	5 ($\approx 5\%$)	15 ($\approx 23.9\%$)
[11-15]	22 ($\approx 22\%$)	15 ($\approx 22.4\%$)
[16-20]	25($\approx 25\%$)	14 ($\approx 20.8\%$)
[21-25]	15 ($\approx 15\%$)	10 ($\approx 14.9\%$)
[26-30]	16 ($\approx 16\%$)	3 ($\approx 4.4\%$)
[31-35]	4 ($\approx 4\%$)	0 ($\approx 0\%$)
[36-40]	4 ($\approx 4\%$)	0 ($\approx 0\%$)
[41-45]	4 ($\approx 4\%$)	0 ($\approx 0\%$)
[46- ...]	2 ($\approx 2\%$)	0 ($\approx 0\%$)

for $N(v) > 25$, malignant melanomas present 30% of the database valleys against less than 5% for benign melanoma. In the same time, for the number of detected valleys [1 to 5] 13.4% are found for benign melanoma and only 2% for malignant melanoma. Using valleys concepts, around 50% of the data can be selected and classified. However from 11 to 25 valleys detected number is almost the same between benign and malignant melanoma. We conclude from this table that the malignant melanoma has more chances to contains more valleys than benign lesions.

Table 5.13 presents the number of crevasses detected with segment length of 2 from 0 to 14. Thus, from the table the absence of crevasses in benign lesions presents around 40% compared to malignant melanoma where only 6% without any crevasse are detected. Even if the crevasses exist in benign melanoma, in average, there are more in malignant than benign ones. In the other side, melanoma cases contain more crevasses with around 23% against 6% for benign lesion when $N(c) > 5$. From this table, the conclusion is that benign lesions contains less crevasses than malignant cases.

The two tables (5.12 and 5.13) describe perfectly the idea of border irregularity of ABCD rule with more deep analysis and study. The introduction of the two concepts (valleys and crevasses) as first and second level of border irregularity feature increases the detection and helps more the understanding of the feature itself.

Table 5.13: Number of detected area in equidistant segments using second level of irregularity (horizontal $\bigcap$ vertical). Crevasse geometrical forms

number of elements	malignant melanoma (99 images)	benign melanoma (67 images)
0 sets	6 ($\approx 6.1\%$)	27 ($\approx 40.3\%$)
[1-2]	38($\approx 38.4\%$)	24 ($\approx 47.1\%$)
[3-4]	26 ($\approx 26.3\%$)	12 ($\approx 17.9\%$)
[5-6]	12($\approx 12.1\%$)	2 ($\approx 3\%$)
[7-8]	7($\approx 7.1\%$)	1 ($\approx 1.5\%$)
[9-10]	7 ($\approx 7.1\%$)	1 ($\approx 1.5\%$)
[11-12]	1 ($\approx 1\%$)	0 ($\approx 0\%$)
[12-...]	2 ($\approx 2\%$)	0 ($\approx 0\%$)

To improve these statistical analysis results, the size of the detected valleys and crevasses using different thresholds to discriminate better the benign and malignant lesions is added, as explained in section 4.3.3 and summarized by equation (4.31). Therefore, a machine learning via SVM training and classifier are applied on the feature set obtained. The obtained results are presented in subsection below (subsection:5.5.2.2).

5.5.2.2 SVM classification on border irregularity features

Support Vector Machine (SVM) classifier is used on a database of 166 skin lesions images (67 benign lesions and 99 malignant melanoma), it is applied on different integer values of the threshold τ_v ($\tau_v \in [0, 100]$) as given in equation (4.31). The other threshold τ_c mentioned in the equation is fixed empirically to 2.5. This choice reduces considerably the complexity of the algorithm and time running. Thus, the features extracted are used as input for the SVM classifier with linear kernel following 70% (69 malignant, 45 benign) for the training and 30% (30 malignant, 22 benign) for the test. Table 5.14 shows different results for $\tau_v \in (0, 10, 20, 30, 40, 50, 60, 70, 80, 90)$ adding to that the optimum value of τ_v showing the best results.

Table 5.14: Result of SVM classifier using the extracted features following the different values of the threshold τ_v.

τ	sensitivity	specificity	accuracy
0	73.33%	72.73%	73.08%
10	60%	95.45%	75%
19	$\mathbf{80}\%$	$\mathbf{95.45}\%$	$\mathbf{86.54}\%$
20	80%	90.91%	84.61%
30	86.67%	77.27%	82.69%
40	80%	68.18%	75%
50	86.67%	68.18%	78.85%
60	83.33%	72.73%	78.85%
70	86.67%	72.73%	80.77%
80	83.33%	81.82%	82.69%
90	86.67%	63.64%	76.92%

Table 5.14 presents the results of classification using different thresholds τ_v. The results are performed following three performance metrics which are accuracy (acc), sensitivity (sen) and specificity (spe).

The result shows a maximum of accuracy of 86.54% given by $\tau_v = 19$ with sensitivity of 95.45% and specificity of 80%. it can be seen from this table that the good result of the sensitivity for big values of τ_v i.e more than 83% for all $\tau_v \geq 50$. The opposite is seen for the specificity where it gives irregular values when $\tau \geq 50$, from 68.18% to 81.82%.

For the threshold $\tau = 0$ (Table 5.14), more than 72% of sensitivity, specificity and accuracy performances are obtained. This result represents the information extracted from border features by the proposed method and the effect of these new concepts introduced in this work (valleys and crevasses).

5.5.2.3 *Standard image view contribution*

The normalization of the database is one of the keys contributing to result improving of the method proposed. It shows the impact of making all images in the same view. However the choice of horizontal, vertical or oblique view has no any effect.

Figure 5.15 shows the effect of preprocessing step. The intermediate contribution of the standard view presented in section 4.3.3.1 using the same training and test sets on SVM classifier. The graph illustrates the accuracy performance of the same database between the original orientation and the proposed standard view. Therefore, from the graph it can be seen easily that the accuracy for all thresholds (from 0 to 100), shows greater results in standard view than the original images. The maximum of accuracy in original is only 78.85% compared to standard view images which is 86.54%.

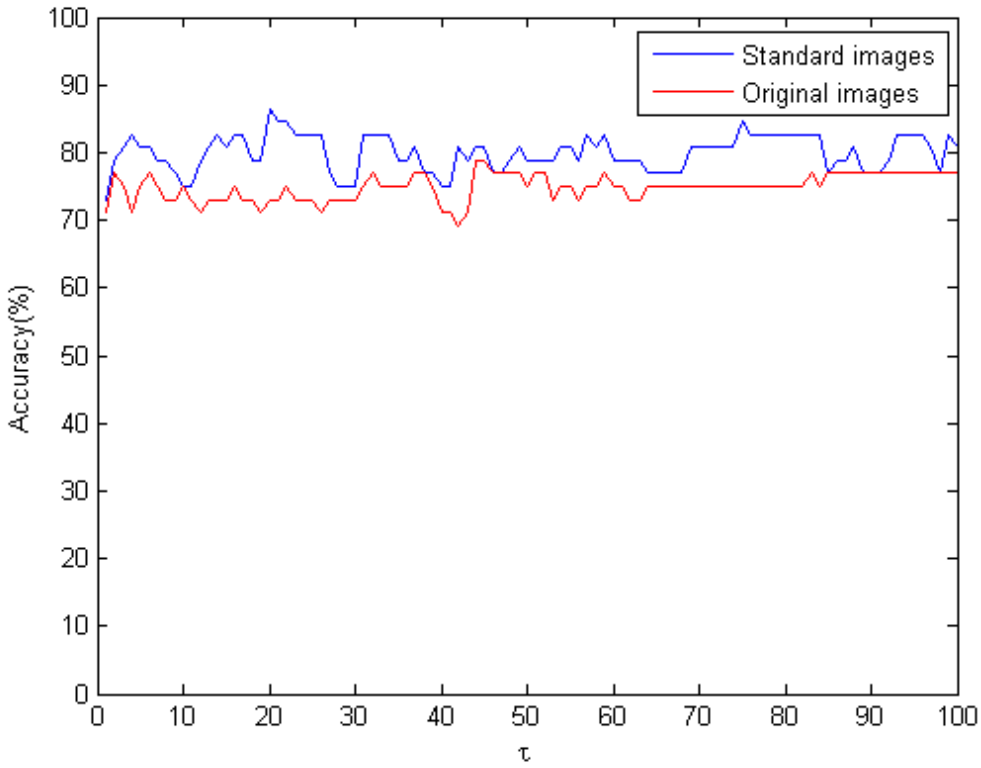

Figure 5.15: Accuracy of standard view and original images using border features presented in the current method. blue (up) : proposed standard view images, red (down): Original images.

5.5.2.4 *Comparison with existing methods*

In this subsection, the obtained results are compared with the method used by Amelard et al. [105] (2014). Using the same database from dermQuest [5] and DermIs [4], our results outperforms significantly those presented by Amelard et al. as shown in Table 5.15 with an accuracy of 86.26% obtained by the proposed method to an accuracy of 81.26% obtained by Amerald et al.

In addition to that, as mentioned above, a preprocessing of the database is also done to clean all the redundant images as illustrated by figure 5.4 where the same image were acquired at different distance.

Table 5.15: Comparison of the obtained result with the existing method using the same database.

Method	Approach used	Accuracy
Amelrd et al. [105] (2014)	Illumination correction algorithm quantifying asymmetry and border irregularities characteristics.	81.26%
Proposed method	Border irregularity features on standard view images	$\mathbf{86.54\%}$

Thus, by the proposed method, the border of pigment lesions is studied to discriminate the malignant and benign lesions on standard camera images. Therefore, the border irregularity of each pigment are deeply explored. In the literature, most of methods studied the irregularities following the two axis x and y giving some score as used in ABCD rule. The proposed method extracts a small set of features containing 8 irregularity border features. The obtained results are encouraging and showing higher performances comparing to the literature on the same database.

To conclude, in the current work, two ideas are proposed and explored. Firstly, the introduction of valleys and crevasses concepts for the irregularity of lesion borders, and secondly the standard view of the whole database with its impact on the result as it

presented and illustrated in figure 5.15, where the standard view results is compared with the image original randomly acquired. The implementation of these two ideas shows an accuracy of 86.45% compared to amelard et al. [105] where the authors used illumination, asymmetry and border irregularities and obtained only 81.26%.

CHAPTER 6

CONCLUSIONS AND RECOMMENDATIONS

In this chapter, all research works presented in this thesis are summarized in section 6.1, where the objectives enumerated in section 1.5. Then, The limitations of presented methods and their perspectives are introduced and discussed in section 6.2.

6.1 Conclusion

The main aim of this PhD work is to propose a mathematical methods to automate the detection of skin cancer. The main issue of this thesis is to treat the different output images in skin cancer. Therefore, in the current work, the majority of image category acquisition, which are standard camera images and dermoscopy images, are treated to improve the CAD system for skin cancer. The work is separated into two parts following these two categories of input images.

In the current work, two main tasks were treated, firstly the development of an adapted segmentation for skin lesions, and secondly the classification of lesions into malignant and benign cases using a sets of discriminative features. This second part is also divided into two distinguished methods depending on the input image.

6.1.1 Part I: Segmentation method

In this part, the research on the segmentation of skin lesion is focused on the development of new approach of skin lesion segmentation based on Chan and Vese Model. It

has the particularity to segment the the random development of melanoma lesion. This approach is applied and evaluated on skin cancer coming from standard camera images given in DermIs and DermQuest databases. One of Chan and Vese model particularities is its high sensibility to different edges and colors. The skin cancer is recognized principally by sets of rules defined by dermatologists and researchers which are ABCD rule and 7-point checklist. Our proposed approach can be considered as a specialization in one side and a generalization in other side of Chan and Vese model. Therefore, a choice of one specific combination treats the segmentation deeply compared to the original Chan and Vese model. In the second view, all the combination of Chan and Vese model are treated in the current approach.

The approach is evaluated using the subjective evaluation method. The results obtained shows a high performance of the proposed method for the used database. Although, a Jaccard index method could be applied to evaluate the proposed method. However, the ground truth given for these images shows only the whole lesion and not the specific level lesions basing on the color and intermediary borders. The method answered to the first objective of adaptive segmentation. However, it is not fully automatic due to the manual fixed parameters of the original method.

The main contribution of the proposed approach is more theoretical, and it can be applied on other kind of images. Therefore, it explains the generalization of the model for different more cases than the original model.

6.1.2 Part II: Feature extraction

This second part summarizes the two methods developed to extract the main features of skin lesions for their classification into benign and malignant lesion. Firstly, the border irregularities of lesions applied on standard camera images is explored. Secondly, a new descriptor based on a mixture of structural and textural features is developed. This second approach was applied on dermoscopy images from the free database PH^2.

1. The first method of feature extraction is based on different combinations of structural and textural features to select the best discriminative set for the classification of benign and malignant lesions. Therefore, for structural features, a multi-resolution analysis was explored using wavelet and curvelet transforms. While, the textural features are extracted using local binary pattern operator. The method was also cross validated by $n-$random sampling cross validation using 1000 random combinations. The method highlights the performances of three skin lesions sets from PH^2 database, which are common nevus, atypical nevus and melanoma. The results obtained show a higher performances in term of accuracy, sensitivity and specificity in case of wavelet-local binary uniform pattern fusion. This method is answering to the second objective of feature extraction based on the the fusion of structural and textural features.

2. The second method of feature extraction is based on the border irregularities behavior. The method explored a new concept of border representation, where two kinds of features are extracted from the border, which are valleys and crevasses geometrical forms. These two new concepts can considered as first and second level of lesion border irregularities. These features are learned by SVM classifier with linear kernel. The results obtained show a higher performances of classification compared to the literature's results using the same database. This idea of characterization of border could be implemented in a typical flow of ABCD rule method, it represents more variability than the method based on eight segments from the border used currently in ABCD rule. The challenge fixed in the third objective , which is the exploration of the border irregularities in formation of, is achieved.

A comparison of these methods with previous work in the literature are highlighted and discussed in the last chapter. All details of proposed methods are explained as suggested in the literature. In addition to that, for all methods proposed, only the free benchmark databases, which are DermIs and DermQuest for standard camera images and PH^2 for dermoscopy images, are used.

6.2 Future directions

Despite the several developed approaches, to our knowledge, there is no CAD system available for medical doctors that can perfectly discriminate melanoma. Thus, there is a need to explore new directions in skin cancer detection using images processing. Therefore, the main directions for further work can be itemized in general and specified perspectives. The specified ones include:

- Minimization of the segmentation proposed for the extension of Chan and Vese model expressed by equation (4.12) using random forest or gradient descent methods. This perspective is one of the main directions of the current work. It present a new view of segmentation in image processing.

- The automation of all parameters of Chan and Vese model and its generalizations. This issue makes the segmentation using this method very difficult for non-image processing experts. Therefore, the artificial neural network such as Conventional Neural Network which could be a good compromise method to resolve this issue.

The general perspectives includes some main points about the methodology of work in skin cancer detection domain, such as:

- A systematic validation of all obtained results. We highlighted this point in the fusion of structural and textural features. Thus, it allows for the future work the more visibility for the best direction of research. It increases also the efficiently of results comparison.

- The highlighting of proposed and explored methods in public free database in addition to their private databases such as PH^2 and ISIC (International Skin Images Collaboration *in process*) databases to easily validate the comparison between methods.

REFERENCES

[1] Germán Capdehourat, Andrés Corez, Anabella Bazzano, Rodrigo Alonso, and Pablo Musé. Toward a combined tool to assist dermatologists in melanoma detection from dermoscopic images of pigmented skin lesions. *Pattern Recognition Letters*, 32(16):2187–2196, 2011.

[2] Skin Cancer Fundation. Skin cancer information, 2016. [Online; accessed on 2016/08/20, available at *http://www.skincancer.org/skin-cancer-information*].

[3] Shadi AlZubi, Naveed Islam, and Maysam Abbod. Multiresolution analysis using wavelet, ridgelet, and curvelet transforms for medical image segmentation. *Journal of Biomedical Imaging*, 2011:4, 2011.

[4] Dermatology Information System, 2015. [Online; accessed on 2015/07/20, available at *http://www.dermis.net*].

[5] DermQuest, 2015. [Online; accessed on 2015/07/20, available at *http://www.dermquest.com*].

[6] World, Health, and Organization. How common is skin cancer?, 2015. [Online; accessed on 08/18/2016, available at *http://www.who.int/uv/faq/skincancer/en/index1.html*].

[7] ©Les cancer en France en 2013. Collection état des lieux et des connaissances, ouvrage collectif édité par l'inca, January 2014. *http://www.e-cancer.fr/Expertises-et-publications/Catalogue-des-publications/Les-cancers-en-France-Edition-2013*.

[8] Jose Luis García Arroyo and Begoña García Zapirain. Detection of pigment

network in dermoscopy images using supervised machine learning and structural analysis. *Computers in biology and medicine*, 44:144–157, 2014. http://dx.doi.org/10.1016/j.compbiomed.2013.11.002.

[9] Haur Yueh Lee, Wen Yee Chay, MB Tang, MT Chio, and Suat Hoon Tan. Melanoma: differences between asian and caucasian patients. *Ann Acad Med Singapore*, 41(1):17–20, 2012.

[10] Darrell S Rigel, Julie Russak, and Robert Friedman. The evolution of melanoma diagnosis: 25 years beyond the abcds. *CA: a cancer journal for clinicians*, 60(5):301–316, 2010.

[11] American cancer society available online, statistics 2013. http://www.cancer.org/acs/groups/content/@research/documents/document/acspc-040951.pdf.

[12] Konstantin Korotkov and Rafael Garcia. Computerized analysis of pigmented skin lesions: a review. *Artificial intelligence in medicine*, 56(2):69–90, 2012.

[13] Robert J Friedman, Darrell S Rigel, and Alfred W Kopf. Early detection of malignant melanoma: The role of physician examination and self-examination of the skin. *CA: a cancer journal for clinicians*, 35(3):130–151, 1985.

[14] W Stolz, A Riemann, AB Cognetta, L Pillet, W Abmayr, D Holzel, P Bilek, F Nachbar, and M Landthaler. Abcd rule of dermatoscopy-a new practical method for early recognition of malignant-melanoma. *European Journal of Dermatology*, 4(7):521–527, 1994.

[15] Agnessa Gadeliya Goodson and Douglas Grossman. Strategies for early melanoma detection: Approaches to the patient with nevi. *Journal of the American Academy of Dermatology*, 60(5):719–735, 2009.

[16] Ilias Maglogiannis and Charalampos N Doukas. Overview of advanced computer vision systems for skin lesions characterization. *IEEE transactions on information technology in biomedicine*, 13(5):721–733, 2009.

[17] Giuseppe Argenziano, Gabriella Fabbrocini, Paolo Carli, Vincenzo De Giorgi, Elena Sammarco, and Mario Delfino. Epiluminescence microscopy for the diagnosis of doubtful melanocytic skin lesions: comparison of the abcd rule of dermatoscopy and a new 7-point checklist based on pattern analysis. *Archives of dermatology*, 134(12):1563–1570, 1998.

[18] RM Mackie and VR Doherty. Seven-point checklist for melanoma. *Clinical and experimental dermatology*, 16(2):151–152, 1991.

[19] Laura Raquel Bareiro Paniagua, Deysi Natalia Leguizamón Correa, Diego P Pinto-Roa, José Luis Vázquez Noguera, Salgueiro Toledo, and A Lizza. Computerized medical diagnosis of melanocytic lesions based on the abcd approach. *CLEI Electronic Journal*, 19(2):6–6, 2016.

[20] Zhishun She, Y Liu, and A Damatoa. Combination of features from skin pattern and abcd analysis for lesion classification. *Skin Research and Technology*, 13(1):25–33, 2007.

[21] G Argenziano, C Catricalà, M Ardigo, P Buccini, P De Simone, L Eibenschutz, A Ferrari, G Mariani, V Silipo, I Sperduti, et al. Seven-point checklist of dermoscopy revisited. *British Journal of Dermatology*, 164(4):785–790, 2011.

[22] Jose Luis Garcia-Arroyo and Begonya Garcia-Zapirain. Recognition of pigment network pattern in dermoscopy images based on fuzzy classification of pixels. *Computer methods and programs in biomedicine*, 153:61–69, 2018.

[23] Giuseppe Argenziano, Iris Zalaudek, Rosamaria Corona, Francesco Sera, Lorenza Cicale, Gianluca Petrillo, Eleonora Ruocco, Rainer Hofmann-Wellenhof, and H Peter Soyer. Vascular structures in skin tumors: a dermoscopy study. *Archives of dermatology*, 140(12):1485–1489, 2004.

[24] Kunio Doi. Computer-aided diagnosis in medical imaging: historical review, current status and future potential. *Computerized medical imaging and graphics*, 31(4):198–211, 2007.

[25] Leila H Eadie, Paul Taylor, and Adam P Gibson. A systematic review of computer-assisted diagnosis in diagnostic cancer imaging. *European journal of radiology*, 81(1):e70–e76, 2012.

[26] Hayit Greenspan, Tanveer Syeda-Mahmood, et al. *Medical content-based retrieval for clinical decision support*. Springer, 2012.

[27] Kunio Doi. Current status and future potential of computer-aided diagnosis in medical imaging. *The British journal of radiology*, 2014.

[28] Konstantin Korotkov et al. *Automatic change detection in multiple pigmented skin lesions*. PhD thesis, 2014.

[29] Cancer Resarch UK. Treating skin cancer, 2016. [Online; accessed on 10/14/2016].

[30] Nabin K Mishra and M Emre Celebi. An overview of melanoma detection in dermoscopy images using image processing and machine learning. *arXiv preprint arXiv:1601.07843*, 2016.

[31] Naheed R Abbasi, Helen M Shaw, Darrell S Rigel, Robert J Friedman, William H McCarthy, Iman Osman, Alfred W Kopf, and David Polsky. Early diagnosis of cutaneous melanoma: revisiting the abcd criteria. *Jama*, 292(22):2771–2776, 2004.

[32] Ammara Masood and Adel Ali Al-Jumaily. Computer aided diagnostic support system for skin cancer: a review of techniques and algorithms. *International journal of biomedical imaging*, 2013, 2013.

[33] M EMRE Celebi, QUAN Wen, HITOSHI Iyatomi, KOUHEI Shimizu, H Zhou, and G Schaefer. A state-of-the-art survey on lesion border detection in dermoscopy images, 2015.

[34] Fiona M Walter, A Toby Prevost, Joana Vasconcelos, Per N Hall, Nigel P Burrows, Helen C Morris, Ann Louise Kinmonth, and Jon D Emery. Using the 7-point checklist as a diagnostic aid for pigmented skin lesions in general practice: a diagnostic validation study. *Br J Gen Pract*, 63(610):e345–e353, 2013.

[35] Con Dolianitis, John Kelly, Rory Wolfe, and Pamela Simpson. Comparative performance of 4 dermoscopic algorithms by nonexperts for the diagnosis of melanocytic lesions. *Archives of dermatology*, 141(8):1008–1014, 2005.

[36] P Carli, E Quercioli, S Sestini, M Stante, L Ricci, G Brunasso, and V De Giorgi. Pattern analysis, not simplified algorithms, is the most reliable method for teaching dermoscopy for melanoma diagnosis to residents in dermatology. *British Journal of Dermatology*, 148(5):981–984, 2003.

[37] M Emre Celebi, Hitoshi Iyatomi, Gerald Schaefer, and William V Stoecker. Lesion border detection in dermoscopy images. *Computerized medical imaging and graphics*, 33(2):148–153, 2009.

[38] Tim Lee, Vincent Ng, Richard Gallagher, Andrew Coldman, and David McLean. Dullrazor®: A software approach to hair removal from images. *Computers in biology and medicine*, 27(6):533–543, 1997.

[39] Paul Wighton, Tim K Lee, and M Stella Atkins. Dermascopic hair disocclusion using inpainting. In *Medical Imaging*, pages 691427–691427. International Society for Optics and Photonics, 2008.

[40] Kimia Kiani and Ahmad R Sharafat. E-shaver: An improved dullrazor® for digitally removing dark and light-colored hairs in dermoscopic images. *Computers in biology and medicine*, 41(3):139–145, 2011.

[41] Mohammad Taghi Bahreyni Toossi, Hamid Reza Pourreza, Hoda Zare, Mohamad-Hoseyn Sigari, Pouran Layegh, and Abbas Azimi. An effective hair removal algorithm for dermoscopy images. *Skin Research and Technology*, 19(3):230–235, 2013.

[42] Nhi H Nguyen, Tim K Lee, and M Stella Atkins. Segmentation of light and dark hair in dermoscopic images: a hybrid approach using a universal kernel. In *SPIE Medical Imaging*, pages 76234N–76234N. International Society for Optics and Photonics, 2010.

[43] Feng-Ying Xie, Shi-Yin Qin, Zhi-Guo Jiang, and Ru-Song Meng. Pde-based unsupervised repair of hair-occluded information in dermoscopy images of melanoma. *Computerized Medical Imaging and Graphics*, 33(4):275–282, 2009.

[44] M Fiorese, E Peserico, and A Silletti. Virtualshave: automated hair removal from digital dermatoscopic images. In *Conference proceedings:... Annual International Conference of the IEEE Engineering in Medicine and Biology Society. IEEE Engineering in Medicine and Biology Society. Annual Conference*, volume 2011, pages 5145–5148, 2010.

[45] Adam Huang, Shun-Yuen Kwan, Wen-Yu Chang, Min-Yin Liu, Min-Hsiu Chi, and Gwo-Shing Chen. A robust hair segmentation and removal approach for clinical images of skin lesions. In *2013 35th Annual International Conference of the IEEE Engineering in Medicine and Biology Society (EMBC)*, pages 3315–3318. IEEE, 2013.

[46] Qaisar Abbas, M Emre Celebi, and Irene Fondón García. Hair removal methods: a comparative study for dermoscopy images. *Biomedical Signal Processing and Control*, 6(4):395–404, 2011.

[47] Qaisar Abbas, Irene Fondón, and Muhammad Rashid. Unsupervised skin lesions border detection via two-dimensional image analysis. *Computer methods and programs in biomedicine*, 104(3):e1–e15, 2011.

[48] Qaisar Abbas, Irene Fondón Garcia, M Emre Celebi, and Waqar Ahmad. A feature-preserving hair removal algorithm for dermoscopy images. *Skin Research and Technology*, 19(1):e27–e36, 2013.

[49] Catarina Barata, Jorge S Marques, and Jorge Rozeira. A system for the detection of pigment network in dermoscopy images using directional filters. *IEEE transactions on biomedical engineering*, 59(10):2744–2754, 2012.

[50] David Delgado Gómez, Constantine Butakoff, Bjarne Kjaer Ersboll, and William Stoecker. Independent histogram pursuit for segmentation of skin lesions. *IEEE Transactions on Biomedical Engineering*, 55(1):157–161, 2008.

[51] M Emre Celebi, Hitoshi Iyatomi, and Gerald Schaefer. Contrast enhancement in dermoscopy images by maximizing a histogram bimodality measure. In *2009 16th IEEE International Conference on Image Processing (ICIP)*, pages 2601–2604. IEEE, 2009.

[52] Ali Madooei, Mark S Drew, Maryam Sadeghi, and M Stella Atkins. Automated pre–processing method for dermoscopic images and its application to pigmented skin lesion segmentation. In *Color and Imaging Conference*, volume 2012, pages 158–163. Society for Imaging Science and Technology, 2012.

[53] Joost Koehoorn, André C Sobiecki, Daniel Boda, Adriana Diaconeasa, Susan Doshi, Stephen Paisey, Andrei Jalba, and Alexandru Telea. Automated digital hair removal by threshold decomposition and morphological analysis. In *International Symposium on Mathematical Morphology and Its Applications to Signal and Image Processing*, pages 15–26. Springer, 2015.

[54] Hengameh Mirzaalian, Tim K Lee, and Ghassan Hamarneh. Hair enhancement in dermoscopic images using dual-channel quaternion tubularness filters and mrf-based multilabel optimization. *IEEE Transactions on Image Processing*, 23(12):5486–5496, 2014.

[55] Alejandro F Frangi, Wiro J Niessen, Koen L Vincken, and Max A Viergever. Multiscale vessel enhancement filtering. In *International Conference on Medical Image Computing and Computer-Assisted Intervention*, pages 130–137. Springer, 1998.

[56] Adam Huang, Wen-Yu Chang, Hsin-Yi Liu, and Gwo-Shing Chen. Capillary detection for clinical images of basal cell carcinoma. In *2012 9th IEEE International Symposium on Biomedical Imaging (ISBI)*, pages 306–309. IEEE, 2012.

[57] Alexandru Telea. An image inpainting technique based on the fast marching method. *Journal of graphics tools*, 9(1):23–34, 2004.

[58] Tim K Lee and Ela Claridge. Predictive power of irregular border shapes for malignant melanomas. *Skin Research and Technology*, 11(1):1–8, 2005.

[59] Shawn Lankton and Allen Tannenbaum. Localizing region-based active contours. *IEEE transactions on image processing*, 17(11):2029–2039, 2008.

[60] Tony F Chan and Luminita A Vese. Active contours without edges. *IEEE Transactions on image processing*, 10(2):266–277, 2001.

[61] Luminita A Vese and Tony F Chan. A multiphase level set framework for image segmentation using the mumford and shah model. *International journal of computer vision*, 50(3):271–293, 2002.

[62] David Mumford and Jayant Shah. Optimal approximations by piecewise smooth functions and associated variational problems. *Communications on pure and applied mathematics*, 42(5):577–685, 1989.

[63] Asad Safi, Maximilian Baust, Olivier Pauly, Victor Castaneda, Tobias Lasser, Diana Mateus, Nassir Navab, Rüdliger Hein, and Mahzad Ziai. Computer–aided diagnosis of pigmented skin dermoscopic images. In *MICCAI International Workshop on Medical Content-Based Retrieval for Clinical Decision Support*, pages 105–115. Springer, 2011.

[64] Fang Li, Chaomin Shen, and Chunming Li. Multiphase soft segmentation with total variation and h^1 regularization. *Journal of Mathematical Imaging and Vision*, 37(2):98–111, 2010.

[65] Sung Ha Kang and Riccardo March. Multiphase image segmentation via equally

distanced multiple well potential. *Journal of Visual Communication and Image Representation*, 25(6):1446–1459, 2014.

[66] Margarida Silveira, Jacinto C Nascimento, Jorge S Marques, André RS Marçal, Teresa Mendonça, Syogo Yamauchi, Junji Maeda, and Jorge Rozeira. Comparison of segmentation methods for melanoma diagnosis in dermoscopy images. *IEEE Journal of Selected Topics in Signal Processing*, 3(1):35–45, 2009.

[67] Faouzi Adjed, Ibrahima Faye, and Fakhreddine Ababsa. Segmentation of skin cancer images using an extension of chan and vese model. In *2015 7th International Conference on Information Technology and Electrical Engineering (ICITEE)*, pages 442–447. IEEE, 2015.

[68] Heydy Castillejos, Volodymyr Ponomaryov, Luis Nino-de Rivera, and Victor Golikov. Wavelet transform fuzzy algorithms for dermoscopic image segmentation. *Computational and mathematical methods in medicine*, 2012, 2012.

[69] Stephane G Mallat. A theory for multiresolution signal decomposition: the wavelet representation. *IEEE transactions on pattern analysis and machine intelligence*, 11(7):674–693, 1989.

[70] Li Ma, Bo Qin, Weidong Xu, and Lei Zhu. Multi-scale descriptors for contour irregularity of skin lesion using wavelet decomposition. In *2010 3rd International Conference on Biomedical Engineering and Informatics*, volume 1, pages 414–418. IEEE, 2010.

[71] Li Ma and Richard C Staunton. Analysis of the contour structural irregularity of skin lesions using wavelet decomposition. *Pattern recognition*, 46(1):98–106, 2013.

[72] Gilbert Strang and Truong Nguyen. *Wavelets and filter banks*. SIAM, 1996.

[73] Stéphane Mallat. *A wavelet tour of signal processing*. Academic press, 1999.

[74] Jean-Luc Starck, Emmanuel J Candès, and David L Donoho. The curvelet transform for image denoising. *IEEE Transactions on image processing*, 11(6):670–684, 2002.

[75] M Abu Mahmoud, A Al-Jumaily, and MS Takruri. Wavelet and curvelet analysis for automatic identification of melanoma based on neural network classification. *International Journal of Computer Information Systems and Industrial Management (IJCISIM)*, 2013.

[76] Bulent Erkol, Randy H Moss, R Joe Stanley, William V Stoecker, and Erik Hvatum. Automatic lesion boundary detection in dermoscopy images using gradient vector flow snakes. *Skin Research and Technology*, 11(1):17–26, 2005.

[77] Alan P Mangan and Ross T Whitaker. Partitioning 3d surface meshes using watershed segmentation. *IEEE Transactions on Visualization and Computer Graphics*, 5(4):308–321, 1999.

[78] Fernand Meyer and Serge Beucher. Morphological segmentation. *Journal of visual communication and image representation*, 1(1):21–46, 1990.

[79] Vicente Grau, AUJ Mewes, M Alcaniz, Ron Kikinis, and Simon K Warfield. Improved watershed transform for medical image segmentation using prior information. *IEEE transactions on medical imaging*, 23(4):447–458, 2004.

[80] Martino Pesaresi and Jon Atli Benediktsson. A new approach for the morphological segmentation of high-resolution satellite imagery. *IEEE transactions on Geoscience and Remote Sensing*, 39(2):309–320, 2001.

[81] Kairit Sirts and Sharon Goldwater. Minimally-supervised morphological segmentation using adaptor grammars. *Transactions of the Association for Computational Linguistics*, 1:255–266, 2013.

[82] M Emre Celebi, Quan Wen, Sae Hwang, Hitoshi Iyatomi, and Gerald Schaefer. Lesion border detection in dermoscopy images using ensembles of thresholding methods. *Skin Research and Technology*, 19(1):e252–e258, 2013.

[83] Harald Ganster, P Pinz, Reinhard Rohrer, Ernst Wildling, Michael Binder, and Harald Kittler. Automated melanoma recognition. *IEEE transactions on medical imaging*, 20(3):233–239, 2001.

[84] Philippe Schmid. Lesion detection in dermatoscopic images using anisotropic diffusion and morphological flooding. In *Image Processing, 1999. ICIP 99. Proceedings. 1999 International Conference on*, volume 3, pages 449–453. IEEE, 1999.

[85] Jagat Narain Kapur, Prasanna K Sahoo, and Andrew KC Wong. A new method for gray-level picture thresholding using the entropy of the histogram. *Computer vision, graphics, and image processing*, 29(3):273–285, 1985.

[86] M Emre Celebi, Y Alp Aslandogan, William V Stoecker, Hitoshi Iyatomi, Hiroshi Oka, and Xiaohe Chen. Unsupervised border detection in dermoscopy images. *Skin Research and Technology*, 13(4):454–462, 2007.

[87] Rahil Garnavi, Mohammad Aldeen, M Emre Celebi, George Varigos, and Sue Finch. Border detection in dermoscopy images using hybrid thresholding on optimized color channels. *Computerized Medical Imaging and Graphics*, 35(2):105–115, 2011.

[88] Qaisar Abbas, Irene Fondón Garcia, M Emre Celebi, Waqar Ahmad, and Qaisar Mushtaq. Unified approach for lesion border detection based on mixture modeling and local entropy thresholding. *Skin Research and Technology*, 19(3):314–319, 2013.

[89] Md Amran Hossen Bhuiyan, Ibrahim Azad, and Md Kamal Uddin. Image processing for skin cancer features extraction. *International Journal of Scientific & Engineering Research*, 4(2):1–6, 2013.

[90] Kalyanmoy Deb, Amrit Pratap, Sameer Agarwal, and TAMT Meyarivan. A fast and elitist multiobjective genetic algorithm: Nsga-ii. *IEEE transactions on evolutionary computation*, 6(2):182–197, 2002.

[91] Fengying Xie and Alan C Bovik. Automatic segmentation of dermoscopy images using self-generating neural networks seeded by genetic algorithm. *Pattern Recognition*, 46(3):1012–1019, 2013.

[92] Milan Sonka, Vaclav Hlavac, and Roger Boyle. *Image processing, analysis, and machine vision*. Cengage Learning, 2014.

[93] Hanzheng Wang, Xiaohe Chen, Randy H Moss, R Joe Stanley, William V Stoecker, M Emre Celebi, Thomas M Szalapski, Joseph M Malters, James M Grichnik, Ashfaq A Marghoob, et al. Watershed segmentation of dermoscopy images using a watershed technique. *Skin Research and Technology*, 16(3):378–384, 2010.

[94] Huiyu Zhou, Gerald Schaefer, Abdul H Sadka, and M Emre Celebi. Anisotropic mean shift based fuzzy c-means segmentation of dermoscopy images. *IEEE Journal of Selected Topics in Signal Processing*, 3(1):26–34, 2009.

[95] André Sobiecki, Andrei Jalba, Daniel Boda, Adriana Diaconeasa, and Alexandru Telea. Gap-sensitive segmentation and restoration of digital images. In *TPCG*, pages 1–8, 2014.

[96] Jeffrey Glaister, Alexander Wong, and David A Clausi. Segmentation of skin lesions from digital images using joint statistical texture distinctiveness. *IEEE Transactions on Biomedical Engineering*, 61(4):1220–1230, 2014.

[97] Howard Zhou, Mei Chen, Le Zou, Richard Gass, Laura Ferris, Laura Drogowski, and James M Rehg. Spatially constrained segmentation of dermoscopy images. In *Biomedical Imaging: From Nano to Macro, 2008. ISBI 2008. 5th IEEE International Symposium on*, pages 800–803. IEEE, 2008.

[98] Jin Qi, Miao Le, Chunming Li, and Ping Zhou. Global and local information based deep network for skin lesion segmentation. *arXiv preprint arXiv:1703.05467*, 2017.

[99] Kathy M Clawson, Philip Morrow, Bryan Scotney, John McKenna, and Olivia

Dolan. Analysis of pigmented skin lesion border irregularity using the harmonic wavelet transform. In *Machine Vision and Image Processing Conference, 2009. IMVIP'09. 13th International*, pages 18–23. IEEE, 2009.

[100] David E Newland. Harmonic wavelet analysis. In *Proceedings of the Royal Society of London A: Mathematical, Physical and Engineering Sciences*, volume 443, pages 203–225. The Royal Society, 1993.

[101] Rajib Chakravorty, Sisi Liang, Mani Abedini, and Rahil Garnavi. Dermatologist-like feature extraction from skin lesion for improved asymmetry classification in ph 2 database. In *Engineering in Medicine and Biology Society (EMBC), 2016 IEEE 38th Annual International Conference of the*, pages 3855–3858. IEEE, 2016.

[102] Vincent TY Ng, Benny YM Fung, and Tim K Lee. Determining the asymmetry of skin lesion with fuzzy borders. *Computers in biology and medicine*, 35(2):103–120, 2005.

[103] Srinivasan Sankaran and Gopalakrishnan Sethumadhavan. Quantifications of asymmetries on the spectral bands of malignant melanoma using six sigma threshold as preprocessor. In *Computational Intelligence and Information Technology, 2013. CIIT 2013. Third International Conference on*, pages 80–86. IET, 2013.

[104] Wen-Yu Chang, Adam Huang, Chung-Yi Yang, Chien-Hung Lee, Yin-Chun Chen, Tian-Yau Wu, and Gwo-Shing Chen. Computer-aided diagnosis of skin lesions using conventional digital photography: a reliability and feasibility study. *PloS one*, 8(11):e76212, 2013.

[105] Robert Amelard, Jeffrey Glaister, Alexander Wong, and David A Clausi. Melanoma decision support using lighting-corrected intuitive feature models. In *Computer Vision Techniques for the Diagnosis of Skin Cancer*, pages 193–219. Springer, 2014.

[106] MH Jafari, S Samavi, N Karimi, SMR Soroushmehr, K Ward, and K Najarian. Automatic detection of melanoma using broad extraction of features from digital images. In *Engineering in Medicine and Biology Society (EMBC), 2016 IEEE 38th Annual International Conference of the*, pages 1357–1360. IEEE, 2016.

[107] J Jaworek-Korjakowska and R Tadeusiewicz. Determination of border irregularity in dermoscopic color images of pigmented skin lesions. In *2014 36TH Annual International Conference of the IEEE Engineering in Medicine and Biology Society*, pages 6459–6462. IEEE, 2014.

[108] Tim K Lee, David I McLean, and M Stella Atkins. Irregularity index: a new border irregularity measure for cutaneous melanocytic lesions. *Medical image analysis*, 7(1):47–64, 2003.

[109] TB Holmstrom. A survey and evaluation of features for the diagnosis of malignant melanoma. *Mater Thesis*, 2005.

[110] Benjamin S Aribisala and Ela Claridge. A border irregularity measure using a modified conditional entropy method as a malignant melanoma predictor. In *International Conference Image Analysis and Recognition*, pages 914–921. Springer, 2005.

[111] Yu Zhou, Melvyn Smith, Lyndon Smith, and Robert Warr. A new method describing border irregularity of pigmented lesions. *Skin Research and Technology*, 16(1):66–76, 2010.

[112] Yue Iris Cheng, Ragavendar Swamisai, Scott E Umbaugh, Randy H Moss, William V Stoecker, Saritha Teegala, and Subhashini K Srinivasan. Skin lesion classification using relative color features. *Skin Research and Technology*, 14(1):53–64, 2008.

[113] Andrew J Round, Andrew WG Duller, and Peter J Fish. Lesion classification using skin patterning. *Skin research and technology*, 6(4):183–192, 2000.

[114] Ying Chang, R Joe Stanley, Randy H Moss, and William Van Stoecker. A systematic heuristic approach for feature selection for melanoma discrimination using clinical images. *Skin Research and Technology*, 11(3):165–178, 2005.

[115] R Joe Stanley, Randy Hays Moss, William Van Stoecker, and Chetna Aggarwal. A fuzzy-based histogram analysis technique for skin lesion discrimination in dermatology clinical images. *Computerized Medical Imaging and Graphics*, 27(5):387–396, 2003.

[116] Jixiang Chen, R Joe Stanley, Randy H Moss, and William Van Stoecker. Colour analysis of skin lesion regions for melanoma discrimination in clinical images. *Skin Research and Technology*, 9(2):94–104, 2003.

[117] Ela Claridge, Symon Cotton, Per Hall, and Marc Moncrieff. From colour to tissue histology: physics-based interpretation of images of pigmented skin lesions. *Medical Image Analysis*, 7(4):489–502, 2003.

[118] Omar Abuzaghleh, Buket D Barkana, and Miad Faezipour. Automated skin lesion analysis based on color and shape geometry feature set for melanoma early detection and prevention. In *Systems, Applications and Technology Conference (LISAT), 2014 IEEE Long Island*, pages 1–6. IEEE, 2014.

[119] Brian D'Alessandro, Atam P Dhawan, and Nizar Mullani. Computer aided analysis of epi-illumination and transillumination images of skin lesions for diagnosis of skin cancers. In *2011 Annual International Conference of the IEEE Engineering in Medicine and Biology Society*, pages 3434–3438. IEEE, 2011.

[120] Sina Khakabi, Paul Wighton, Tim K Lee, and M Stella Atkins. Multilevel feature extraction for skin lesion segmentation in dermoscopic images. In *SPIE Medical Imaging*, pages 83150E–83150E. International Society for Optics and Photonics, 2012.

[121] Qaisar Abbas, M Emre Celebi, Carmen Serrano, Irene FondóN GarcíA, and

Guangzhi Ma. Pattern classification of dermoscopy images: A perceptually uniform model. *Pattern Recognition*, 46(1):86–97, 2013.

[122] Noel Codella, Junjie Cai, Mani Abedini, Rahil Garnavi, Alan Halpern, and John R Smith. Deep learning, sparse coding, and svm for melanoma recognition in dermoscopy images. In *International Workshop on Machine Learning in Medical Imaging*, pages 118–126. Springer, 2015.

[123] Timo Ojala, Kimmo Valkealahti, Erkki Oja, and Matti Pietikäinen. Texture discrimination with multidimensional distributions of signed gray-level differences. *Pattern Recognition*, 34(3):727–739, 2001.

[124] Timo Ojala, Matti Pietikainen, and Topi Maenpaa. Multiresolution gray-scale and rotation invariant texture classification with local binary patterns. *IEEE Transactions on pattern analysis and machine intelligence*, 24(7):971–987, 2002.

[125] Victor González-Castro, Johan Debayle, Yanal Wazaefi, Mehdi Rahim, Caroline Gaudy, Jean-Jacques Grob, and Bernard Fertil. Automatic classification of skin lesions using geometrical measurements of adaptive neighborhoods and local binary patterns. In *Image Processing (ICIP), 2015 IEEE International Conference on*, pages 1722–1726. IEEE, 2015.

[126] Faouzi Adjed, Ibrahima Faye, Fakhreddine Ababsa, Syed Jamal Gardezi, and Sarat Chandra Dass. Classification of skin cancer images using local binary pattern and svm classifier. In *AIP Conference Proceedings*, volume 1787, page 080006. AIP Publishing, 2016.

[127] Maryam Sadeghi, Tim K Lee, David McLean, Harvey Lui, and M Stella Atkins. Detection and analysis of irregular streaks in dermoscopic images of skin lesions. *IEEE transactions on medical imaging*, 32(5):849–861, 2013.

[128] Maen Takruri, Adel Al-Jumaily, and Mohamed Khaled Abu Mahmoud. Automatic recognition of melanoma using support vector machines: A study based on wavelet, curvelet and color features. In *Industrial Automation, Information and*

Communications Technology (IAICT), 2014 International Conference on, pages 70–75. IEEE, 2014.

[129] Pablo G Cavalcanti and Jacob Scharcanski. Automated prescreening of pigmented skin lesions using standard cameras. *Computerized Medical Imaging and Graphics*, 35(6):481–491, 2011.

[130] S Sabbaghi, Mohammad Aldeen, and Rahil Garnavi. A deep bag-of-features model for the classification of melanomas in dermoscopy images. In *Engineering in Medicine and Biology Society (EMBC), 2016 IEEE 38th Annual International Conference of the*, pages 1369–1372. IEEE, 2016.

[131] S Sabbaghi, Mohammad Aldeen, Rahil Garnavi, George Varigos, C Doliantis, and J Nicolopoulos. Automated colour identification in melanocytic lesions. In *Engineering in Medicine and Biology Society (EMBC), 2015 37th Annual International Conference of the IEEE*, pages 3021–3024. IEEE, 2015.

[132] Lei Bi, Jinman Kim, Euijoon Ahn, Dagan Feng, and Michael Fulham. Automatic melanoma detection via multi-scale lesion-biased representation and joint reverse classification. In *Biomedical Imaging (ISBI), 2016 IEEE 13th International Symposium on*, pages 1055–1058. IEEE, 2016.

[133] Yuexiang Li and Linlin Shen. Skin lesion analysis towards melanoma detection using deep learning network. *arXiv preprint arXiv:1703.00577*, 2017.

[134] Yarin Gal, Riashat Islam, and Zoubin Ghahramani. Deep bayesian active learning with image data. *arXiv preprint arXiv:1703.02910*, 2017.

[135] Adria Romero Lopez, Xavier Giro-i Nieto, Jack Burdick, and Oge Marques. Skin lesion classification from dermoscopic images using deep learning techniques. In *Biomedical Engineering (BioMed), 2017 13th IASTED International Conference on*, pages 49–54. IEEE, 2017.

[136] Andre Esteva, Brett Kuprel, Roberto A Novoa, Justin Ko, Susan M Swetter, Helen M Blau, and Sebastian Thrun. Dermatologist-level classification of skin cancer with deep neural networks. *Nature*, 542(7639):115, 2017.

[137] Noel CF Codella, Q-B Nguyen, Sharath Pankanti, DA Gutman, Brian Helba, AC Halpern, and John R Smith. Deep learning ensembles for melanoma recognition in dermoscopy images. *IBM Journal of Research and Development*, 61(4):5–1, 2017.

[138] Thorsten Joachims. Text categorization with support vector machines: Learning with many relevant features. In *European conference on machine learning*, pages 137–142. Springer, 1998.

[139] B Yegnanarayana. *Artificial neural networks*. PHI Learning Pvt. Ltd., 2009.

[140] Catarina Barata, Margarida Ruela, Mariana Francisco, Teresa Mendonça, and Jorge S Marques. Two systems for the detection of melanomas in dermoscopy images using texture and color features. *IEEE Systems Journal*, 8(3):965–979, 2014.

[141] Catarina Barata, M Emre Celebi, and Jorge S Marques. Improving dermoscopy image classification using color constancy. *IEEE journal of biomedical and health informatics*, 19(3):1146–1152, 2015.

[142] Massimo Ferri and Ignazio Stanganelli. Size functions for the morphological analysis of melanocytic lesions. *Journal of Biomedical Imaging*, 2010:5, 2010.

[143] Grzegorz Surowka and Katarzyna Grzesiak-Kopec. Different learning paradigms for the classification of melanoid skin lesions using wavelets. In *2007 29th Annual International Conference of the IEEE Engineering in Medicine and Biology Society*, pages 3136–3139. IEEE, 2007.

[144] Ilias G Maglogiannis and Elias P Zafiropoulos. Characterization of digital medical images utilizing support vector machines. *BMC Medical Informatics and Decision Making*, 4(1):1, 2004.

[145] Grzegorz Surowka. Supervised learning of melanocytic skin lesion images. In *2008 Conference on Human System Interactions*, pages 121–125. IEEE, 2008.

[146] Elisabetta La Torre, Barbara Caputo, and Tatiana Tommasi. Learning methods for melanoma recognition. *International Journal of Imaging Systems and Technology*, 20(4):316–322, 2010.

[147] Hitoshi Iyatomi, Hiroshi Oka, M Emre Celebi, Masahiro Hashimoto, Masafumi Hagiwara, Masaru Tanaka, and Koichi Ogawa. An improved internet-based melanoma screening system with dermatologist-like tumor area extraction algorithm. *Computerized Medical Imaging and Graphics*, 32(7):566–579, 2008.

[148] Stephan Dreiseitl, Lucila Ohno-Machado, Harald Kittler, Staal Vinterbo, Holger Billhardt, and Michael Binder. A comparison of machine learning methods for the diagnosis of pigmented skin lesions. *Journal of biomedical informatics*, 34(1):28–36, 2001.

[149] Teresa Mendonça, Pedro M Ferreira, Jorge S Marques, André RS Marcal, and Jorge Rozeira. Ph 2-a dermoscopic image database for research and benchmarking. In *2013 35th Annual International Conference of the IEEE Engineering in Medicine and Biology Society (EMBC)*, pages 5437–5440. IEEE, 2013.

[150] Giuseppe Argenziano, HP Soyer, V De Giorgi, Domenico Piccolo, Paolo Carli, and Mario Delfino. Interactive atlas of dermoscopy (book and cd-rom). 2000.

[151] Jeremy Kawahara and Ghassan Hamarneh. Multi-resolution-tract cnn with hybrid pretrained and skin-lesion trained layers. In *International Workshop on Machine Learning in Medical Imaging*, pages 164–171. Springer, 2016.

[152] Leah Bar, Tony F Chan, Ginmo Chung, Miyoun Jung, Nahum Kiryati, Nir Sochen, and Luminita A Vese. Mumford and shah model and its applications to image segmentation and image restoration. *Handbook of Mathematical Methods in Imaging*, pages 1–52, 2014.

[153] Jinming Duan, Zhenkuan Pan, Xiangfeng Yin, Weibo Wei, and Guodong Wang.

Some fast projection methods based on chan-vese model for image segmentation. *EURASIP Journal on Image and Video Processing*, 2014(1):7, 2014.

[154] Aslak Grinsted, John C Moore, and Svetlana Jevrejeva. Application of the cross wavelet transform and wavelet coherence to geophysical time series. *Nonlinear processes in geophysics*, 11(5/6):561–566, 2004.

[155] Ribeiro Kleber Mariano, Júnior Roberto Alves Braga, Sáfadi Thelma, and Horgan Graham. Comparison between fourier and wavelets transforms in biospeckle signals. *Applied Mathematics*, 2013, 2013.

[156] Alexander Grossmann and Jean Morlet. Decomposition of hardy functions into square integrable wavelets of constant shape. *SIAM journal on mathematical analysis*, 15(4):723–736, 1984.

[157] Minh N Do and Martin Vetterli. The finite ridgelet transform for image representation. *IEEE Transactions on image Processing*, 12(1):16–28, 2003.

[158] Emmanuel J Candès and David L Donoho. Ridgelets: A key to higher-dimensional intermittency? *Philosophical Transactions of the Royal Society of London A: Mathematical, Physical and Engineering Sciences*, 357(1760):2495–2509, 1999.

[159] Emmanuel J Candes and David L Donoho. Curvelets: A surprisingly effective nonadaptive representation for objects with edges. Technical report, Stanford Univ Ca Dept of Statistics, 2000.

[160] Emmanuel Candes, Laurent Demanet, David Donoho, and Lexing Ying. Fast discrete curvelet transforms. *Multiscale Modeling & Simulation*, 5(3):861–899, 2006.

[161] Tanaya Guha and QM Jonathan Wu. *Curvelet based feature extraction*. INTECH Open Access Publisher, 2010.

[162] Timo Ahonen, Abdenour Hadid, and Matti Pietikainen. Face description with

local binary patterns: Application to face recognition. *IEEE transactions on pattern analysis and machine intelligence*, 28(12):2037–2041, 2006.

[163] Alice Porebski, Nicolas Vandenbroucke, and Ludovic Macaire. Haralick feature extraction from lbp images for color texture classification. In *2008 First Workshops on Image Processing Theory, Tools and Applications*, pages 1–8. IEEE), 2008.

[164] Marko Heikkilä, Matti Pietikäinen, and Cordelia Schmid. Description of interest regions with center-symmetric local binary patterns. In *ICVGIP*, volume 6, pages 58–69. Springer, 2006.

[165] Lun Zhang, Rufeng Chu, Shiming Xiang, Shengcai Liao, and Stan Li. Face detection based on multi-block lbp representation. *Advances in biometrics*, pages 11–18, 2007.

[166] Lior Wolf, Tal Hassner, and Yaniv Taigman. Descriptor based methods in the wild. In *Workshop on faces in'real-life'images: Detection, alignment, and recognition*, 2008.

[167] Matti Pietikäinen, Abdenour Hadid, Guoying Zhao, and Timo Ahonen. *Computer vision using local binary patterns*, volume 40. Springer Science & Business Media, 2011.

[168] Anil K Jain, Robert P. W. Duin, and Jianchang Mao. Statistical pattern recognition: A review. *IEEE Transactions on pattern analysis and machine intelligence*, 22(1):4–37, 2000.

[169] Alex J Smola and Bernhard Schölkopf. A tutorial on support vector regression. *Statistics and computing*, 14(3):199–222, 2004.

[170] Simon Haykin and Neural Network. A comprehensive foundation. *Neural Networks*, 2(2004), 2004.

[171] Ajith Abraham. Artificial neural networks. *handbook of measuring system design*, 2005.

[172] David Kriesel. *A brief Introduction to Neural Networks*. dkriesel.com, 2005.

[173] Peter H Sydenham and Richard Thorn. *Handbook of measuring system design*, volume 2. Wiley, 2005.

[174] Ron Kohavi et al. A study of cross-validation and bootstrap for accuracy estimation and model selection. In *Ijcai*, volume 14, pages 1137–1145, 1995.

[175] Prabir Burman. A comparative study of ordinary cross-validation, v-fold cross-validation and the repeated learning-testing methods. *Biometrika*, 76(3):503–514, 1989.

[176] Jianhong Jackie Shen. A stochastic-variational model for soft mumford-shah segmentation. *International Journal of Biomedical Imaging*, 2006, 2006.

[177] T. Mendonça, F., M. Ferreira, P., A. Marcal, R. S., C. Barata, J. Marques, S., J. Rocha, and Rozeira J. Ph2: A public database for the analysis of dermoscopic images. *in Dermoscopy Image Analysis (M. E. Celebi, T. Mendonca, and J. S. Marques, eds.)*, pages 419–439, 2015.

[178] Xiao-Feng Wang, De-Shuang Huang, and Huan Xu. An efficient local chan–vese model for image segmentation. *Pattern Recognition*, 43(3):603–618, 2010.

[179] Wendy Liu, John P Dowling, William K Murray, Grant A McArthur, John F Thompson, Rory Wolfe, and John W Kelly. Rate of growth in melanomas: characteristics and associations of rapidly growing melanomas. *Archives of Dermatology*, 142(12):1551–1558, 2006.

[180] Shutao Li and Bin Yang. Multifocus image fusion by combining curvelet and wavelet transform. *Pattern Recognition Letters*, 29(9):1295–1301, 2008.

[181] Jalal M Fadili and Jean-Luc Starck. Curvelets and ridgelets, 2009.

Publications

1. Faouzi adjed, Jamal Gardezi, Fakhreddine Ababsa, Ibrahima Faye, and Sarat Cahndra Dass. Fusion of Structural and Textural Features for Melanoma Recognition. *IET Computer Vision*. 2017

2. Faouzi Adjed, Fakhreddine Ababsa, Ibrahima Faye, Jamal Gardezi, and Sarat Chandra Dass. Classification of skin cancer using local binary pattern and SVM classifier. *In 2016 4th International Conference on fundamental and applied aciences (ICFAS)*. IEEE, 2016

3. Faouzi Adjed, Ibrahima Faye, and Fakhreddine Ababsa. Segemntation of skin cancer images using an extension of Chan and Veses model. in 2015, 7^{th} *International Conference on Information Technology and Electrical Engineering (ICITEE)*, pages 442-447. IEEE, 2015

université PARIS-SACLAY
ÉCOLE DOCTORALE
Sciences et technologies de l'information et de la communication (STIC)

Titre : Segmentation et Détection du Cancer de la Peau en Utilisant la Variation Totale et l'Analyse Multi-résolution

Mots clés : Segmentation, Détection, Variation Totale, Analyse Multi-résolution, Imagerie médicale

Résumé : Les décès du cancer de la peau sont majoritairement des mélanomes malins. Il est considéré comme l'un des plus dangereux cancer. A ses débuts, les mélanomes malins sont traités avec des simples biopsies et sont complètement curable. Pour cela, une détection précoce est la meilleure solution pour réduire ses conséquences désastreuses. Imagerie médicale telle que la dermoscopie et les caméras à images standard sont les outils disponibles les plus adaptées pour diagnostiquer précocement les mélanomes. Le diagnostic assisté par ordinateur (CAD) est développé dans le but d'accompagner les radiologistes dans la détection et le diagnostic. Cependant, il y a un besoin d'améliorer la précision de la segmentation et de détection des lésions. Dans ce travail, le modèle de Chan et Vese a été adapté pour segmenter davantage les variations à l'intérieur des lésions avec un résultat très encourageant. La deuxième tâche consiste à extraire des caractéristiques afin de discriminer les mélanomes. Deux méthodes ont été développée, une se basant sur l'irrégularité des bords des lésions et l'autre par la fusion des caractéristiques texturales et structurelles. Les résultats ont montrés de bonnes performances avec une précision de 86.54% et de 86.07%, respectivement.

Title : Skin Cancer Segmentation and Detection Using Total Variation and Mutiresolution Analysis

Keywords : Segmentation, Detection, Total Variation, Multiresolutional Analysis, medical imaging

Abstract : The vast majority of skin cancer deaths are due to malignant melanoma. It is considered as one of the most dangerous cancers. In its early stages, malignant melanoma is completely curable with a simple biopsy. Therefore, an early detection is the best solution to improve skin cancer prognostic. Medical imaging such as dermoscopy and standard camera images are the most suitable tools available to diagnose melanoma at early stages. To help radiologists in the diagnosis of melanoma cases, there is a strong need to develop computer aided diagnosis (CAD) systems. The accurate segmentation and classification of pigment skin lesions still remains a challenging task due to the various colors and structures developed randomly inside the lesions. The current work focused on two main tasks. In the first task, a new approach of the segmentation of skin lesions based on Chan and Vese model is developed. The model is adapted to segment the variations of the pigment inside the lesion and not only the main border. The subjective evaluation, applied on a database of standard camera images, obtained a very encouraging results with 97.62% of true detection rate. In the second main task, two feature extraction methods were developed for the analysis of standard camera and dermoscopy images. The method developed for the standard camera skin cancer images is based on border irregularities, introducing two new concepts, which are valleys and crevasses as first and second level of the border irregularity. The method has been implemented on DermIs and DermQues, two databases of standard camera images, and achieved an accuracy of 86.54% with a sensitivity of 80% and a specificity of 95.45%. The second method consisted of a fusion of structural and textural features. The structural features were extracted from wavelet and curvelet coefficients, while the textural features were obtained from the local binary pattern operator. The method has been implemented on the PH2 database for dermoscopy images with 1000-random sampling cross validation. The obtained results achieved an accuracy, a sensitivity and a specificity of 86:07%, 78.93% and 93.25%. Compared to the existing methods, the proposed methods in this work show very good performances.

Université Paris-Saclay
Espace Technologique / Immeuble Discovery
Route de l'Orme aux Merisiers RD 128 / 91190 Saint-Aubin, France